THEORETICAL CHARACTERIZATION OF MICROSTRIP LUMPED ELEMENTS AND INTERCONNECTS IN $M^3IC'S$

by
Pisti B. Katehi
Dimitris Pavlidis

Department of Electrical Engineering and Computer Science
The University of Michigan
Ann Arbor, MI 48109-2122

June 1988

PROGRESS REPORT

1. ARO Proposal Number: DAAL03-87-K-0088 (23836-EL)

2. Period Covered By Report: 1 January 1988 - 30 June 1988

3. Title of Proposal: Theoretical and Experimental Study of Microstrip Discontinuities in Millimeter Wave Integrated Circuits.

4. Contract Number: DAAL03-87-K-0088

5. Name of Institution: University of Michigan

6. Authors of Report: Pisti B. Katehi
Dimitris Pavlidis

7. Listing of Interim Reports and Manuscripts Submitted or Published Under Full or Partial ARO Sponsorship During This Reporting Period:

(1) L.P. Dunleavy and P.B. Katehi, "A New Method For Discontinuity Analysis in Shielded Microstrip," Digest of the 1988 IEEE MTT-S International Symposium, New York, New York, May 1988, pp. 701-704.

(2) L.P. Dunleavy and P.B. Katehi, "Shielding Effects in Microstrip Discontinuities- Part I: Theory". It has been submitted for publication in the IEEE Trans. on Microwave Theory and Techniques.

(3) L.P. Dunleavy and P.B. Katehi, "Shielding Effects in Microstrip Discontinuities- Part II: Applications". It has been submitted for publication in the IEEE Trans. on Microwave Theory and Techniques.

(4) T.E. van Deventer and P.B. Katehi, "High Frequency Conductor Losses in Shielded Microstrip". Technical Report ARO-024562-2-T, EECS Department, University of Michigan, Ann Arbor, June 1988.

(5) M.E. Coluzzi and P.B. Katehi, " Theoretical Characterization of an Air-Bridge". Technical Report ARO-024562-1-T, EECS Department, University of Michigan, Ann Arbor, June 1988.

8. Scientific Personnel Supported By This Project:

Faculty	Graduate Students
P. B. Katehi	M. Coluzzi
D. Pavlidis	M. Weiss
	W. Harokopus
	E. van Deventer

RESEARCH TASKS

Title	Personel Involved with the Research
1.Theoretical Characterization of an Air-Bridge.	P.B. Katehi*
2.High Frequency Conductor Losses in Shielded Microstip.	P.B. Katehi T.E. van Deventer
3.Shielding Effects on the Phase Velocity of Microstrip Lines.	P.B. Katehi L.P. Dunleavy**
4.Gate Capacitance Modeling of GaAs MESFET's in Millimeter Wave Frequencies.	D. Pavlidis M. Weiss W. Harokopus P.B. Katehi

* Part of the theoretical formulation for this problem has been carried out by Mr.M. Coluzzi who was a graduate student supported by this contract during the period September 1987-January 1988. Last February, Mr. Coluzzi left the University and since then Dr. Katehi has been responsible for this task.

** Dr. L.P. Dunleavy graduated last May and he has been with Hughes Torrance since then.

1. THEORETICAL CHARACTERIZATION OF AN AIR-BRIDGE

Faculty Supervisor: Pisti B. Katehi

Graduate Student Participant: None at the present time.
(There is a new graduate student starting in Fall 1988 who will continue the work in this problem).

Period: 1 January 1988 - 30 June 1988.

Work Performed:

The theoretical formulation for the air bridge has been completed. The analytical method employed in these algorithms efficiently takes into account shielding effects and conductor losses(5)(Appendix E).

Program for the Second Year:

Using the completed theoretical formulation of the problem, computer programs will be written which will give frequency dependent equivalent circuits or scattering parameters for the Air-Bridge. The theoretical results will be compared to available experimental data for verification.

Publications and Reports:

M.E. Coluzzi and P.B. Katehi, "Theoretical Characterization of an Air-Bridge". Technical Report ARO-024562-1-T, EECS Department, University of Michigan, Ann Arbor, June 1988.

2. HIGH FREQUENCY CONDUCTOR LOSSES IN SHIELDED MICROSTRIP

Faculty Supervisor: Pisti B. Katehi

Graduate Student Participant: T. E. van Deventer

Period: 1 January 1988 - 30 June 1988

Work Performed:

A new analytical method has been developed to evaluate conductor losses in single or multiple shielded microstrip lines (4) (Appendix D). Numerical results for the case of a single line have been derived and we are in the process of comparing them to available data at lower frequencies.

Program for the Second year:

Extensive numerical data will be derived for the case of single or multiple shielded microstrip lines printed on multilayer substrates. In addition, we will try to extend the method to microstrip discontinuities.

Publications and Reports:

T.E. van Deventer and P.B. Katehi, "High Frequency Conductor Losses in Shielded Microstrip". Technical Report ARO-024562-2-T, EECS Department, University of Michigan, Ann Arbor, June 1988.

3. SHIELDING EFFECTS ON THE PHASE VELOCITY OF MICROSTRIP LINES

Faculty Supervisor: P.B. Katehi

Graduate Student Participant: L.P. Dunleavy

Period: 1 January 1988 - 30 June 1988

Work Performed:

An integral equation method has been developed for the accurate evaluation of shielding effects on the propagation properties of shielded microstrip lines. The integral equation has been derived by applying reciprocity theorem and then is solved by the method of moments (2),(3),(Appendices B,C). Numerical results have been derived and compared to experimental ones for verification of the theory.

Program for the second year:

For the second year we plan on extending the study of shielding effects to single or multiple microstrip lines on multilayer substrates.

Publications and Reports:

L.P. Dunleavy and P.B. Katehi, "A New Method for Discontinuity Analysis in Shielded Microstrip," Digest of the 1988 IEEE MTT-S International Symposium, New York, New York, May 1988, PP. 701-704.

L.P. Dunleavy and P.B. Katehi, "Shielding Effects in Microstrip Discontinuities- Part I: Theory". It has been submitted for publication in the IEEE Trans. on Microwave Theory and Techniques.

L.P. Dunleavy and P.B. Katehi, "Shielding Effects in Microstrip Discontinuities- Part II: Applications". It has been submitted for publication in the IEEE Trans. on Microwave Theory and Techniques.

4 SIMULATION OF TRANSISTOR INPUT IMPEDANCE AT MILLIMETR-WAVE FREQUENCIES.

Faculty Supervisors: D. Pavlidis
P.B. Katehi

Post Graduate Participant: M. Weiss

Graduate Student Participant: W.P. Harokopus

Work Performed:

As a first step to the analytical evaluation of a GaAs MESFET at millimeter wave frequencies, a quasi-static modeling of the transistor gate was caried out using a finite difference method.In order to reduce computation time, we used Neumann's boundary conditions in conjuction with a graded mesh. Results which were derived from this approach compare very well with available data for the case of a simple-shaped depletion region. In addition, we have initiated a dynamic analysis of the problem which is based on a finite element method. The formulation of the problem has been completed and we are in the process of writing the computer programs.

Program for the Second Year:

In addition to the gate capacitance modelling we are planning to extend our theoretical studies towards a better understanding of other transistor characteristics such as gate-drain and drain-source capacitance, access resistance to the active channel, and geometry and transition effects.

TASKS TO BE INITIATED DURING THE SECOND YEAR

Other tasks we plan to initiate during the coming period is a study on the geometry optimization of the devices. Efficient millimeter wave operation requires a good knowledge of the electromagnetic field transformation at the transmission line to gate or drain terminal transition. Propagation along the gate and drain strips should also be considered because of the effects that it can have on the transistor gain. The gate configuration, width and paralleling for power applications will be examined and understood by considering the distributed nature of the device. Using our full-wave analysis we will address the above problems and extract equivalent circuits permitting the optimization of device geometry and material parameters.

For these tasks, **Dr. D. Pavlidis** and **Dr. P.B. Katehi** will serve as faculty advisors. Other scientific personel who will participate in these problems are:

T.E. van Deventer (Graduate Student)
M. Weiss (Postdoctoral Fellow)

Appendix A

"A new Method for Discontinuity Analysis in Shielded Microstrip"
L.P. Dunleavy and P.B. Katehi

A NEW METHOD FOR DISCONTINUITY ANALYSIS IN SHIELDED MICROSTRIP

L.P. Dunleavy and P.B. Katehi

The Radiation Laboratory

University of Michigan, Ann Arbor, MI

Abstract-. A new integral equation method is described for the accurate full-wave analysis of shielded microstrip discontinuities. The integral equation is derived by an application of reciprocity theorem, then solved by the method of moments. Numerical and experimental results are presented for open-end and series gap discontinuities, and a coupled line filter.

I. INTRODUCTION

The development of more accurate microstrip discontinuity models, based on full-wave analyses, is key to improving microwave and millimeter-wave circuit simulations and reducing lengthy design cycle costs. In most applications, radiation and electromagnetic interference are avoided by enclosing microstrip circuitry in a shielding cavity (or housing) as shown in Figure 1. The effect of the shielding is significant, and requires accurate modeling, at high frequencies. Shielding effects are not adequately accounted for in the discontinuity models used in most available microwave CAD software.

To address these inadequacies, a new method was developed for the full-wave analysis of discontinuities in shielded microstrip [2]. This method accurately takes into account the effect of the shielding enclosure. The theoretical contribution, as compared to previous work [3]-[5], is in the novel way that reciprocity theorem, the method of moments, and transmission line theory are combined to solve for discontinuity parasitics. As illustrated in Figure 2, the coaxial feed is modeled using an equivalent magnetic "frill" current [6,7]. To the authors' knowledge, this is the first time that the frill current approach has been applied to microstrip circuit problems.

To demonstrate the method, numerical results are presented for open-end and series gap discontinuities, and a four resonator coupled line filter. These results are compared to other full-wave analyses, to data from *Super Compact* and *Touchstone* [1], and to measurements. The measurements were performed using a variation of the TSD de-embedding technique [8,9].

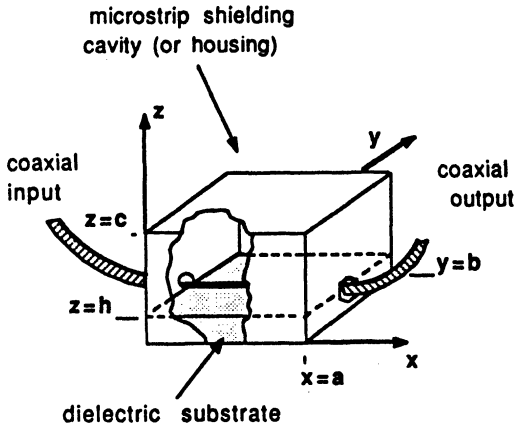

Figure 1: In most practical designs, microstrip circuitry is enclosed in a shielding cavity whose effects must be accurately modeled at high frequencies.

II. SUMMARY OF THEORETICAL METHOD

In the theoretical derivation [2], an application of reciprocity theorem results in an integral equation relating the magnetic current source $\bar{M}_s$, and the electric current on the conducting strips $\bar{J}_s$, to the electromagnetic fields inside the cavity. A Galerkin's implementation of the method of moments is employed by first dividing the strips into N_s subsections. The current is then expanded according to [1]

$$\bar{J}_s = \psi(y) \sum_{p=1}^{N_s} I_p \alpha_p(x)\, \hat{x} \,. \qquad (1)$$

[1] *Super Compact* and *Touchstone* are microwave CAD software packages available from Compact Software and EESOF respectively.

0149-645X/88/0000-0701$01.00 © 1988 IEEE

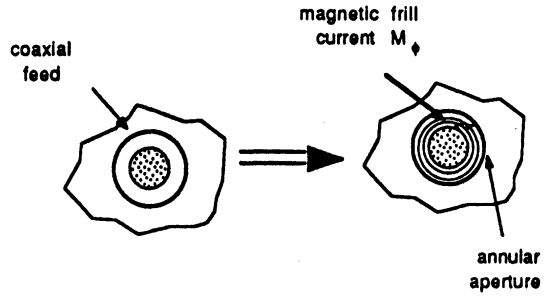

Figure 2: The coaxial feed is represented by an equivalent magnetic frill current $\bar{M}_s = M_\phi \hat{\phi}$; this is used as the excitation mechanism for computing the microstrip current.

where $\psi(y)$ describes the variation of the longitudinal current in the transverse (i.e. y) direction, and $\alpha_p(x)$ are sinusoidal subsectional basis functions.

The resulting equation may be expressed as

$$\sum_{p=1}^{N_s} \left[\int\int_{S_p} \bar{E}_q(x=h) \cdot \psi(y)\, \alpha_p(x)\, \hat{x} ds \right] I_p = \int\int_{S_f} \bar{H}_q \cdot \bar{M}_s ds \qquad (2)$$

where S_p is the surface area of the p^{th} subsection, S_f is the surface of the coaxial aperture, and $\bar{E}_q, \bar{H}_q$ are the electric and magnetic fields respectively, associated with a test current $\bar{J}_q$ existing over the q^{th} strip subsection.

We may express (2) by the matrix equation

$$[\mathbf{Z}]\,[\mathbf{I}] = [\mathbf{V}]\ . \qquad (3)$$

Here, [Z] is the impedance matrix, [V] is the excitation vector and [I] is the unknown current vector comprised of the complex coefficients I_p.

Finally, after evaluating the elements of [Z] and [V], the matrix equation is solved to compute the current distribution. Based on the current, transmission line theory is used to derive scattering parameters, and (if desired) an equivalent circuit model, to characterize the discontinuity [1,2].

III. RESULTS

An open-end can be represented by an effective length extension L_{eff}, by a shunt capacitance c_{op}, or by the associated reflection coefficient Γ_{op} (= S_{11}). The plot of Figure 3 compares L_{eff} results to those of Jansen et. al. [3] and Itoh [4]. Also shown is the cut-off frequency f_c, which is defined as the lowest frequency where non-evanescent waveguide modes can exist within the cavity. The new results are almost identical to those obtained by Jansen et. al. for frequencies above 8 GHz, but show a reduced value for lower frequencies.

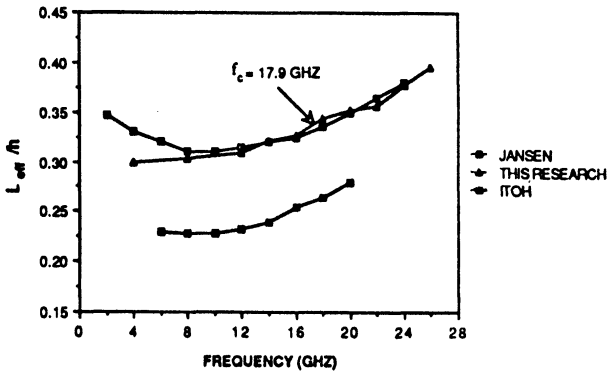

Figure 3: Effective length extension of a microstrip open-end discontinuity, as compared to results from other full-wave analyses (ϵ_r = 9.6, W/h = 1.57, b = .305″, c = .2″, h = .025″).

The results shown in Figure 4 illustrate that shielding effects are significant at high frequencies. The normalized open-end capacitance c_{op} is plotted for three different cavity sizes. The results show that reducing the cavity size raises f_c (as expected), and it lowers the value of c_{op}. For comparison, data obtained from *Super Compact* and *Touchstone* are included.

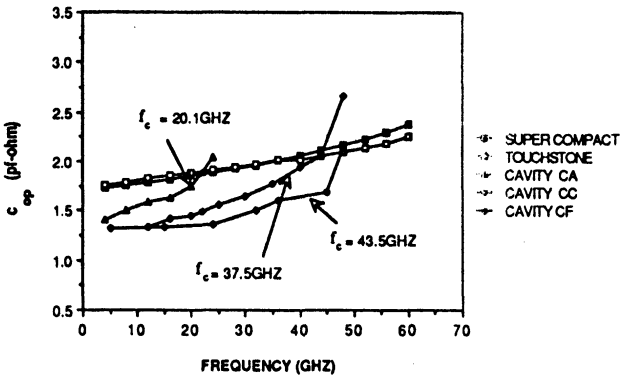

Figure 4: A comparison of the normalized open-end capacitance for three different cavity sizes shows that shielding effects are significant at high frequencies (ϵ_r = 9.7, $W = h$ = .025″; cavity CA: b = c = .25″, cavity CC: b = c =.01″, cavity CF: b = c =.075″).

In the remaining examples, numerical results from the new method are compared to measurements. Figure 5 shows results for the angle of S_{11} of an open-end, and Figure 6 contains results for the magnitude of the transmission coefficient ($/S_{21}/$) for a series gap discontinuity. In both cases, the agreement between the numerical and experimental data is very good.

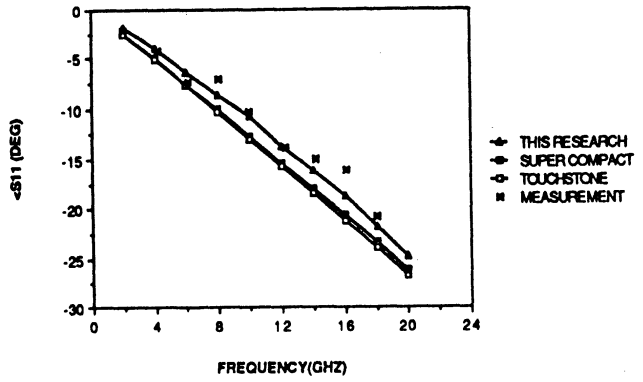

Figure 5: Numerical and measured results show good agreement for the angle of S11 of an open circuit (ϵ_r = 9.7, W = h =.025", b = c =.25").

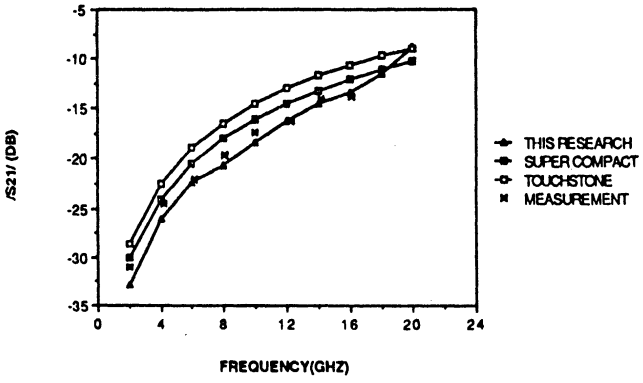

Figure 6: Good agreement with measurements has also been obtained for series gap discontinuities. Shown here is the magnitude of S_{21} for a series gap with a 9 mil gap spacing (ϵ_r = 9.7,W = h = .025", b = c =.25").

Finally, consider the four resonator filter of Figure 7. Numerical results for the magnitude and phase of S_{21}, shown in Figure 8, demonstrate excellent agreement with measurements for frequencies below the cutoff frequency f_c. Above cutoff, the filter measurement is distorted due to waveguide moding within the test fixture.

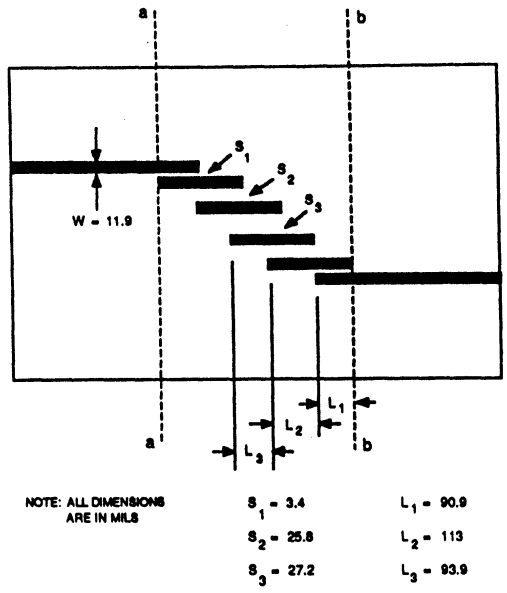

Figure 7: Numerical and experimental results are compared below for this 4 resonator filter (ϵ_r = 9.7, h = .025", b = .4", c = .25").

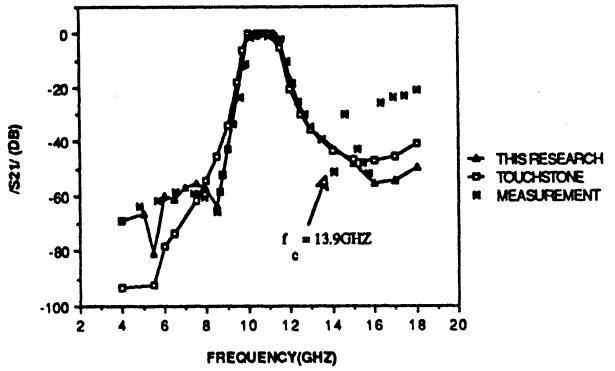

a. Amplitude of S_{21}

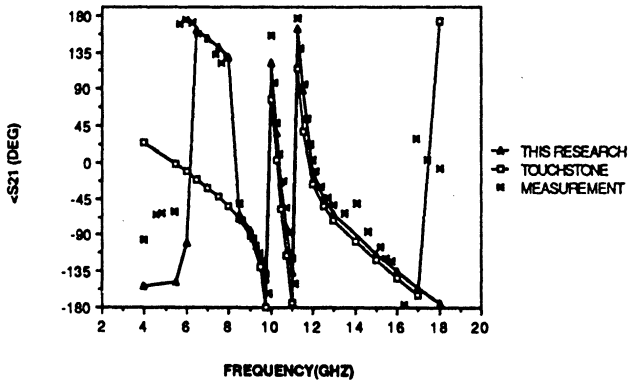

b. Phase of S_{21}

Figure 8: Results for transmission coefficient S_{21} of 4 resonator filter.

IV. CONCLUSIONS

A new analysis method has been described for shielded microstrip discontinuities. Results from this method have demonstrated good agreement with measurements and other numerical results. This method is useful for the evaluation of existing discontinuity models, for the analysis of cases where existing solutions fail –such as when shielding effects are significant–, and for the development of new discontinuity models with improved accuracy for high frequency applications.

ACKNOWLEDGEMENTS

The authors thank Mr. Ed Watkins, Mr. Jim Schellenberg, and Mr. Marcel Tutt for their contributions to this work. This work was primarily sponsored by The National Science Foundation (Contract. No. ECS -8602530). Partial sponsorship was also provided by the Army Research Office (Contract No. DAAL03-87-K-0088) and the Microwave Products Division of Hughes Aircraft Co.

REFERENCES

[1] P. Katehi and N. Alexopoulos,"Frequency Dependent Characteristics of Microstrip Discontinuities in Millimeter-wave Integrated Circuits", *IEEE Trans. Microwave Theory Tech.* Vol. MTT-33 No. 10, Oct. 1985, pp. 1029-1035.

[2] L. Dunleavy and P. Katehi, "A New Method for Discontinuity Analysis in Shielded Microstrip: Theory and Computational Considerations", In preparation.

[3] R. Jansen, and N. Koster, "Accurate Results on the End Effect of Single and Coupled Lines for Use in Microwave Circuit Design " *A.E.U.* Band 34 1980, pp 453-459.

[4] T. Itoh,"Analysis of Microstrip Resonators", *IEEE Trans. Microwave Theory Tech.*, Vol Mtt-24 1974, pp 946-951.

[5] J. Rautio, "An Electromagnetic Time-Harmonic Analysis of Shielded Microstrip Circuits",*IEEE Trans. Microwave Theory Tech.*, Vol. MTT-35, No. 8, pp726-729.

[6] C. Chi and N. Alexopoulos, "Radiation by a Probe Through a Substrate" *IEEE Trans. Antennas Propagat.* vol. AP-34, Sept. 1986, pp 1080-1091.

[7] R. Harrington, *Time-Harmonic Electromagnetic Fields*, McGraw Hill 1961, pp.111-112.

[8] N. Franzen and R. Speciale, "A New Procedure for System Calibration and Error Removal in Automated S-Parameter Measurements", *5th European Microwave Conference*, pp. 69-73.

[9] L. Dunleavy and P. Katehi, "Repeatability Issues for De-embedding Microstrip Discontinuity S-parameter Measurements By the TSD Technique" *Automatic RF Techniques Group (ARFTG) Conf. Dig.* June 1986.

Appendix B

"Shielding Effects in Microstrip Discontinuities
Part I: Theory"
L.P. Dunleavy and P.B. Katehi

Shielding Effects in Microstrip Discontinuities – Part I: Theory

Submitted to IEEE Trans. on Microwave Theory and Tech. – April 1988

L.P. Dunleavy* and P.B. Katehi
Radiation Laboratory
Dept. of Electrical Engineering and Computer Science
The University of Michigan
1301 Beal Avenue
Ann Arbor, MI 48109-2122

Abstract-. A new integral equation method is described for the accurate full-wave analysis of shielded microstrip discontinuities. The integral equation is derived by applying the reciprocity theorem, then solved by the method of moments. In this derivation, a coaxial aperture is modeled with an equivalent magnetic current, and is used as the excitation mechanism for generating the microstrip currents. Computational aspects of the method have been explored extensively. A summary of some of the more interesting conclusions is included.

---

* L.P. Dunleavy is now with Hughes Aircraft Company.

I. INTRODUCTION

The need for more accurate microstrip circuit simulations has become increasingly apparent with the advent of monolithic microwave integrated circuits (MMICs), as well as the increased interest in millimeter-wave and near-millimeter-wave frequencies. The development of more accurate microstrip discontinuity models, based on full-wave analyses, is key to improving high frequency circuit simulations and reducing lengthy design cycle costs. Further, in most applications the microstrip circuit is enclosed in a shielding cavity (or housing) as shown in Figure 1. There are two main conditions where shielding effects are significant. The first occurs when the frequency approaches or is above the cutoff frequency f_c for higher order modes. The second occurs when the metal enclosure is physically close to the circuitry. A full-wave analysis is required to accurately model these effects.

Although shielding effects have been studied to some extent in the past (e.g. [1]), the treatment has been incomplete, particularly for more complicated structures such as a coupled line filter. Further, shielding effects are not accurately accounted for in the discontinuity models of most available microwave CAD software. To address these inadequacies, Part I of this paper develops an accurate method for the analysis of discontinuities in shielded microstrip. The method presented is based on an integral equation approach. The integral equation is derived by an application of reciprocity theorem, then solved by the method of moments.

To derive a realistically based formulation, a coaxial excitation mechanism is used. To date, all full-wave analyses of microstrip discontinuities use either a gap

generator excitation method [2,3,6], or a cavity resonance technique [4,5]. Both of these techniques are purely mathematical tools. The former has no physical basis relative to an actual circuit. The latter is also abstract, since in any practical circuit some form of excitation is present. In fact, one of the most common excitations in practice comes from a coaxial feed (Figure 1). A magnetic current model for such a feed is used in the present treatment as the excitation, and this method is compared to the gap generator method in Part II of the paper.

The emphasis in Part II is on the application of the present theoretical method to study shielding effects in discontinuities. As part of this study, numerical and measured results are presented for the structures of Figure 2, which include open-end and series gap discontinuities, and a coupled line filter. The measured results are seen to be in excellent agreement with the theoretical results from the present research.

The objectives of this research may be summarized as follows: i) Develop a new theoretical method for analysis of shielded microstrip discontinuities (Part I), ii) Explore the use of a practical (i.e. coaxial) excitation mechanism (Part I and II), iii) Investigate high frequency microstrip measurement techniques (Part II), v) Study the effect of shielding on discontinuity behavior (Part II), and iv) Obtain experimental data for verification of the new theoretical method (Part II). In addition, computational aspects of the method are explored extensively.

II. THEORETICAL FORMULATION

The details of the theoretical derivation for the present method are given in [7]. Hence, only a summary of the key steps is described below.

A. Integral Equation

In the theoretical formulation, a few simplifying assumptions are made to reduce unnecessary complexity and excessive computer time. Throughout the analysis, it is assumed that the width of the conducting strips is small compared to the microstrip wavelength λ_g (the "thin-strip" approximation). In this case, the transverse component of the current may be neglected. While substrate losses are accounted for, it is assumed that the strip conductors and the walls of the shielding box are lossless, and that the strip has infinitesimal thickness. These assumptions are valid for the high frequency analysis of the microstrip structures of Figure 2, provided good conductors are used in the metalized areas.

Consider the geometry of Figure 1. In most cases the coaxial feed, or "launcher", is designed to allow only transverse electromagnetic (TEM) propagation, and the feed's center conductor is small compared to a wavelength ($kr_a \ll 1$). In these cases, the radial electric field will be dominant on the aperture and we can replace the feed by an equivalent magnetic surface current $\bar{M}_s$ [8]. This current is sometimes called a "frill" current [9]. The source $\bar{M}_s$ induces the current distribution $\bar{J}_s$ on the conducting strip and produces the total electric field $\bar{E}^{tot}$ and the total magnetic field $\bar{H}^{tot}$ inside the cavity as indicated in Figure 1.

Now consider a cavity geometry similar to Figure 1, with the strip conductors as well as the coaxial input and output removed. Assume a test current $\bar{J}_q$ existing

on a small subsection of the area which was occupied by the strip. The fields inside this new geometry are denoted by $\bar{E}_q$, and $\bar{H}_q$. Using the reciprocity theorem, the two sets of sources ($\bar{M}_s, \bar{J}_s$; and $\bar{J}_q$) are related according to

$$\int\int\int_V \left(\bar{J}_s \cdot \bar{E}_q - \bar{H}_q \cdot \bar{M}_s\right) dv = \int\int\int_V \bar{J}_q \cdot \bar{E}^{tot} dv \tag{1}$$

where V represents the volume of the interior of the cavity.

Since $\bar{J}_q \cdot \bar{E}^{tot}$ is zero everywhere inside the cavity, the right hand side of (1) vanishes. Reducing the remaining volume integrals in (1) to surface integrals results in

$$\int\int_{S_{strip}} \bar{E}_q(z=h) \cdot \bar{J}_s ds = \int\int_{S_f} \bar{H}_q(x=0) \cdot \bar{M}_s ds \tag{2}$$

where S_{strip} is the surface of the conducting strip and S_f is the surface of the coaxial aperture(s). For one-port discontinuities, S_f represents the surface of the feed on the left hand side of Figure 1, while for two-port discontinuities, S_f represents both feed surfaces. An integral equation similar to (2) can be derived for the case of gap generator excitation by setting $\bar{M}_s = 0$ and assuming that E_x is non-zero at one point on the strip [7].

In order to solve the integral equation (2), the current distribution $\bar{J}_s$ is expanded into a series of orthonormal functions as follows [1]:

$$\bar{J}_s = \psi(y) \sum_{p=1}^{N_s} I_p \alpha_p(x)\, \hat{x} \tag{3}$$

where I_p are unknown current coefficients and N_s is the number of sections considered on the strip (Figure 3). The function $\psi(y)$ describes the variation of the

[1] The assumed time dependence is $e^{j\omega t}$.

current in the transverse direction and is given by [2,10]

$$\psi(y) = \begin{cases} \frac{\frac{2}{\pi W}}{\sqrt{1-\left[\frac{2(y-Y_0)}{W}\right]^2}} & Y_0 - W/2 \le y \le Y_0 + W/2 \\ 0 & \text{otherwise} \end{cases} \tag{4}$$

where W is the width of the microstrip line and Y_0 is the y-coordinate of the center of the strip with respect to the origin in Figure 1.

The basis functions $\alpha_p(x)$ are described by

$$\alpha_p(x) = \begin{cases} \frac{\sin[K(x_{p+1}-x)]}{\sin(Kl_x)} & x_p \le x \le x_{p+1} \\ \frac{\sin[K(x-x_{p-1})]}{\sin(Kl_x)} & x_{p-1} \le x \le x_p \\ 0 & \text{otherwise} \end{cases} \tag{5}$$

for $p \neq 1$, and

$$\alpha_1(x) = \begin{cases} \frac{\sin[K(l_x-x)]}{\sin(Kl_x)} & 0 \le x \le l_x \\ 0 & \text{otherwise} \end{cases} \tag{6}$$

for $p = 1$, where

K is a scaling factor, taken to be equal to the wave number in the dielectric

x_p is the x-coordinate of the pth subsection $(= (p-1)l_x)$

l_x is the subsection length $(l_x = x_{p+1} - x_p)$.

For computation, all of the geometrical parameters are normalized with respect to the dielectric wavelength (λ_d); hence the normalized scaling factor is equal to 2π.

The integral equation (2) can now be transformed into a matrix equation by substituting the expansion of (3) for the current $\bar{J}_s$. The result may be put in the form

$$[\mathbf{Z}]\,[\mathbf{I}] = [\mathbf{V}] \ . \tag{7}$$

In the above, [Z] is an $N_s \times N_s$ impedance matrix, [I] is a vector comprised of the unknown current coefficients I_p, and [V] is the excitation vector. The individual elements of the impedance matrix are given by

$$Z_{qp} = \int\int_{S_p} \bar{E}_q(z=h) \cdot \hat{x}\psi(y)\,\alpha_p(x)\,ds\,. \tag{8}$$

where S_p is the area of the two subsections on either side of the point x_p. The elements of the excitation vector are found according to

$$V_q = \int\int_{S_f} \bar{H}_q \cdot \bar{M}_s ds\,. \tag{9}$$

Once the elements of the impedance matrix and excitation vector have been computed, the current distribution is found by solving (7) as follows:

$$[\mathbf{I}] = [\mathbf{Z}]^{-1}[\mathbf{V}]\,. \tag{10}$$

B. Evaluation of impedance matrix elements

Before evaluating the elements of the impedance matrix, the Green's function associated with the electric current $\bar{J}_q$ is derived. To do this the cavity is divided into two regions: region 1 consists of the volume contained within the substrate ($z < h$), while region 2 is the volume above the substrate surface ($z > h$).

The integral form of the electric field is given in terms of the Green's function, by

$$\bar{E}_q^{\,i} = -j\omega\mu_0 \int\int\int_V \left[\left(\bar{\bar{I}} + \frac{1}{k_i^2}\bar{\nabla}\bar{\nabla}\right)\cdot(\bar{\bar{G}}^i)^T\right]\cdot \bar{J}dv' \tag{11}$$

where $k_i^2 = \omega^2\mu_0\epsilon_i$. The index i indicates that the above holds in each region (i.e. for $i = 1, 2$).

In (11), $\bar{\bar{G}}^i$ is a dyadic Green's function [11] satisfying the following equation

$$\nabla^2\bar{\bar{G}}^i + k_i^2\bar{\bar{G}}^i = -\bar{\bar{I}}\delta(\bar{r} - \bar{r}')\,. \tag{12}$$

where $\bar{\bar{I}}$ is the unit dyadic ($= \hat{x}\hat{x} + \hat{y}\hat{y} + \hat{z}\hat{z}$), $\bar{r}$ is the position vector of a field point anywhere inside the cavity, and $\bar{r}'$ is the position vector of an infinitesimal current source.

Because of the existence of an air/dielectric interface, and the assumption of a unidirectional current, the dyadic Green's function will have the form

$$\bar{\bar{G}}^i = G^i_{xx}\hat{x}\hat{x} + G^i_{xz}\hat{x}\hat{z} \,. \tag{13}$$

The dyadic components of (13) are found by applying appropriate boundary conditions at the walls: $x = 0$, and a ; $y = 0$, and b ; and $z = 0$, c ; and at the air-dielectric interface [7]. These components may be expressed as

$$G^{(1)}_{xx} = \sum_{m=1}^{\infty}\sum_{n=0}^{\infty} A^{(1)}_{mn} \cos k_x x \sin k_y y \sin k^{(1)}_z z \tag{14}$$

$$G^{(1)}_{xz} = \sum_{m=1}^{\infty}\sum_{n=0}^{\infty} B^{(1)}_{mn} \sin k_x x \sin k_y y \cos k^{(1)}_z z \tag{15}$$

$$G^{(2)}_{xx} = \sum_{m=1}^{\infty}\sum_{n=0}^{\infty} A^{(2)}_{mn} \cos k_x x \sin k_y y \sin k^{(2)}_z (z-c) \tag{16}$$

$$G^{(2)}_{xz} = \sum_{m=1}^{\infty}\sum_{n=0}^{\infty} B^{(2)}_{mn} \sin k_x x \sin k_y y \cos k^{(2)}_z (z-c) \tag{17}$$

where

$$k_x = n\pi/a \tag{18}$$

$$k_y = m\pi/b \tag{19}$$

$$k^{(1)}_z = \sqrt{k_1^2 - k_x^2 - k_y^2} \tag{20}$$

$$k^{(2)}_z = \sqrt{k_0^2 - k_x^2 - k_y^2} \tag{21}$$

$$k_1 = \omega\sqrt{\mu_0\epsilon_1} \tag{22}$$

$$k_0 = \omega\sqrt{\mu_0\epsilon_0} \,, \tag{23}$$

and

$$A_{mn}^{(1)} = \frac{-\varphi_n \cos k_x x' \sin k_y y' \tan k_z^{(2)}(h-c)}{abd_{1mn} \cos k_z^{(1)} h} \tag{24}$$

$$A_{mn}^{(2)} = \frac{-\varphi_n \cos k_x x' \sin k_y y' \tan k_z^{(1)} h}{abd_{1mn} \cos k_z^{(2)}(h-c)} \tag{25}$$

$$B_{mn}^{(1)} = \frac{-\varphi_n(1-\epsilon_r^*)k_x \cos k_x x' \sin k_y y' \tan k_z^{(1)} h \tan k_z^{(2)}(h-c)}{abd_{1mn}d_{2mn} \cos k_z^{(1)} h} \tag{26}$$

$$B_{mn}^{(2)} = \frac{-\varphi_n(1-\epsilon_r^*)k_x \cos k_x x' \sin k_y y' \tan k_z^{(1)} h \tan k_z^{(2)}(h-c)}{abd_{1mn}d_{2mn} \cos k_z^{(2)}(h-c)} \tag{27}$$

In (24)-(27), ϵ_r^* is the complex dielectric constant of the substrate and

$$\varphi_n = \begin{cases} 2 & \text{for } n = 0 \\ 4 & \text{for } n \neq 0 \end{cases} \tag{28}$$

$$d_{1mn} = k_z^{(2)} \tan k_z^{(1)} h - k_z^{(1)} \tan k_z^{(2)}(h-c) \tag{29}$$

$$d_{2mn} = k_z^{(2)} \epsilon_r^* \tan k_z^{(2)}(h-c) - k_z^{(1)} \tan k_z^{(1)} h \, . \tag{30}$$

In view of (11)-(30), the elements of the impedance matrix may be put in the following form [2]:

$$Z_{qp} = \frac{j\omega\mu_0 K^2 l_x^4}{16ab \sin^2 K l_x} \zeta_q \zeta_p \sum_{n=0}^{NSTOP} \varphi_n \cos k_x x_q \cos k_x x_p \cdot \left[\text{Sinc}\left[\frac{1}{2}(k_x + K)l_x\right] \text{Sinc}\left[\frac{1}{2}(k_x - K)l_x\right]\right]^2 LN(n) \tag{31}$$

with $LN(n)$ given by the series

$$LN(n) = \sum_{m=1}^{MSTOP} L_{mn} \, . \tag{32}$$

The series elements L_{mn} are given by

[2] The expression given here for the impedance matrix elements, and that given shortly for the excitation vector elements apply to the case of an open-end or series gap. Slight modifications are necessary for analysis of parallel coupled line filters.

$$L_{mn} = \frac{\varphi_n[\sin(k_y Y_0) J_0\left(\frac{k_y W}{2}\right)]^2 \tan k_z^{(1)} h \tan k_z^{(2)}(h-c)}{\left[k_z^{(2)} \tan k_z^{(1)} h - k_z^{(1)} \tan k_z^{(2)}(h-c)\right]} \cdot \frac{\left[k_z^{(2)} \epsilon_r^* \left(1 - \frac{k_x^2}{k_1^2}\right) \tan k_z^{(2)}(h-c) - k_z^{(1)} \left(1 - \frac{k_x^2}{k_0^2}\right) \tan k_z^{(1)} h\right]}{\left[k_z^{(2)} \epsilon_r^* \tan k_z^{(2)}(h-c) - k_z^{(1)} \tan k_z^{(1)} h\right]}, \quad (33)$$

where Y_0 is the y-coordinate of of the center of the strip, and

$$\mathrm{Sinc}(t) = \begin{cases} \frac{\sin t}{t} & \text{for } t \neq 0 \\ 1 & \text{for } t = 0 \end{cases} \quad (34)$$

$$\zeta_q = \begin{cases} 2 & \text{for } q = 1 \\ 4 & \text{otherwise} \end{cases} \quad (35)$$

$$R_{1n} = \frac{1}{2}(k + k_x) l_x \quad (36)$$

$$R_{2n} = \frac{1}{2}(k - k_x) l_x \,. \quad (37)$$

C. Evaluation of the Excitation Vector Elements

The formulation for the excitation vector elements for the one-port case will now be carried out. The case for two-port excitation is a straightforward extension [7].

To evaluate the excitation vector elements according to (9), we need to find the magnetic field $\bar{H}_q$ and the frill current $\bar{M}_s = M_\phi \hat{\phi}$. An approximate expression for the frill current is given by [8]

$$\bar{M}_s = -\frac{V_0}{\rho \ln\left(\frac{r_b}{r_a}\right)} \hat{\phi} \quad (38)$$

where

V_0 is the complex voltage applied by the coaxial line at the feeding point

r_b is the radius of the coaxial feed's outer conductor

r_a is the radius of the coaxial feed's inner conductor

ρ, ϕ are cylindrical coordinates referenced to the feed's center.

Substituting from (38) into (9) yields (with $ds = \rho d\rho d\phi$)

$$\begin{aligned} V_q &= -\frac{V_0}{\ln\left(\frac{r_b}{r_a}\right)} \int\int_{S_f} H^i_{q\phi}(x=0) d\rho d\phi \\ &= -\frac{V_0}{\ln\left(\frac{r_b}{r_a}\right)} \left[\int\int_{S_f^{(1)}} H^{(1)}_{q\phi}(x=0) d\rho d\phi + \int\int_{S_f^{(2)}} H^{(2)}_{q\phi}(x=0) d\rho d\phi \right] \end{aligned} \quad (39)$$

where

$S_f^{(1)}$ is the portion of the feed surface below the substrate/air interface ($z'' = \rho \sin\phi \leq -t$)

$S_f^{(2)}$ is the portion of the feed surface above the substrate ($z'' = \rho \sin\phi \geq -t$)

$H^{(1)}_{q\phi}(x=0)$ and $H^{(2)}_{q\phi}(x=0)$ are the $\hat{\phi}$ components of the magnetic field, in regions 1 and 2 respectively, evaluated on the plane of the aperture.

After solving for the magnetic fields $H^i_{q\phi}(x=0)$ and substituting the resulting expressions into (39), the following formulation is produced for excitation vector elements:

$$\begin{aligned} V_q &= \frac{-V_0 \zeta_q K l_x^2}{\ln\left(\frac{r_b}{r_a}\right) 4ab \sin K l_x} \sum_{n=0}^{NSTOP} \cos k_x x_q \\ &\quad \cdot \mathrm{Sinc}\left[\frac{1}{2}(k_x + K) l_x\right] \mathrm{Sinc}\left[\frac{1}{2}(k_x - K) l_x\right] [MN(n)] \end{aligned} \quad (40)$$

where $MN(n)$ is expressed in terms of the series given by

$$MN(n) = \sum_{m=1}^{MSTOP} M_{mn} \,. \quad (41)$$

The series elements M_{mn} are given by the following integral

$$
\begin{aligned}
M_{mn} &= \int\int_{S_f} \mathcal{M}^i_{mn}\, d\rho\, d\phi \\
&= \int\int_{S_f^{(1)}} \mathcal{M}^{(1)}_{mn}\, d\rho\, d\phi + \int\int_{S_f^{(2)}} \mathcal{M}^{(2)}_{mn}\, d\rho\, d\phi\,. \qquad (42)
\end{aligned}
$$

The above integrations are performed numerically, with the integrands $\mathcal{M}^i_{mn}$ given by

$$
\begin{aligned}
\mathcal{M}^{(1)}_{mn} &= \cos\phi\, c^{(1)}_{zmn} \cos k_y(\rho\cos\phi + Y_c) \sin k_z^{(1)}(\rho\sin\phi + h_c) \\
&\quad - \sin\phi\, c^{(1)}_{ymn} \sin k_y(\rho\cos\phi + Y_c) \cos k_z^{(1)}(\rho\sin\phi + h_c) \qquad (43)
\end{aligned}
$$

for ρ and ϕ in region 1, and

$$
\begin{aligned}
\mathcal{M}^{(2)}_{mn} &= \cos\phi\, c^{(2)}_{zmn} \cos k_y(\rho\cos\phi + Y_c) \sin k_z^{(2)}(\rho\sin\phi - c + h_c) \\
&\quad - \sin\phi\, c^{(2)}_{ymn} \sin k_y(\rho\cos\phi + Y_c) \cos k_z^{(2)}(\rho\sin\phi - c + h_c)\,. \qquad (44)
\end{aligned}
$$

for ρ and ϕ in region 2. In (43), and (44) Y_c, and h_c are the the y and z coordinates of the coaxial feed, and

$$
\begin{aligned}
c^{(1)}_{ymn} &= \frac{c^{(1)}_{zmn}}{k_y d_{2mn}} \Big\{ k_z^{(1)} k_z^{(2)} \epsilon_r^* \tan k_z^{(2)}(h-c) \\
&\quad - \left[(k_z^{(1)})^2 + k_x^2(1-\epsilon_r^*) \right] \tan k_z^{(1)} h \Big\} \qquad (45) \\
c^{(1)}_{zmn} &= \frac{\varphi_n k_y \tan k_z^{(2)}(h-c)}{d_{1mn} \cos k_z^{(1)} h} \sin k_y Y_0\, J_0(k_y \frac{W}{2}) \qquad (46) \\
c^{(2)}_{ymn} &= \frac{c^{(2)}_{zmn}}{k_y d_{2mn}} \Big\{ k_z^{(1)} k_z^{(2)} \tan k_z^{(1)} h \\
&\quad - \left[(k_z^{(2)})^2 \epsilon_r^* - k_x^2(1-\epsilon_r^*) \right] \tan k_z^{(2)}(h-c) \Big\} \qquad (47) \\
c^{(2)}_{zmn} &= \frac{\varphi_n k_y \tan k_z^{(1)} h}{d_{1mn} \cos k_z^{(2)}(h-c)} \sin k_y Y_0\, J_0(k_y \frac{W}{2})\,. \qquad (48)
\end{aligned}
$$

The above outlines the theory for computing the current distribution on the conducting strips of shielded microstrip discontinuities. The next step is to use the

current distribution to derive the network parameters of the discontinuity under consideration. As shown in Figure 4, an open-end discontinuity can be represented by an effective length extension L_{eff} or by an equivalent capacitance C_{op}. For a two-port network, a general scattering parameter representation is used. The effective dielectric constant ϵ_{eff} is calculated from the distance between two adjacent maxima of the current distribution on a straight microstrip line. The theory for deriving these network parameters is described for elsewhere [2,7,12], and a brief summary is given in Appendix I.

The theoretical method developed above has been implemented in a Fortran program. The remainder of the paper addresses computational aspects of the solution for the current distribution and discontinuity network parameters.

III. COMPUTATION OF CURRENT DISTRIBUTION

To gain insight into the nature of the computations, we will now examine plots of a typical impedance matrix, excitation vector, and current distribution for an open-ended microstrip line.

Figure 5 shows the amplitude distribution of a typical impedance matrix. It is seen that the amplitude of the diagonal elements is the greatest and it tapers off uniformly as one moves away from the diagonal. Another observation is that the matrix is symmetric such that $Z_{qp} = Z_{pq}$ for any p and q, which is expected from (31). When the impedance matrix of Figure 5 is inverted, the amplitude distribution is as shown in Figure 6. The inverted impedance matrix shows a sinusoidal shape for any given row or column.

Figure 7 shows the amplitude distribution for the excitation vector. The ampli-

tude is highest over the subsection closest to the feed then tapers off smoothly. In contrast, the excitation vector for the gap generator method has only one non-zero value, at the position of the source.

Multiplying the inverted impedance matrix by the excitation vector of Figure 7 yields the current distribution of Figure 8. It can be seen that the shape of the current is similar to that exhibited by the first column of the impedance matrix. This is not surprising given the shape of the excitation vector.

IV. CONVERGENCE OF Z_{qp} AND V_q

In the expressions of (31), and (40) for the impedance matrix and excitation vector elements, the summations over m and n are theoretically infinite. The number of elements included in these series depends on the convergence behavior of Z_{qp} and V_q with the summation indices.

As seen from (31), the convergence of the impedance matrix is described mainly by the convergence of $LN(n)$. Figure 9 shows the typical variation of $LN(n)$ with m and n. Most of the contributions from $LN(n)$ to the impedance matrix are concentrated in the first several n values. The convergence over m is good, and it appears that performing the computations out to $m = 200$ may be sufficient. Note, however, that the allowable truncation points for the summations over m and n vary with the geometry. The values quoted here are for illustration purposes only.

The computation of Z_{qp} over n is illustrated for a typical impedance matrix in Figure 10. Shown is the convergence behavior for one row ($q = 32$) of the 64 x 64 element impedance matrix of Figure 5. This behavior is representative of that for

any row. After only a few terms the diagonal element ($p = q = 32$) rises above the others, and after adding 100 terms the amplitude distribution is well formed.

Similar conclusions can be drawn for the convergence of the excitation vector elements with respect to the summation indices m and n.

V. CONVERGENCE OF NETWORK PARAMETERS

The convergence behavior of the elements of the impedance matrix and excitation vector is important to examine, yet the more relevant question remains: how are the final results affected by various convergence related parameters?

To answer this question, a series of numerical experiments were carried out, and the main results are presented here. As illustrated in Figure 4, an open end discontinuity can be represented by either an effective length extension L_{eff} or an equivalent capacitance c_{op}. The microstrip effective dielectric constant ϵ_{eff} is calculated from the distance between two adjacent maxima of the open-end current distribution (Figure 8).

The experiments investigated the convergence behavior of L_{eff} and ϵ_{eff} with respect to the sampling rate N_x $(= 1/l_x)$, and the truncation points $NSTOP$, $MSTOP$ for the summations over n and m respectively. These numerical experiments have been grouped into three separate categories each exploring a different aspect of the convergence behavior [3].

[3]The parameters used for the plots shown in this section are the following: $\epsilon_r = 9.7, W = h = .025'', a = 3.5'', b = c = .25'', f = 18$GHz.

A. Effect of K-value

Using the program mentioned above, data was generated to plot L_{eff} and ϵ_{eff} versus N_x for several different values of the normalized scaling factor K of (5) and (6). Figure 11a shows the convergence behavior of L_{eff} for a typical case. It is seen that a relatively flat convergence region exists for all the K-values between about 40 and 100 samples per wavelength. Outside this region the convergence behavior depends on K.

At first glance, it appears that the best convergence is achieved for higher K-values (e.g. $K = 8\pi$); however, quite the opposite conclusion results from examining the ϵ_{eff} computation. As can be seen from Figure 11b, the best convergence for ϵ_{eff} is obtained for low K-values.

Based on these and other observations [7], it was determined that a value of $K = 2\pi$ gives the best convergence behavior for the L_{eff} and ϵ_{eff} computations.

B. L_{eff}, ϵ_{eff} Convergence on n and m

To investigate the convergence of the network parameter computations with the summation index n, several program runs were executed for different values of $NSTOP$, with $MSTOP$ fixed at 1000. Data was generated to plot L_{eff} and ϵ_{eff} versus n for several l_x values. Figure 12a shows that for all the l_x values, good convergence on n is achieved after 500 terms. The same can be said for the convergence of ϵ_{eff}.

In examining the convergence behavior with n it was found that, for a given subsection length l_x, cavity length a, and truncation point $NSTOP$, a maximum sampling limit exists beyond which the computed current becomes completely

erratic. This is called the erratic current condition and is given by the following simple relationship:

$$NSTOP * l_x < a \quad \text{or} \quad N_x > \frac{NSTOP}{a}. \tag{49}$$

To investigate the convergence behavior with respect to the summation index m, $NSTOP$ was fixed at 500, and the program was run for different values of $MSTOP$. Figure 12b shows that L_{eff} converges well on m after about 500 terms. The convergence behavior of ϵ_{eff} on m, was found to be similar to that for L_{eff}.

C. Optimum Sampling Range

In this last numerical experiment, the effect of varying l_x on the numerical accuracy of the matrix solution was examined. This was done by studying the variation of the matrix condition number [13], with respect to l_x for a fixed matrix size . After studying several cases it was found that an optimum sampling range, may be defined by the following choice of subsection length l_x

$$\frac{1.5a}{NSTOP} \leq l_x \leq \frac{4a}{NSTOP}. \tag{50}$$

Sampling within this range automatically avoids the erratic current condition and provides the best accuracy in the matrix solution, and also in the solution for network parameters.

To support this last claim, consider the plot of Figure 13. It is seen that the optimum sampling region specified by (50) coincides directly with the flat convergence region for the L_{eff} calculation. This consistency between the optimum sampling region and the flat convergence region for the L_{eff} calculation was observed in all the cases examined [7].

VI. SUMMARY AND CONCLUSIONS

In the theoretical part of the presented research, a method of moments formulation for the shielded microstrip problem was derived based on a more realistic excitation model than used with previous techniques. The formulation follows from the reciprocity theorem, with the use of a frill current model for the coaxial feed.

Computational considerations for implementing the theoretical solution were studied extensively. Several numerical experiments were presented that explored the convergence and the stability of the solution. Most significantly, it was found that an erratic current condition and an optimum sampling range exist; both of these are given by very simple relationships.

Using the method presented here, Part II concentrates on the theoretical and experimental characterization of the discontinuities of Figure 2, and studies the effects of shielding on their behavior.

APPENDIX I

A. One-Port Network Parameters (Open-End Discontinuity)

The effective length extension (Figure 4) for an open-end discontinuity is given by

$$L_{eff} = \frac{\lambda_g}{4} - d_{max} \,. \tag{51}$$

where d_{max} is the distance from the end of the line to a current maximum.

The normalized equivalent capacitance (Figure 4) can be expressed as

$$c_{op} = \frac{\sin 2\beta_g d_{max}}{\omega(1 - \cos 2\beta_g d_{max})} = \frac{\sin 2\beta_g L_{eff}}{\omega(1 + \cos 2\beta_g L_{eff})} \,. \tag{52}$$

In the above, β_g is the phase constant of microstrip transmission line.

B. Two-Port Network Parameters (Gap discontinuity, Coupled Line Filters)

For the computation of two-port network parameters, the strip geometry is assumed to be physically symmetric with respect to the center of the cavity (in both the x and y directions of Figure 1). The network parameters are determined by analyzing the currents from the even and odd mode excitations as discussed in [2,7,12].

The normalized impedance parameters are given by according to

$$z_{11} = \frac{z^e_{IN} + z^o_{IN}}{2} \tag{53}$$

$$z_{12} = \frac{z^o_{IN} - z^e_{IN}}{2} \,. \tag{54}$$

where z^e_{IN} and z^o_{IN} are the input impedances of the even and odd mode networks. The scattering parameters for the network may be derived using the following

Appendix C

"Shielding Effects in Microstrip Discontinuities
Part II: Applications"
L.P. Dunleavy and P.B. Katehi

Shielding Effects in Microstrip Discontinuities – Part II: Applications

Submitted to IEEE Trans. on Microwave Theory and Tech. – April 1988

L.P. Dunleavy* and P.B. Katehi
Radiation Laboratory
Dept. of Electrical Engineering and Computer Science
The University of Michigan
1301 Beal Avenue
Ann Arbor, MI 48109-2122

Abstract-.

As an application of the theoretical method described in a companion paper, numerical and measured results are presented for open-end and series gap discontinuities, and a coupled line filter. Comparisons are also made to commercially available CAD package predictions. The results verify the accuracy of the new theoretical method and demonstrate the effects of shielding on discontinuity behavior. The experimental techniques used, which involve the thru-short-delay de-embedding approach, are also explained.

---

* L.P. Dunleavy is now with Hughes Aircraft Company.

relations:

$$S_{11} = S_{22} = \frac{z_{11}^2 - 1 - z_{12}^2}{D} \tag{55}$$

$$S_{12} = S_{21} = \frac{2z_{12}}{D} \tag{56}$$

where

$$D = z_{11}^2 + 2z_{11} - z_{12}^2 \tag{57}$$

ACKNOWLEDGEMENTS

The authors thank Mr. Ed Watkins, Mr. Jim Schellenberg, and Mr. Marcel Tutt for their contributions to this work. This work was primarily sponsored by The National Science Foundation (Contract. No. ECS -8602530). Partial sponsorship was also provided by the Army Research Office (Contract No. DAAL03-87-K-0088) and the Microwave Products Division of Hughes Aircraft Co.

References

[1] R.H. Jansen, and N.H.L. Koster, "Accurate Results on the End Effect of Single and Coupled Lines for Use in Microwave Circuit Design " *A.E.U.* vol. 34, pp 453-459, 1980.

[2] P.B. Katehi and N.G. Alexopoulos,"Frequency-Dependent Characteristics of Microstrip Discontinuities in Millimeter-wave Integrated Circuits", *IEEE*

Trans. Microwave Theory Tech. vol. MTT-33 No. 10, pp. 1029-1035, Oct. 1985.

[3] R.H. Jansen, and W. Wertgen, "Modular Source-Type 3D Analysis of Scattering Parameters for General Discontinuities, Components and Coupling Effects in (M)MICs", *Proc.* 17^{th} *Eur. Microwave Conf.(Rome) 1987*, pp. 427-432.

[4] R.H. Jansen, "Hybrid Mode Analysis of End Effects of Planar Microwave and Millimeter-Wave Transmission Lines", *Proc. Inst. Elec. Eng.*, vol 128, pp. 77-86, Apr. 1981.

[5] T. Itoh,"Analysis of Microstrip Resonators", *IEEE Trans. Microwave Theory Tech.*, vol MTT-22, pp 946-951, 1974.

[6] J.C. Rautio, "An Electromagnetic Time-Harmonic Analysis of Shielded Microstrip Circuits",*IEEE Trans. Microwave Theory Tech.*, vol. MTT-35, pp726-729, 1987.

[7] L.P. Dunleavy, "Discontinuity Characterization in Shielded Microstrip: A Theoretical and Experimental Study", Ph.D. dissertation, University of Michigan, April 1988.

[8] R.F. Harrington, *Time-Harmonic Electromagnetic Fields*, McGraw Hill 1961, pp.111-112.

[9] C. Chi and N.G. Alexopoulos, "Radiation by a Probe Through a Substrate" *IEEE Trans. Antennas Propagat.* vol. AP-34, Sept. 1986, pp 1080-1091.

[10] J.C. Maxwell, *A Treatise on Electricity and Magnetism* 3rd. ed., vol. 1,New York: Dover 1954 pp 296-297.

[11] C.T. Tai, *Dyadic Green's Functions in Electromagnetic Theory* , Intext Educational Publishers 1971.

[12] P.B. Katehi, "Radiation Losses in MM-Wave Open Microstrip Filters," *Electromagnetics* 7, pp137-152, 1987.

[13] G.H. Golub and C.F. Van Loan, *Matrix Computations*, John Hopkins University Press, 1983, pp26-27.

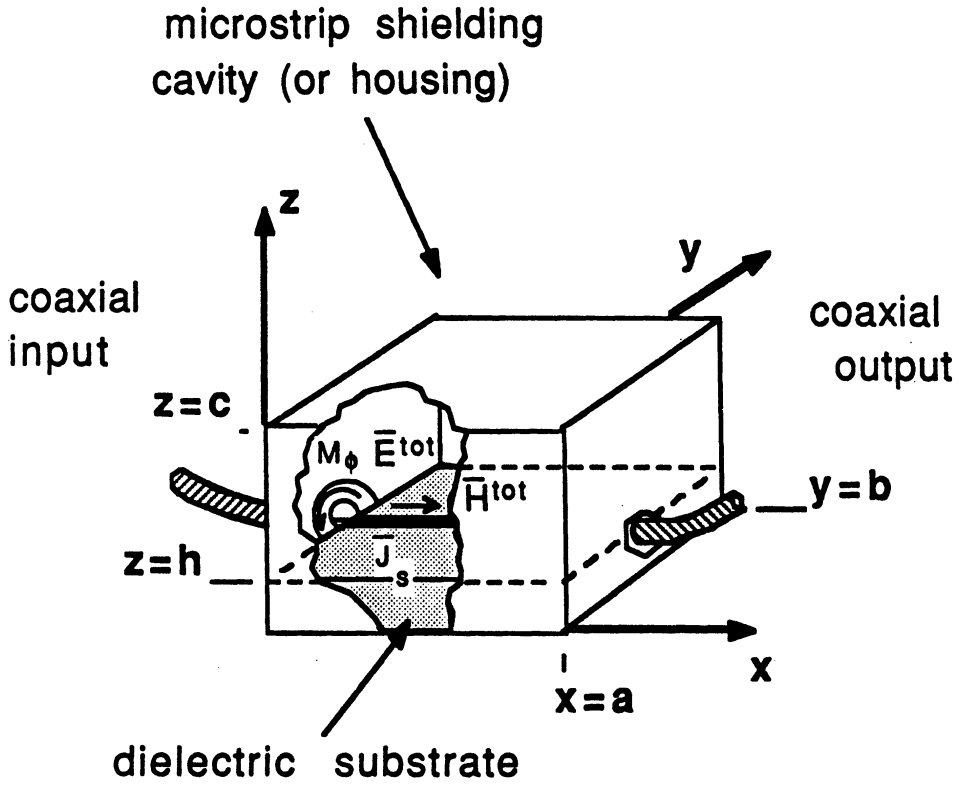

Figure 1: In most practical designs, microstrip circuitry is enclosed in a shielding cavity whose effects must be accurately modeled.

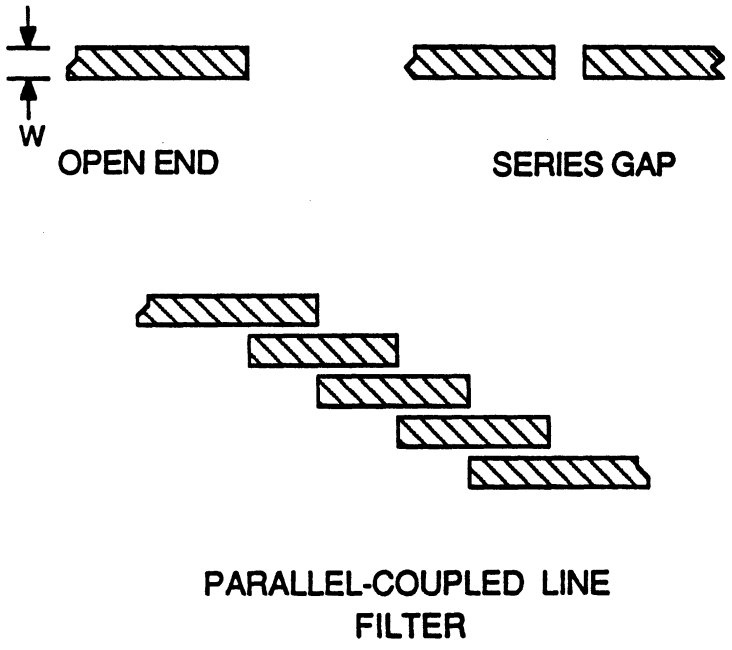

Figure 2: In the present research, the theoretical method is applied to the class of discontinuity structures shown here.

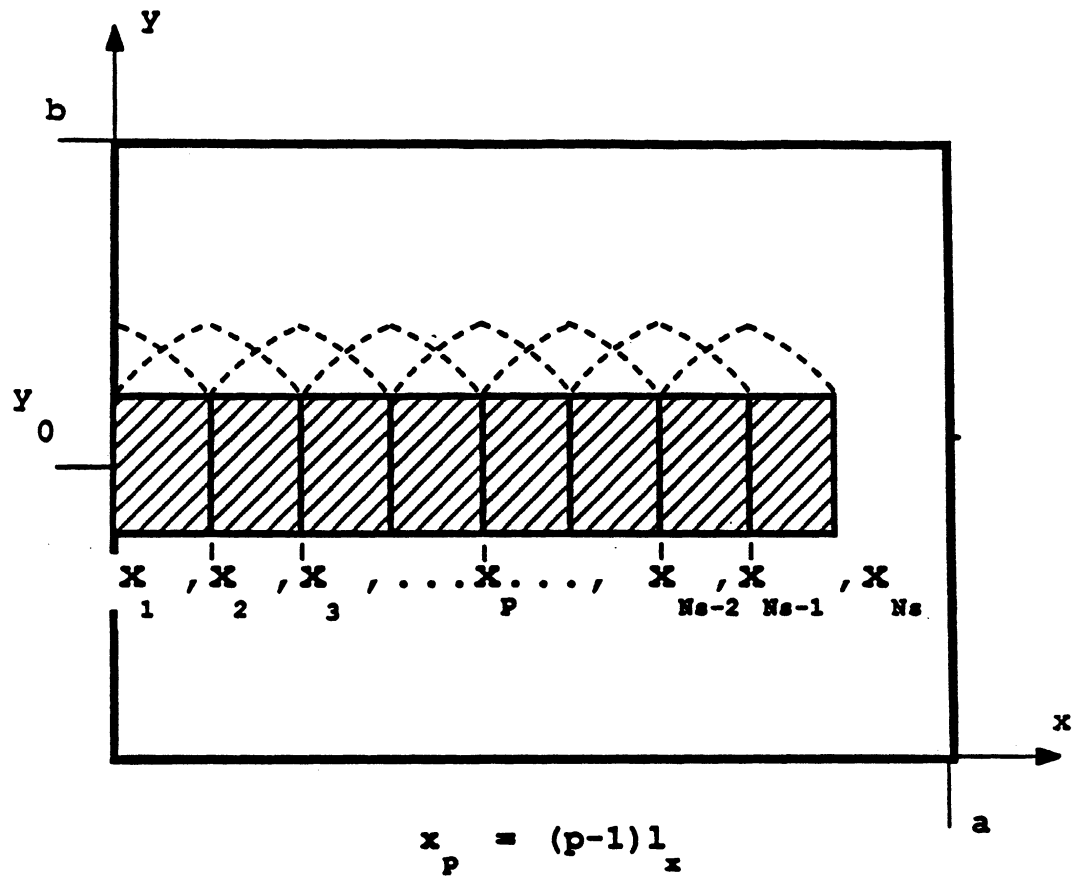

Figure 3: The current in the longitudinal direction is expanded using overlapping sinusoidal basis functions.

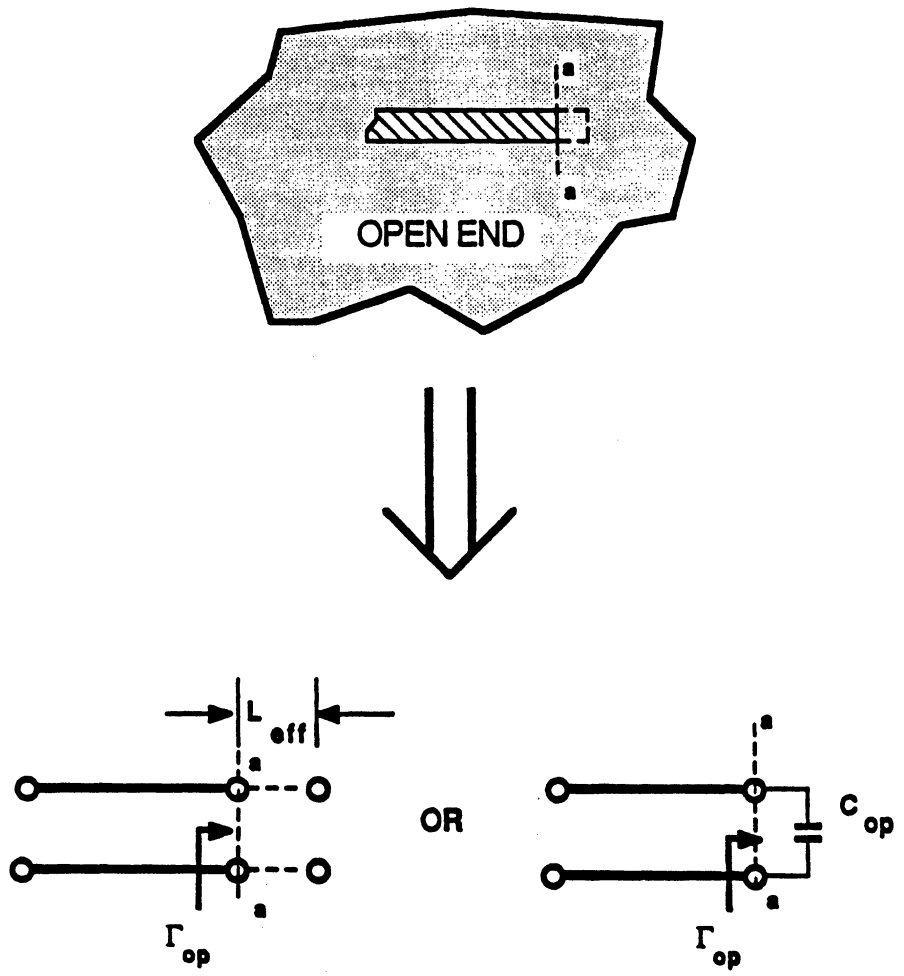

Figure 4: A shielded microstrip open-end can be represented by an effective length extension L_{eff}, or by an equivalent capacitance C_{op}.

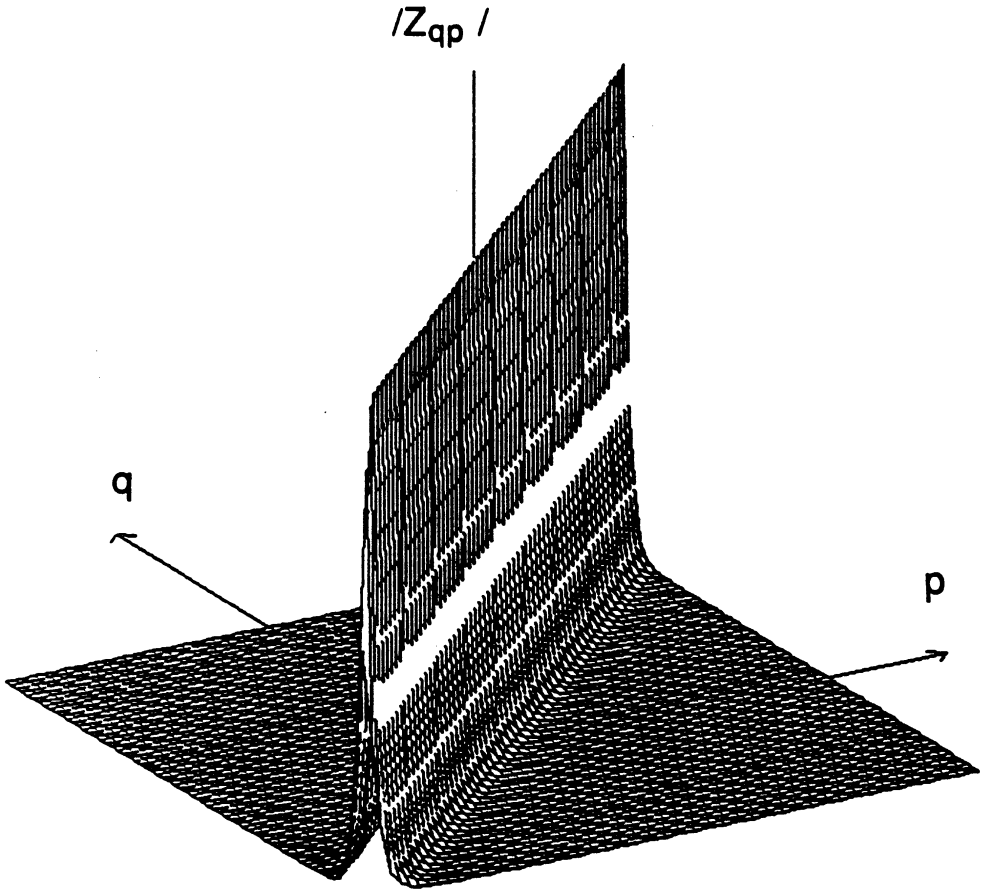

Figure 5: The impedance matrix for an open-end is diagonally dominant.

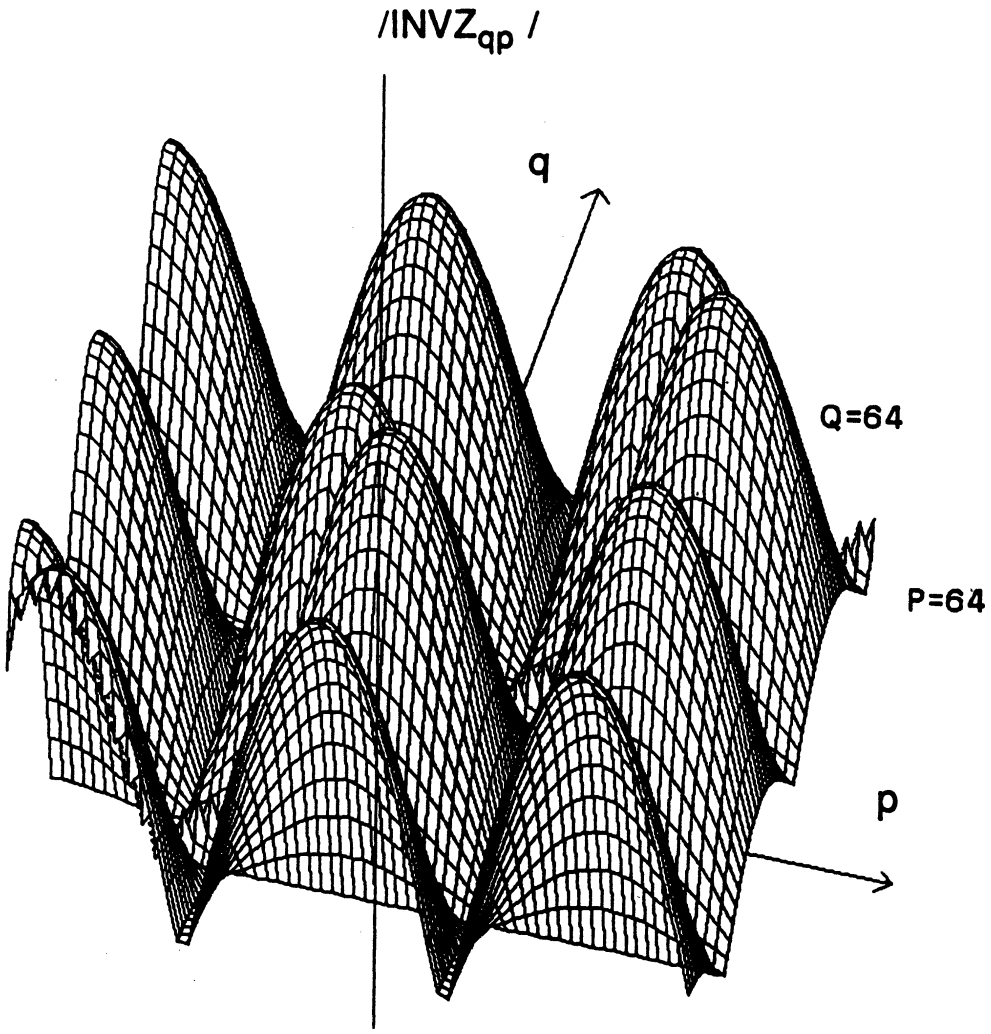

Figure 6: **The inverted impedance matrix displays a sinusoidal shape along any row or column.**

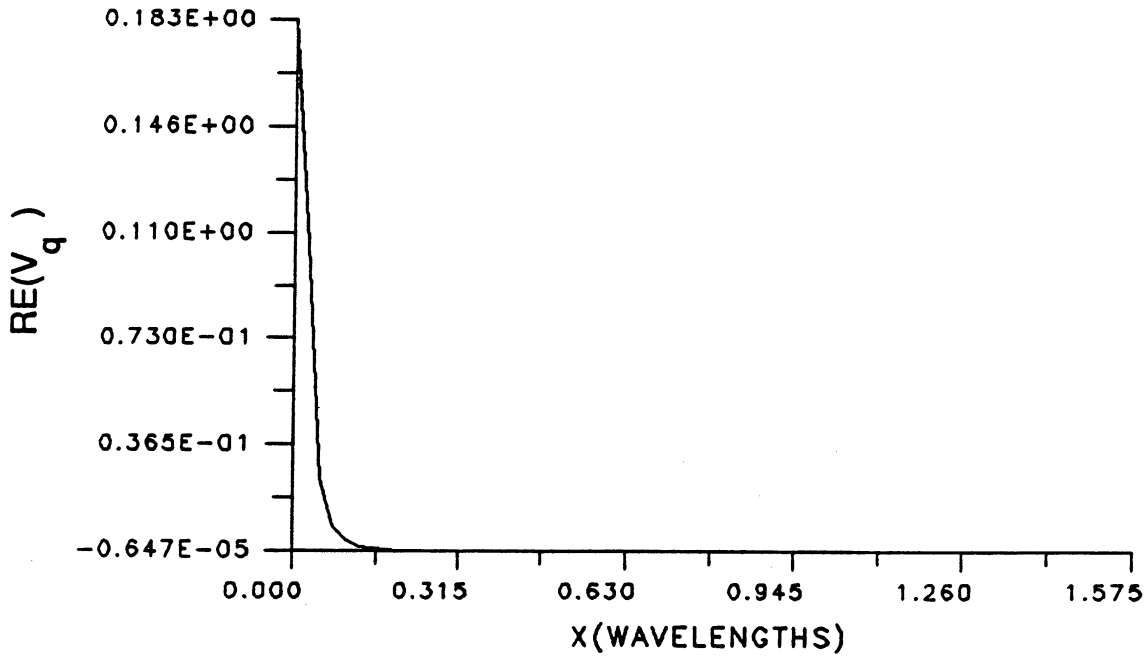

Figure 7: The amplitude distribution of the excitation vector is highest at the position of the feed ($x = 0$), then tapers off uniformly.

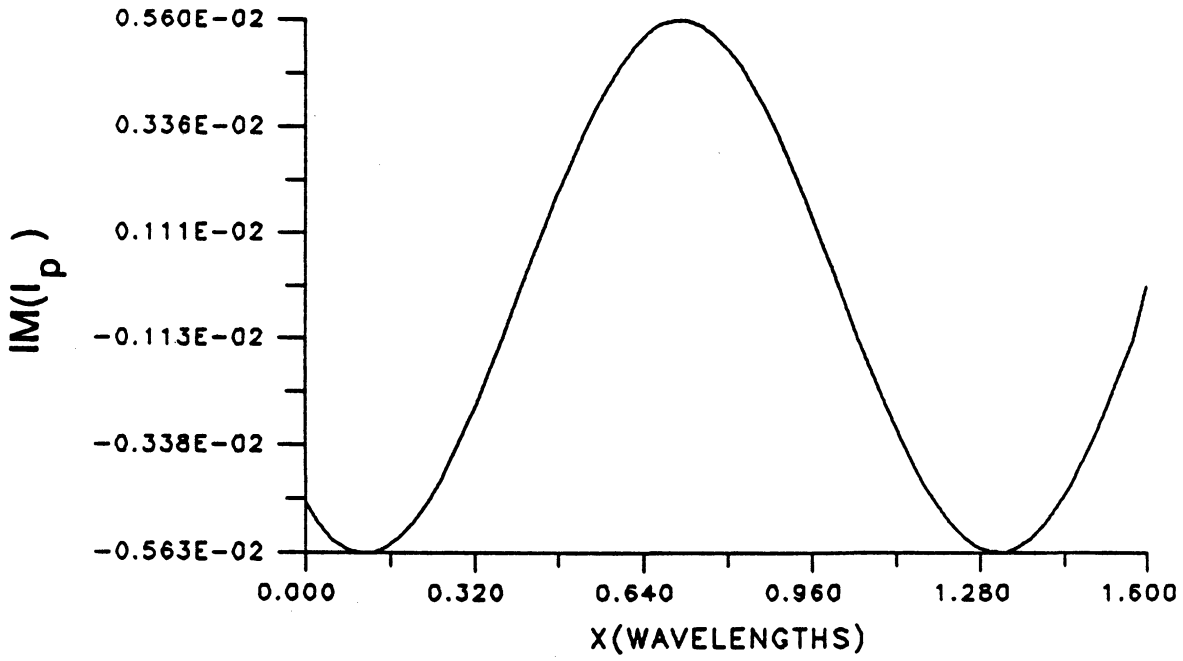

Figure 8: The imaginary part of the current distribution for an open-ended line has a sinusoidal shape, and goes to zero at the line's end ($x = 1.6\lambda_d$).

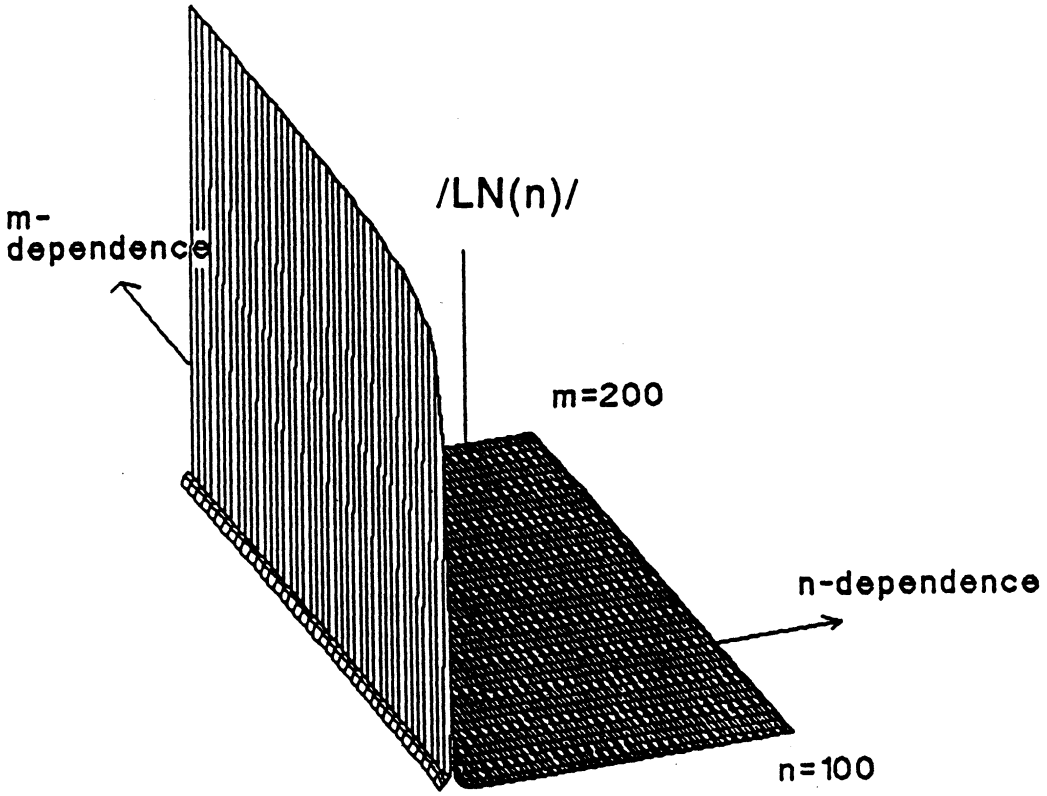

Figure 9: $LN(n)$ has convergent behavior over both m and n.

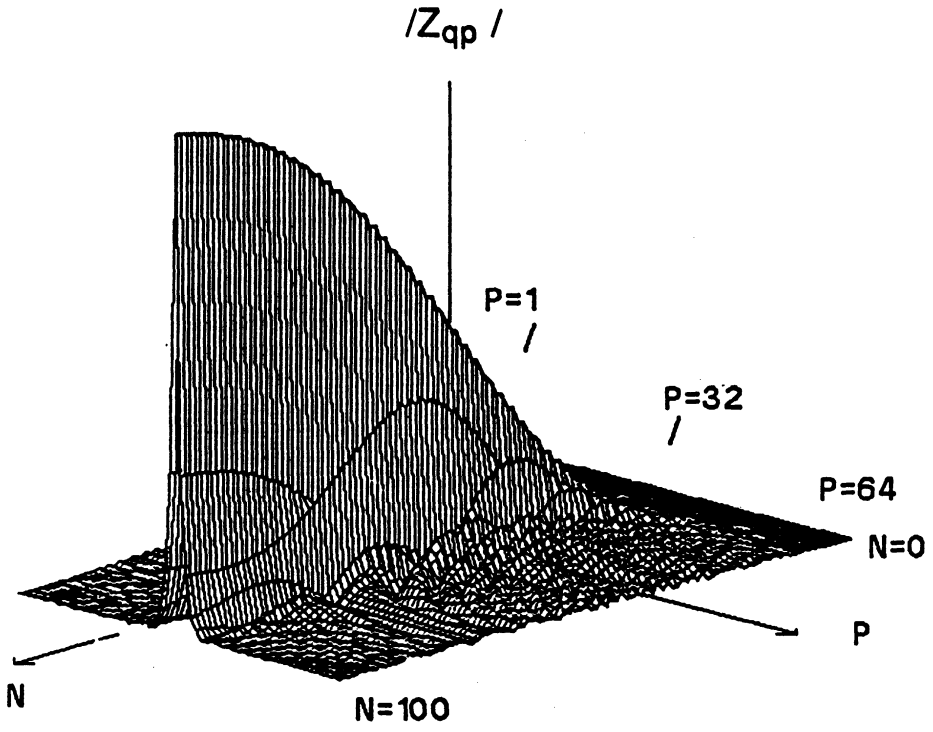

Figure 10: A row ($q = 32$) of the impedance matrix is seen to be well formed after adding 100 terms on n.

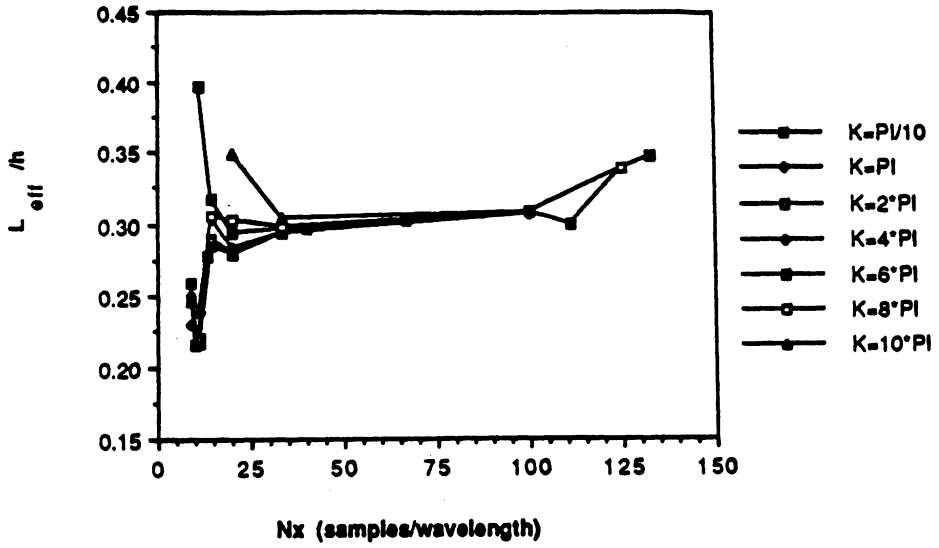

a. A plot of L_{eff} versus sampling displays a flat convergence region for all values of K considered.

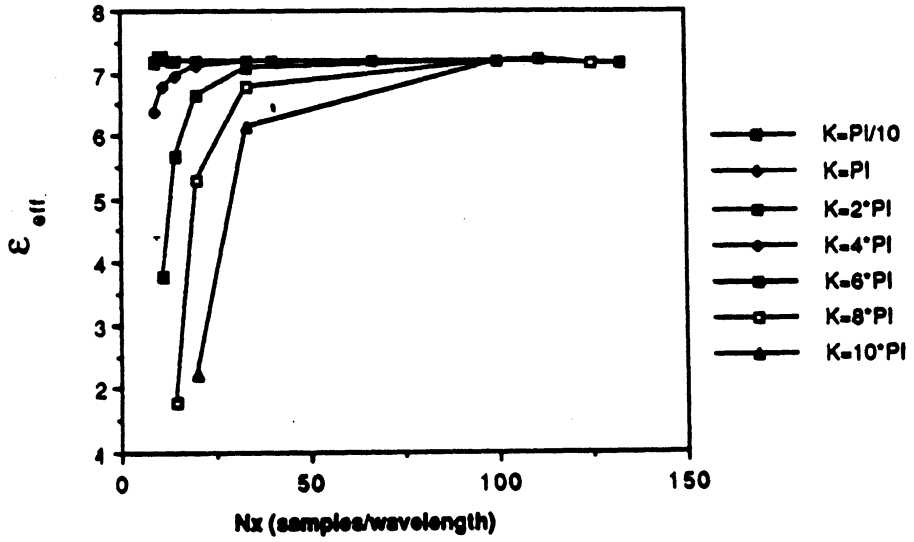

b.The convergence of ϵ_{eff} versus sampling is seen to be better for low K-values.

Figure 11: Convergence of L_{eff} and ϵ_{eff} versus sampling.

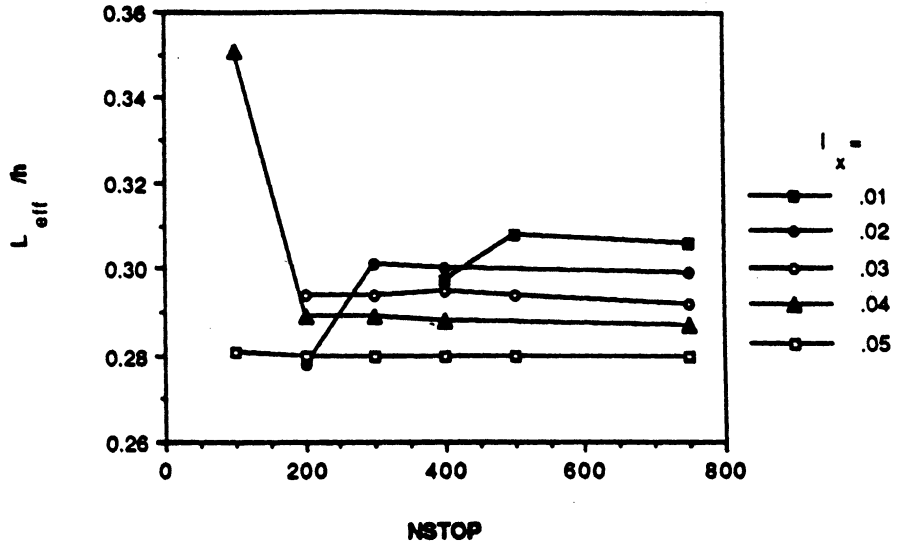

a. The convergence of L_{eff} on n depends on l_x, but is satisfied in all cases considered after 500 terms have been added.

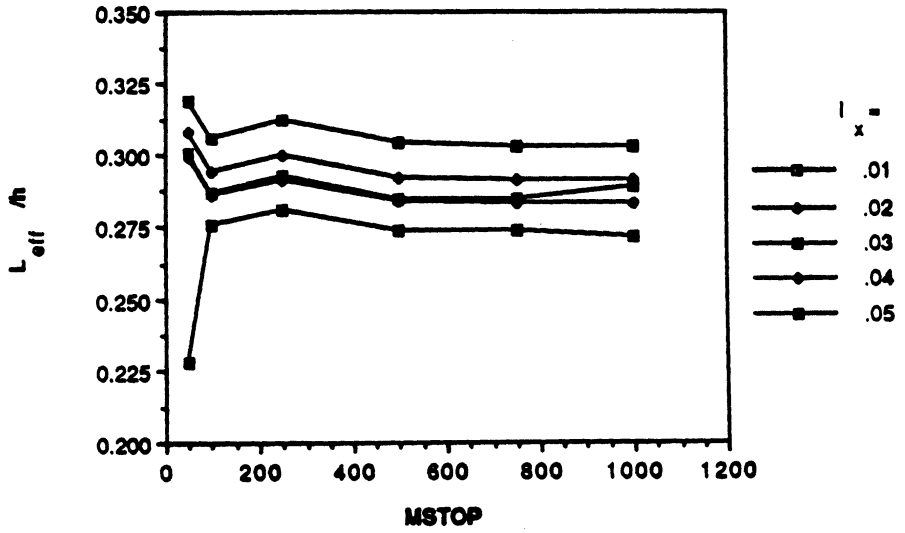

b.The convergence of L_{eff} on m is also satisfied after 500 terms.

Figure 12: Convergence of L_{eff} on n and m.

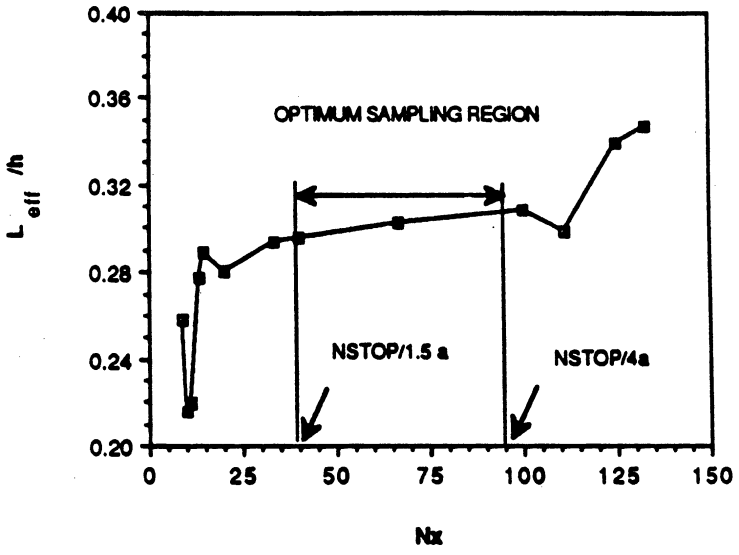

Figure 13: The optimum sampling range is seen to correspond directly with the flat convergence region for the L_{eff} computation.

I. INTRODUCTION

This is the second of two papers concerned with the study of shielding effects in microstrip discontinuities. The companion paper develops a new theoretical method for the full-wave analysis of shielded microstrip discontinuities. The effects of shielding are important in two situations. The first is when the frequency approaches or is above the cutoff frequency for higher order mode propagation. The second occurs when the metal enclosure (Figure 1) is physically close to the circuitry (proximity effects). These effects have not been adequately studied in the past, and are not accounted for in the discontinuity models in most available CAD packages.

In addition to improved theoretical methods, there is a great need for experimental data. Published experimental data on microstrip discontinuites is very limited, especially for high microwave (above X-band) and millimeter-wave frequencies. Such measurements are not trivial, but are essential for verification of the theoretical method. This need motivated the experimental study discussed here.

This paper (Part II) uses the previously described method (Part I) to study the effects of the shielding cavity on the behavior of one- and two-port discontinuities including open-ends, series gaps and parallel coupled line filters. In addition, comparisons are made to available data from other theoretical solutions including other full-wave analyses and commercially available CAD packages.

II. EXPERIMENTAL TECHNIQUES

Measured data on microstrip discontinuities is very limited, particularly at higher frequencies (above 10GHz). This is due to the difficulties involved with performing accurate microstrip measurements. In order to measure a microstrip circuit, it is generally mounted in a test fixture with either coax-to-microstrip or waveguide-to-microstrip transitions. The main difficulties associated with such measurements are the separation of test fixture parasitics from measurements, called de-embedding and the non-repeatability of microstrip connections.

This section explains the experimental techniques used for this study, and addresses the connection repeatability issues that pertain to the measurements.

A. De-embedding Approach

The measurement approach of this study employs Automatic Network Analyzer (ANA) techniques in conjunction with the thru-short-delay (TSD) method for de-embedding the effects of the test fixture from the measurements. The test fixture that was used is shown in Figure 2. The fixture employs a pair of 7mm "Eisenhart" coax-to-microstrip transitions [1]. The shielding is provided by placing U-shaped covers on top of the microstrip carriers. This forms a cavity similar to Figure 1. The instrumentation used for the measurements was an HP8510 ANA.

The test fixture invariably introduces unwanted parasitics and a reference plane shift to the measurements. These effects must be accurately accounted for and removed from the measurements, or incorporated into the ANA system error model. Conventional ANA calibration, which uses a short circuit, an open circuit, and a matched load is not easily performed in microstrip since these calibration standards

are much more difficult to realize in microstrip.

The process for removing test fixture effects is called de-embedding and consists of two steps: 1) fixture characterization, and 2) the extraction of fixture parasitics. Through de-embedding, the effective calibration reference planes are moved from the coaxial or waveguide ANA test ports to microstrip test ports within the fixture.

A comparison of various de-embedding techniques [2] lead to the choice of the TSD technique for the experimental study. This approach was selected over the alternatives considered because the standards used for fixture characterization are the easiest to realize in microstrip, and because the connections to these standards can be made in the same way as the connections made to discontinuity test circuits. In the TSD technique, two-port measurements made on a thru (zero length delay) line, a "short" circuit, and a delay line provide enough information to characterize the fixture. Since the original paper [3], it has been pointed out that the "short" implied in TSD, need not be perfect. In fact, any highly reflecting standard may be used in its place [4,5]. The only requirement is that the same reflection coefficient Γ_s must be presented to both microstrip test ports.

This measurement approach provides for the measurement of the effective dielectric constant, the reflection coefficient of open-end discontinuities, and the two-port scattering parameters of series gaps and coupled line filters. In the present implementation of TSD de-embedding, an open-ended microstrip line is used in place of the short as the reflection standard. Measurements of microstrip effective dielectric constant ϵ_{eff}, and the reflection coefficient of the open-end Γ_{op} are obtained as byproducts of the fixture characterization procedure. Once the fixture is char-

acterized, the de-embedded S-parameter measurements of two-port discontinuities are obtained by extracting the fixture parasitics mathematically.

B. Connection Repeatability Issues

One drawback to the TSD technique is that good microstrip connection repeatability is important for accuracy. Microstrip connections are much harder to make, and less repeatable than connections in coax and waveguide. This is a key limiting factor to the accuracy of microstrip measurements at higher frequencies. To address this issue, a microstrip connection repeatability study was carried out [6]. The results of this study were used to decide on the best connection approach to use and to estimate the associated measurement uncertainties.

There are three basic connection alternatives for TSD characterization of a coaxial fixture. Each of these must rely on at least one of the following assumptions:

1. repeatability of connections made from the coax-to-microstrip transition to the microstrip line
2. repeatability of microstrip-to-microstrip interconnects
3. uniformity of electrical characteristics between different transitions (launcher-to-launcher uniformity).

The results of the repeatability study favor a connection approach relying on repeatable coax/microstrip connections, and this was the approach adopted for the present work.

As part of this work, a method was developed to approximate the uncertainties in de-embedded results arising from connection repeatability errors [2]. The anal-

ysis consists of perturbing the S-parameters of the TSD standards and the D.U.T. with a set of experimentally derived error vectors that are representative of the variations of each S-parameter (S_{11}, S_{12} etc.) measurement with repeated connections. Software was written to allow processing the perturbed S-parameter data in the same way as the measurement data is processed during the TSD de-embedding procedure discussed above. This perturbation analysis, shows approximately how connection errors —which are inevitable— propagate through the TSD mathematics and limit the precision of the final results.

III. NUMERICAL AND EXPERIMENTAL RESULTS

In this section, the numerical and experimental results of the present research are presented for the network parameters of shielded microstrip discontinuities. Included here are results for the effective dielectric constant, open-end and series gap discontinuities, and coupled line filters. Where possible, comparisons are made to results generated from the commercially available CAD packages *Super Compact* and *Touchstone*[1].

The CAD models used in these packages are based on a combination of different theoretical techniques, most often embodied in simplified closed form solutions, curve fit expressions, or look-up tables. These models do not adequately account for the effects of the shielding box (Figure 1). Further, in simulating a circuit containing many discontinuities, the analysis of these packages assume that the discontinuities are independent of one another and the matrix representations for each discontinuity are simply cascaded together mathematically.

[1] *Super Compact* and *Touchstone* are microwave CAD software packages available from Compact Software and EESOF respectively.

In contrast, the full-wave solution presented in Part I accurately treats the entire geometry of the shielded microstrip circuit as a boundary value problem. The interactions between the discontinuity structure, adjacent microstrip conductors, and the shielding cavity are automatically included in the analysis. Because of this, the method is expected to provide better accuracy than CAD model predictions.

A. Cutoff Frequency and Higher Order Modes

One case where shielding effects are noticeable is when the frequency approaches the cutoff frequency f_c for the first higher order shielded microstrip mode. The nature of higher order modes in shielded microstrip is quite different from that in open microstrip. In open microstrip, higher order modes occur in the form of surface waves and radiation modes. The first surface wave mode has a cutoff frequency of zero. In shielded microstrip, the higher order modes take the form of waveguide modes [7]. As a consequence, below the waveguide cutoff frequency, only the dominant microstrip mode can exist.

For the present work, the f_c for the shielded microstrip geometry of Figure 1, is approximated by considering the dielectric-loaded waveguide formed by removing the strip conductors and the walls at $x = 0$, and a. The cutoff frequencies so derived have been found to give a good prediction of where higher order effects are first observed in the computed current distributions. As an example, Figure 3 shows the current distribution on an open-ended line operating below the cutoff frequency. For the indicated geometry, f_c is about 17.9 GHz. As the frequency is raised above the cutoff frequency, the current becomes more and more distorted as shown in Figure 4. The distortion is due to the interactions between the dominant

mode and the first higher order waveguide-like mode inside the cavity.

B. Effective Dielectric Constant

Figure 5 shows ϵ_{eff} for a 25 mil thick alumina substrate where the cross sectional shielding dimensions, b and c, are ten times the substrate thickness (h). The numerical results are compared to measurements, and to CAD package predictions. Note that *Super Compact* allows only the cover height to be varied while the calculation provided by *Touchstone* neglects shielding effects. For the shielding geometry used here, it is seen that the difference between the numerical and CAD package results are within experimental error. However, interestingly enough, better agreement between the CAD results and the numerical results is observed at higher frequencies. This may be due to the fact that the side walls, which are not included in the CAD package analysis are electrically closer to the strip at low frequencies.

The measured data is obtained as a byproduct of the TSD fixture characterization procedure as discussed above. The data shown represents the average of ten separate procedures conducted over a period of time with four different sets TSD standards. The error bars shown in Figure 5 represent the standard deviation ($\pm s$) of the different measurements. This data is shown here in lieu of the result from a single measurement, since it gives a more representative view of the involved measurement uncertainty. In this case the error bars shown represent the combined effect of connection errors, variations in ϵ_r, and other factors. The major error source in this case is believed to be the variations in ϵ_r which can be significant

Table 1: CAVITY NOTATION USED TO DENOTE DIFFERENT GEOMETRY AND SUBSTRATE PARAMETERS

CAVITY	ϵ_r	W (in)	h (in)	b (in)	c (in)	f_c (GHz)
CA	9.7	.025	.025	.250	.250	21.8
CC	9.7	.025	.025	.100	.100	37.5
CF	9.7	.025	.025	.075	.075	41.7
QCB	3.82	.0157	.010	.122	.080	45.8
QCE	3.82	.0157	.010	.100	.100	73.0
QCG	3.82	.0157	.010	.050	.05	102.5

for alumina substrates [8][2].

To see how ϵ_{eff} varies with shielding, consider the plot of Figure 6. This plot compares numerical and *Super Compact* results for three different shielding geometries. The notation used to describe different shielding and substrate geometries is explained in Table 1.

In all cases, as the shielding is brought closer to the microstrip a reduction in ϵ_{eff} is predicted. The case for cavity CA is the same as that of Figure 5. For the other two cases, where the shielding is closer to the microstrip, the *Super Compact* shows a smaller effect than the present integral equation method predicts.

The effect of shielding on ϵ_{eff} for a quartz substrate is displayed in Figure 7. In this case the *Super Compact* analysis is seen to give good results for both of the two larger shielding geometries . However, the numerical results again show a larger reduction in ϵ_{eff} as the size of the shielding is decreased further.

The reduction of the effective dielectric constant, relative to *Super Compact*,

[2]This error reflects the uncertainty of not knowing the exact value of ϵ_r to use in the theoretical simulations.

can be explained as follows. For a larger shielding geometry, the field distribution on the microstrip more closely resembles the open microstrip case, with most of the electric field concentrated in the substrate. In this case, most of the electric field lines originate on the microstrip conductors and terminate on the ground plane below. As the cavity size is reduced, the ground planes of the top and side-walls are brought closer to the microstrip lines. The electric field distribution is now less concentrated in the substrate, as more field lines can terminate on the top and side walls. As a result, a proportionally larger percentage of the energy propagating down the line does so in the air region, and the dielectric constant is reduced.

C. Open-end Discontinuity

As discussed in Part I of the paper, an open-end discontinuity can be represented by an effective length extension L_{eff}, or by a shunt capacitance c_{op}. Both of these three representations will be used in this section.

The plot of Figure 8 compares L_{eff} results to those of Jansen et al. [9] and Itoh [10]. In this case, the dimensions of the shielding cavity are large with respect to the substrate thickness. The results from this research are almost identical to those obtained by Jansen et al. for frequencies above 8 GHz, but show a reduced value for lower frequencies.

The case of Figure 8 was chosen to compare the coaxial and gap generator excitation methods used in the method of moments solution Table 2 shows that the results computed for this case by the two methods are equivalent. This equivalence also holds for the two-port scattering parameters for the structures considered herein. Hence, as far as computing network parameters is concerned either

Table 2: COMPARISON OF L_{eff}/h COMPUTATION FOR THE TWO TYPES OF EXCITATION METHODS

f (GHz)	4	8	12	14	16	18	20
GAP GENERATOR	.298	.305	.309	.321	.324	.344	.353
COAXIAL EXCITATION	.299	.304	.309	.322	.327	.344	.352

method gives good results. Since the coaxial method is more realistically based, this conclusion lends validity to the use of the gap generator method.

The results shown in Figure 9 illustrate the effect of shielding on the open-end discontinuity. The normalized open-end capacitance c_{op} is plotted for three different cavity sizes. The results show that reducing the cavity size raises f_c (as expected), and it lowers the value of c_{op}. For comparison, data obtained from *Super Compact* and *Touchstone* and measurements (see Section 4.3) are included. The errors bars on the measurements represent the estimated standard deviation ($\pm s$) of the connection errors associated with this measurement[3].

Similar shielding effects are observed for an open-end on a quartz substrate as shown in Figure 10. In this case it is seen that the *Super Compact* result gives a good value for low frequencies, and where the frequency is well below the cutoff frequency for a given shielding size. These results show that shielding effects due to wall proximity are less important than shielding effects due to the onset of higher order modes.

[3]The other error sources indicated for the effective dielectric constant measurement are not considered to be as significant for this measurement.

D. Series Gap Discontinuities

Numerical and experimental results have been obtained for series gap discontinuities of three different gap widths [2]. Results for one of these gaps are presented here.

Numerical results for the magnitude of S_{21} of a series gaps with a 15mil gap width are shown plotted in Figure 11. For comparison, results obtained using *Super Compact*, and *Touchstone* are also shown plotted along with measured data. The numerical results are seen to be in very good agreement with the measurements. The test substrate and shielding dimensions used for the measurements are those for cavity CA (Table 1). The error bars associated with the connection errors, are on the order of $\pm$.5dB and are too small to show on the plots.

Results for the angle of S_{21} and S_{11} for the 15 mil series gap are shown in Figures 12 and 13. The error bars in these charts represent the estimated standard deviation from the perturbation analysis[4]. Although the measurements tend to favor the numerical results, the phase differences are not too significant since it is suspected that the measurement may be in error by more than that attributed to connection errors alone. The phase of the S-parameters for the other two gaps behave in a similar way as that for the 15 mil gap and have been omitted from this treatment.

These results are seen to further verify that the theory developed in Part I. For the large shielding dimensions used for the measurements ($b, c \gg h$) the CAD models are also seen to give reasonable predictions. The behavior of series gaps

[4]The analysis was carried out at 10GHz, and it is assumed that the connection errors are approximately the same at the other measurement frequencies.

for different shielding dimensions was not studied, instead emphasis was placed on obtaining results for coupled line filters since their behavior is more complicated and therefore more interesting.

E. Four Resonator Coupled Line Filter

The last results to be presented are for the four resonator coupled line filter of Figure 14. For brevity, only the amplitude and phase of S_{21} will be discussed.

Numerical and measured results of this research are compared along with CAD model predictions in Figure 15. The CAD package analysis for coupled line filters is performed by cascading two different types of discontinuity elements together: coupled microstrip lines, and open-end discontinuities. Neither of the packages studied here account for shielding in the open-end discontinuity model, however, *Super Compact* does include the effect of the cover height in the model for coupled lines.

The numerical results shown in Figure 15 demonstrate excellent agreement with measurements up to the cutoff frequency. The cutoff frequency f_c for the shielding geometry of the filter is approximately 13.9GHz. Above this frequency, the measurements are distorted due to waveguide moding within the test fixture.

The results of Figure 15 show that even for large shielding dimensions the discrepancies are apparent in the CAD model predictions, whereas the numerical results follow the measurements closely, both in amplitude and phase. As can be seen from the amplitude response (Figure 15a), the CAD models give a good prediction in the pass band, but fail to predict the filter response in the rejection band. This is also seen from the phase response (Figure 15b), where the CAD

models display a large error compared to measurements, between about 6 and 8.5GHz, while the numerical results track the measured amplitude and phase very well.

Below about 5.5GHz, the measured phase is seen to be different from the predictions of both the CAD models and the numerical results. This is most likely due to a phase error in the measurements. In the TSD technique, the delay line for the measurements should ideally be $\frac{\lambda_g}{4}$ at the measurement frequency [5]. When the electrical length becomes either too short or too close to a multiple of $\frac{\lambda_g}{2}$ phase ambiguities can result. A good rule of thumb is for the delay line to be between $\frac{\lambda_g}{8}$ and $\frac{3\lambda_g}{8}$. At 5.5GHz the delay line used for the measurements is slightly less than $\frac{\lambda_g}{8}$; hence, this is most likely the source of the phase error in the measurements below this frequency.

We will now examine what happens as the top cover is brought closer to the circuitry. Figure 16a shows *Super Compact* predictions for the four resonator filter with two different cover heights. These predictions indicate that lowering the cover height should significantly narrow the pass band, and reduce the amplitude in the rejection band.

A significantly different prediction is observed in the numerical results for this case presented in Figure 16b. A narrowing of the pass band response is also observed in the numerical predictions, but not by nearly as much as in the *Super Compact* predicts. More importantly, the amplitude in the rejection band is seen to increase instead of decrease.

[5] Multiple lines are needed for broadband measurements.

To prove that the numerical prediction is indeed the correct one, an additional measurement was made of the filter for the low cover height case. As can be seen from Figure 16b the agreement between measured data and the numerical predictions from this research is excellent.

IV. SUMMARY AND CONCLUSIONS

In this paper theoretical and experimental results were presented for the network parameters of one- and two-port discontinuities. For the measurements, the TSD de-embedding approach was used. Connection repeatability errors were considered in detail and a perturbation analysis was developed to approximate their effect on the precision of the final de-embedded results.

The effects of shielding on microstrip behavior was studied. It has been demonstrated that the computed current distribution becomes distorted above the cutoff frequency $f_c$for the first higher order shielded microstrip mode. On the other hand, as long as the cavity size is such that the frequency is below f_c, the current is uniform and undistorted regardless of how thick the substrate is.

Only one of the CAD packages studied takes shielding into account for the effective dielectric constant (ϵ_{eff}) calculation, and then only cover effects are considered. A comparison of the CAD package predictions with the numerical results of this research for ϵ_{eff} showed that good agreement is obtained when the shielding dimensions are large with respect to the substrate thickness, while for small shielding dimensions, the difference between the different results becomes significant.

For the open-end discontinuity, good agreement with other full-wave solutions and with measurements has been demonstrated. A comparison of open-end capac-

itance for different cavity sizes showed that, as the cutoff frequency is approached, the capacitance increases in each case. Choosing a small cavity with a high cut-off frequency extends the region where the capacitance is relatively constant.

Good agreement between numerical and measured results was also demonstrated for series gap discontinuities and a four resonator coupled line filter. For the filter, reducing the cover height was seen to narrow the pass band response and raise the amplitude of the filter's rejection band response. The numerical results of this research give an excellent prediction of this effect, whereas discrepancies are apparent in the CAD model predictions.

ACKNOWLEDGEMENTS

The authors thank Mr. Ed Watkins, Mr. Jim Schellenberg, and Mr. Marcel Tutt for their contributions to this work. This work was primarily sponsored by The National Science Foundation (Contract. No. ECS -8602530). Partial sponsorship was also provided by the Army Research Office (Contract No. DAAL03-87-K-0088) and the Microwave Products Division of Hughes Aircraft Co.

References

[1] R.L. Eisenhart,"A Better Microstrip Connector", *1978 IEEE MTT-S Digest*, pp. 318-320.

[2] L.P. Dunleavy, "Discontinuity Characterization in Shielded Microstrip: A Theoretical and Experimental Study", Ph.D. dissertation, University of Michi-

gan, April 1988.

[3] N. R. Franzen and R. A. Speciale, "A New Procedure for System Calibration and Error Removal in Automated S-Parameter Measurements", *5th European Microwave Conference*,1975, pp. 69-73.

[4] B. Bianco et. al. "Launcher and Microstrip Characterization" *IEEE Trans. on Instrum. and Meas.* Vol. IM 25, NO. 4, Dec. 1976, pp. 320-323.

[5] G. Engen and C. Hoer, "Thru-Reflect-Line: An improved Technique for Calibrating the Six-Port Automatic Network Analyzer". *IEEE Trans. Microwave Theory Tech.* vol. MTT-27, No. 12, Dec. 1979, pp 987-993.

[6] L. Dunleavy and P. Katehi, "Repeatability Issues for De-embedding Microstrip Discontinuity S-parameter Measurements By the TSD Technique" *Automatic RF Techniques Group (ARFTG) Conf. Dig.* June 1986.

[7] E. Yamashita and K. Atsuki, "Analysis of Microstrip-Like Transmission Lines by Nonuniform Discretization of Integral Equations," *IEEE Trans. Microwave Theory Tech.*, vol. MTT-24, pp. 195-200.

[8] J. Snook, "Substrates for Hybrid Microelectronic Applications", *Microwave System News and Comm. Tech.*, February 1988, pp26-31.

[9] R.H. Jansen, and N.H.L. Koster, "Accurate Results on the End Effect of Single and Coupled Lines for Use in Microwave Circuit Design " *A.E.U.* vol. 34, pp 453-459, 1980.

[10] T. Itoh,"Analysis of Microstrip Resonators", *IEEE Trans. Microwave Theory Tech.*, vol MTT-22, pp 946-951, 1974.

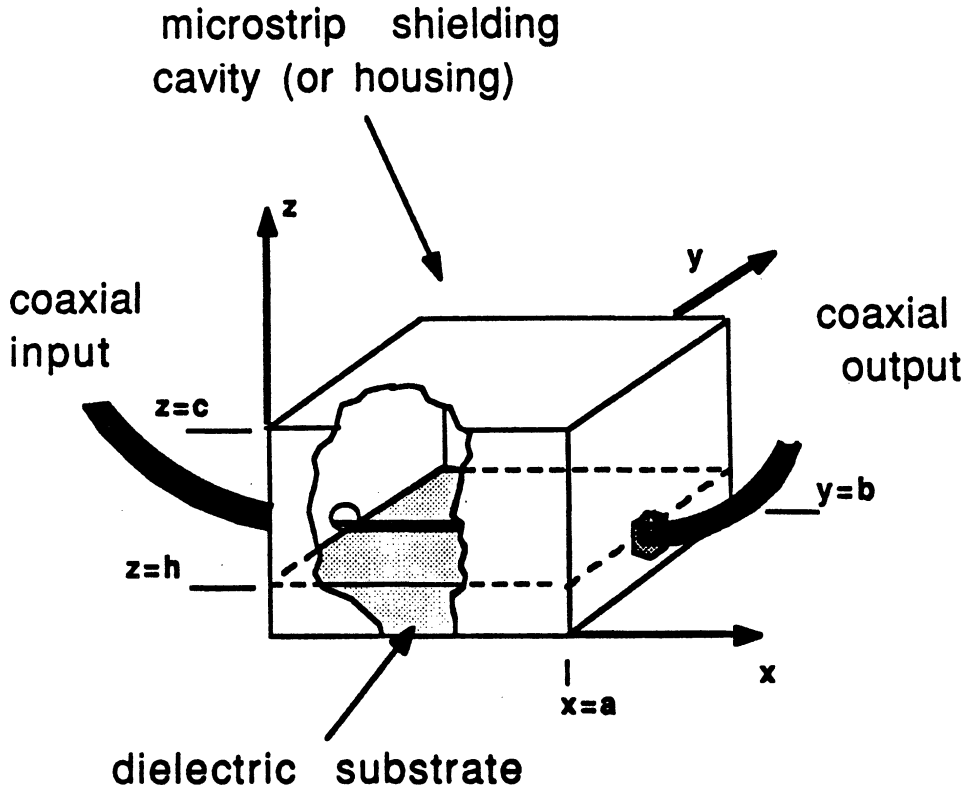

Figure 1: Basic geometry for the shielded microstrip cavity problem.

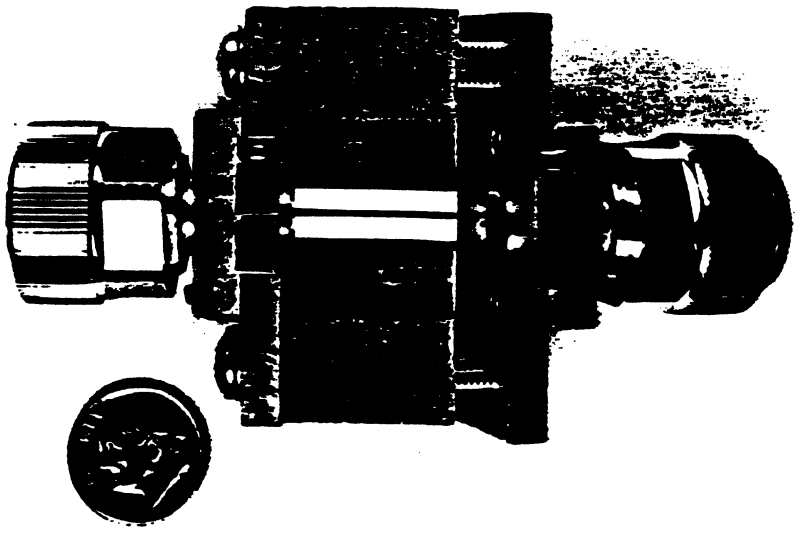

Figure 2: 7mm coaxial/microstrip test fixture (partially disassembled) used for measurements.

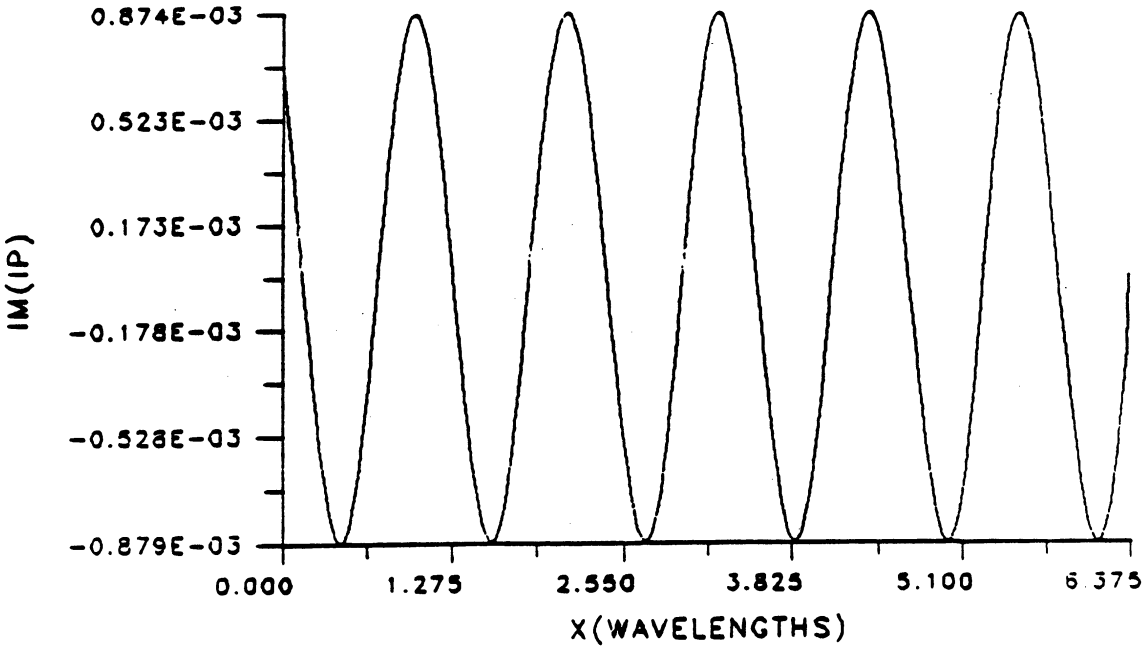

Figure 3: Below the cutoff frequency f_c, the microstrip current on an open-ended line forms a uniform standing wave pattern ($f = 16\text{GHz}, \epsilon_r = 9.7, W/h = 1.57, h = .025", b = c = .275"$).

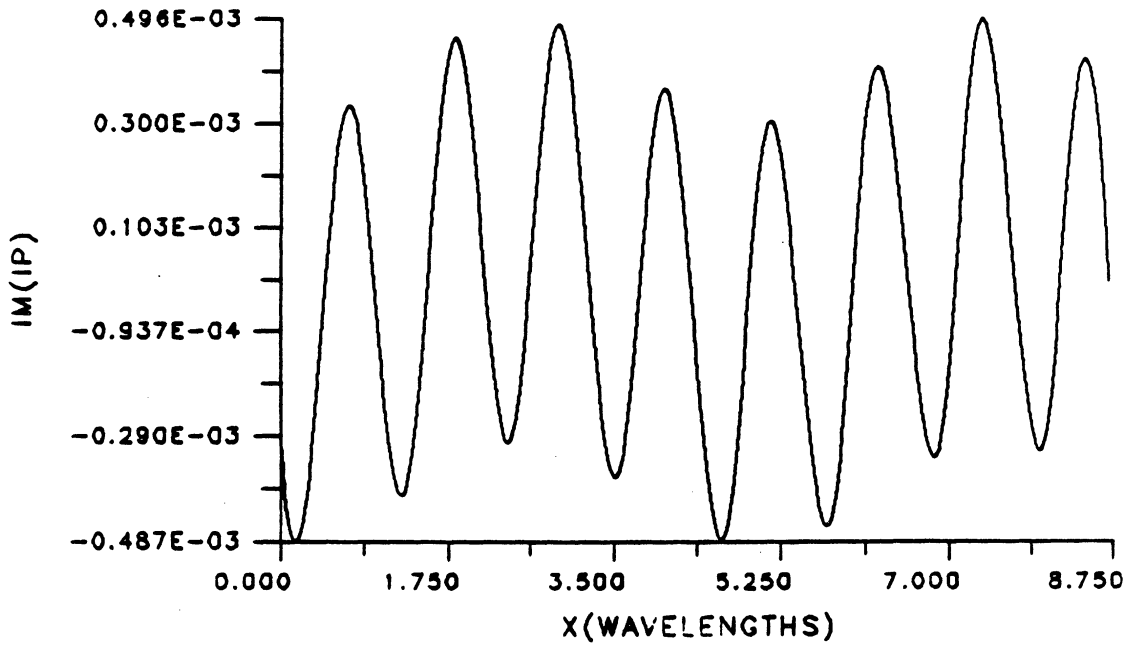

Figure 4: As the frequency is increased above f_c, the current becomes more and more distorted due to higher order modes in the current distribution (f = 22GHz,ϵ_r = 9.7,W/h = 1.57,h = .025", $b = c$ = .275").

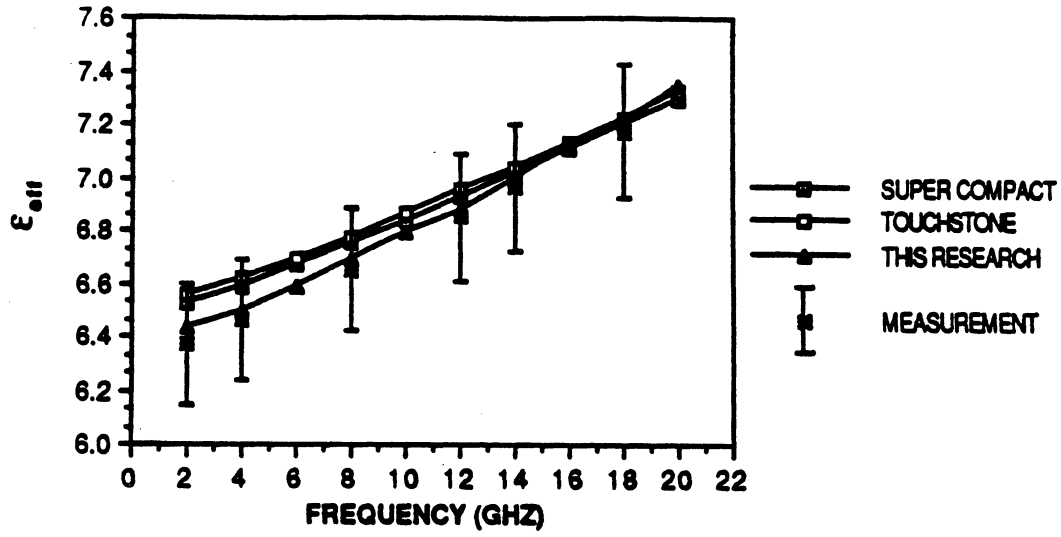

Figure 5: The numerical results for ϵ_{eff} show good agreement with both measurements and CAD package results for an alumina substrate with large shielding dimensions ($\epsilon_r = 9.7, h = .025'', b = c = .25''$).

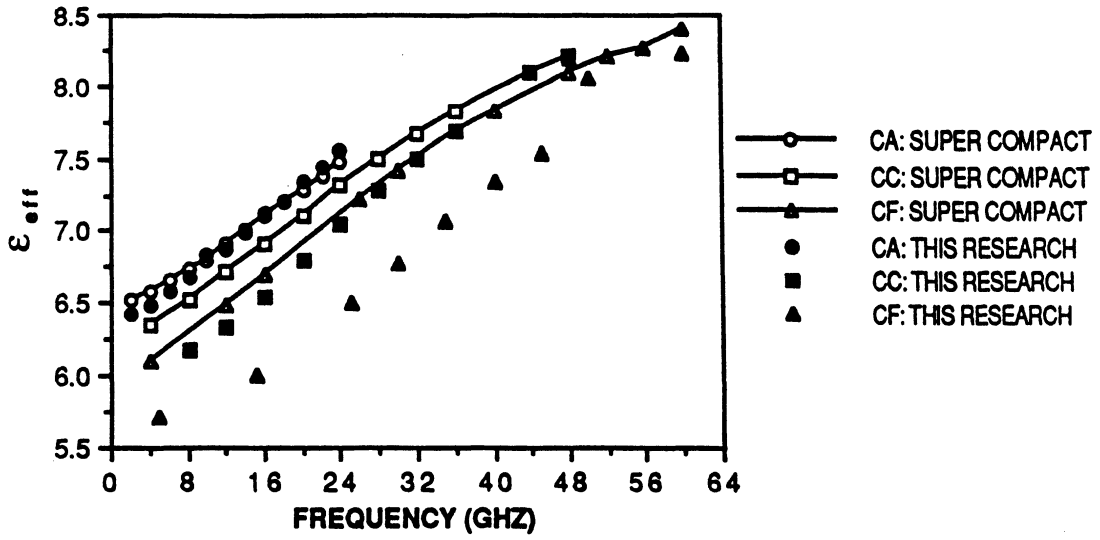

Figure 6: The effects of shielding on ϵ_{eff} are apparent as the size of the shielding cavity is reduced (see Table 5.1 for geometry.)

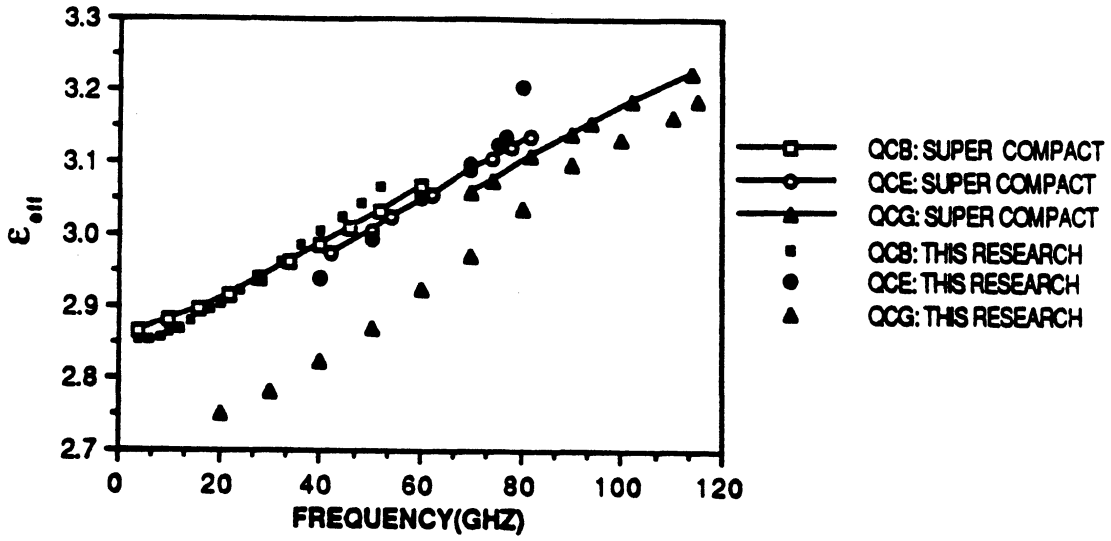

Figure 7: Shielding effects are also significant for the quartz substrate shown here (see Table 5.1 for geometry).

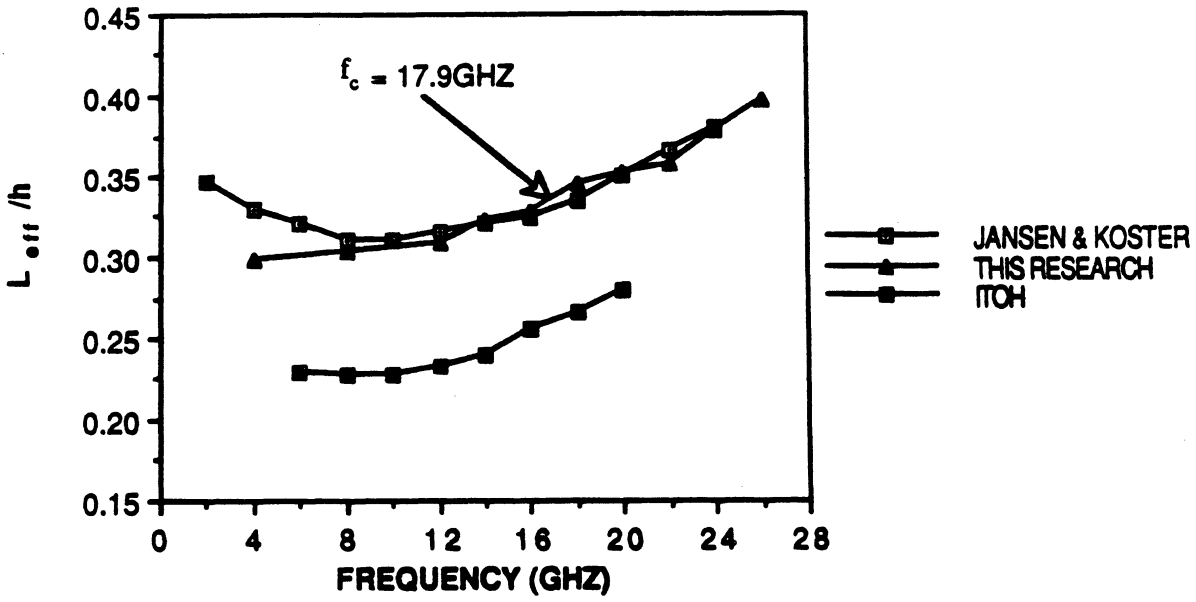

Figure 8: The numerical results of this research are also seen to compare well with other full-wave analyses ($\epsilon_r = 9.6$, W/h = 1.57, $b = .305''$, $c = .2''$, $h = .025''$).

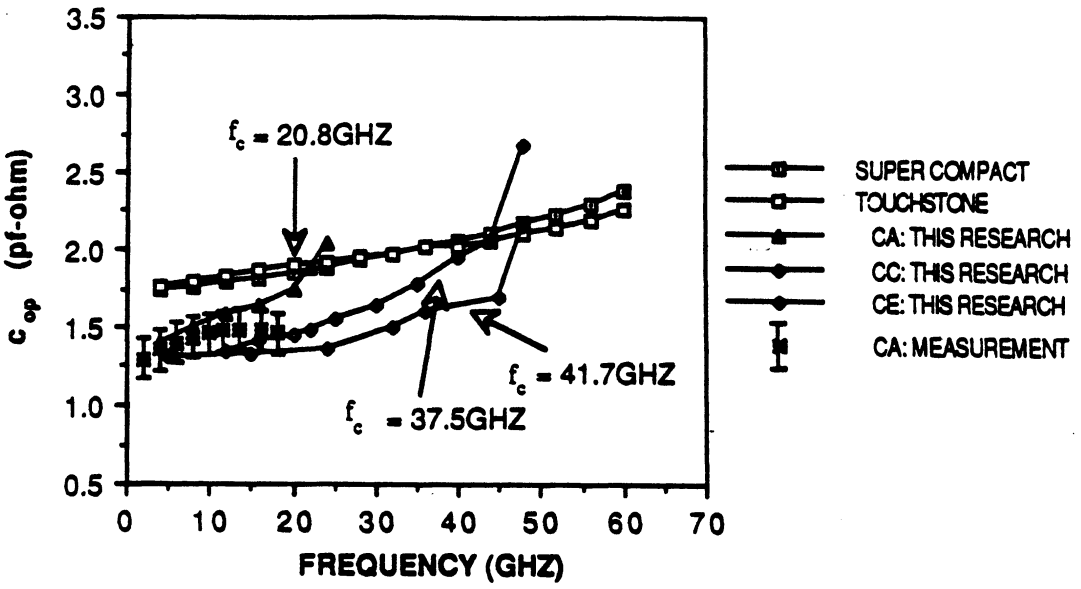

Figure 9: A comparison of the normalized open-end capacitance for three different cavity sizes shows that shielding effects are dominated by the onset of higher order modes rather than by proximity effects (see Table 5.1 for cavity geometries).

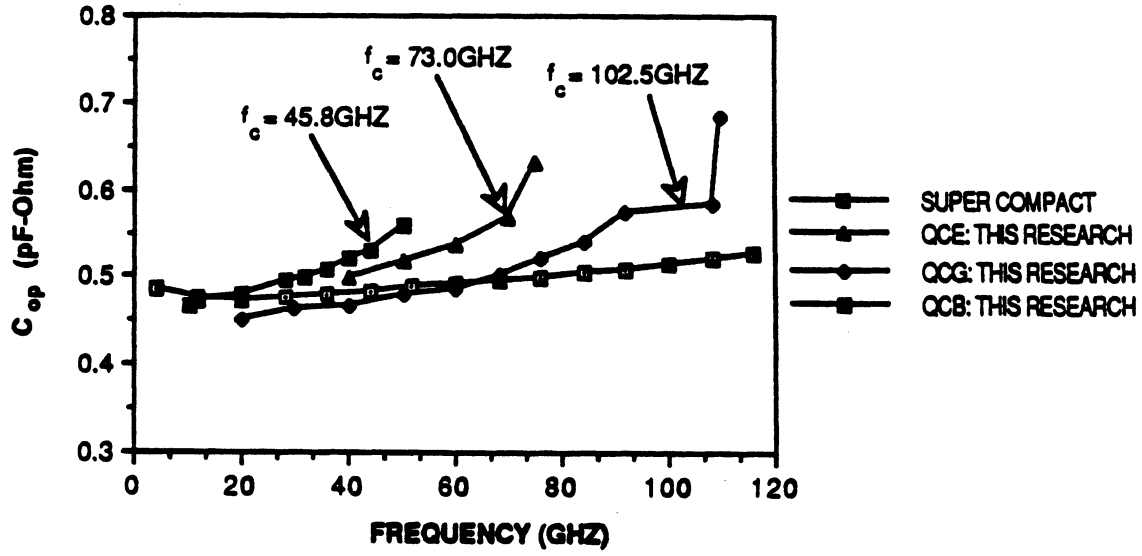

Figure 10: Nomalized open-end capacitance for three different cavity sizes for a quartz substrate also shows a strong dependence on f_c (see Table 5.1 for cavity geometries).

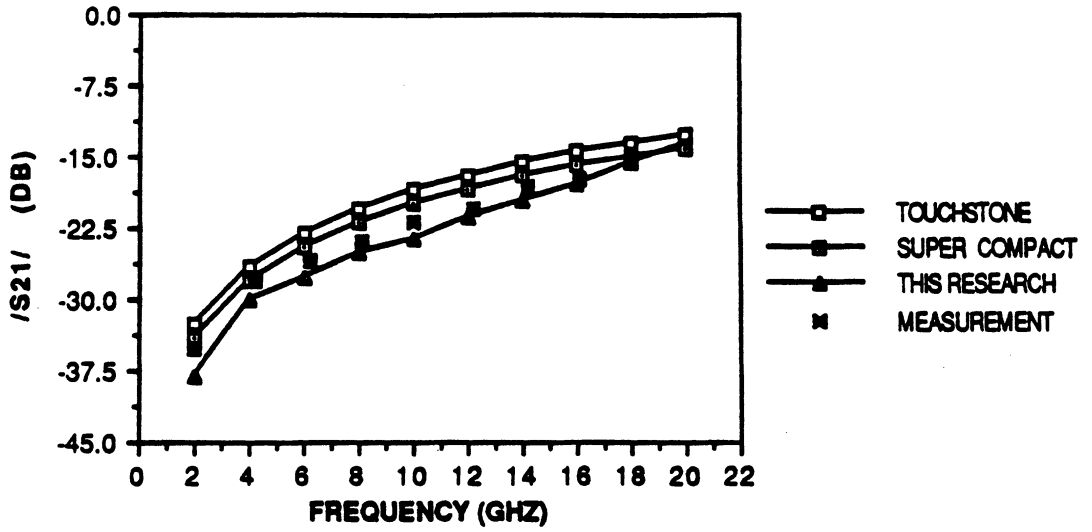

Figure 11: The numerical results show good agreement with measurements for the magnitude of S_{21} for a 15mil series gap.

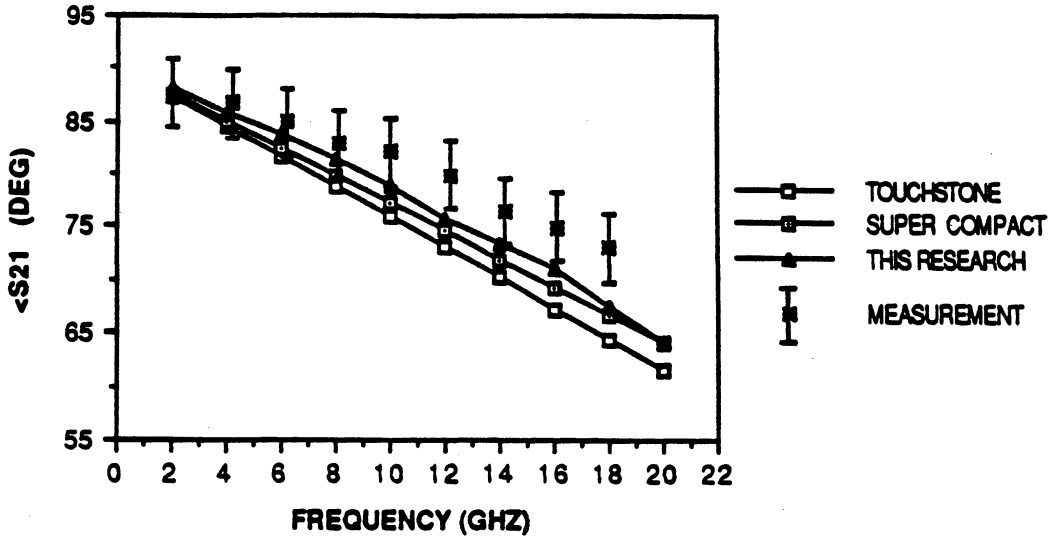

Figure 12: Angle of S_{21} for series gap.

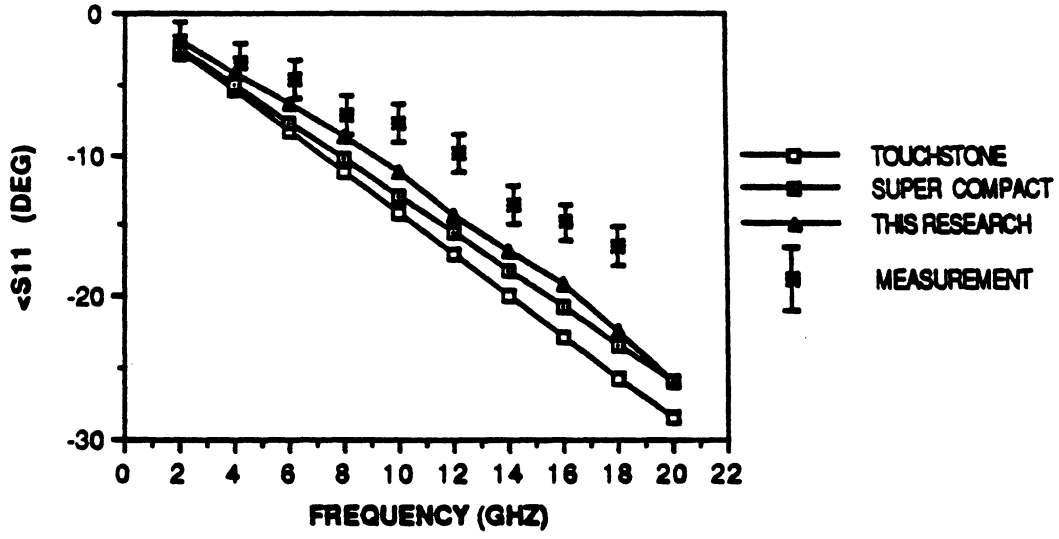

Figure 13: Angle of S_{11} for series gap.

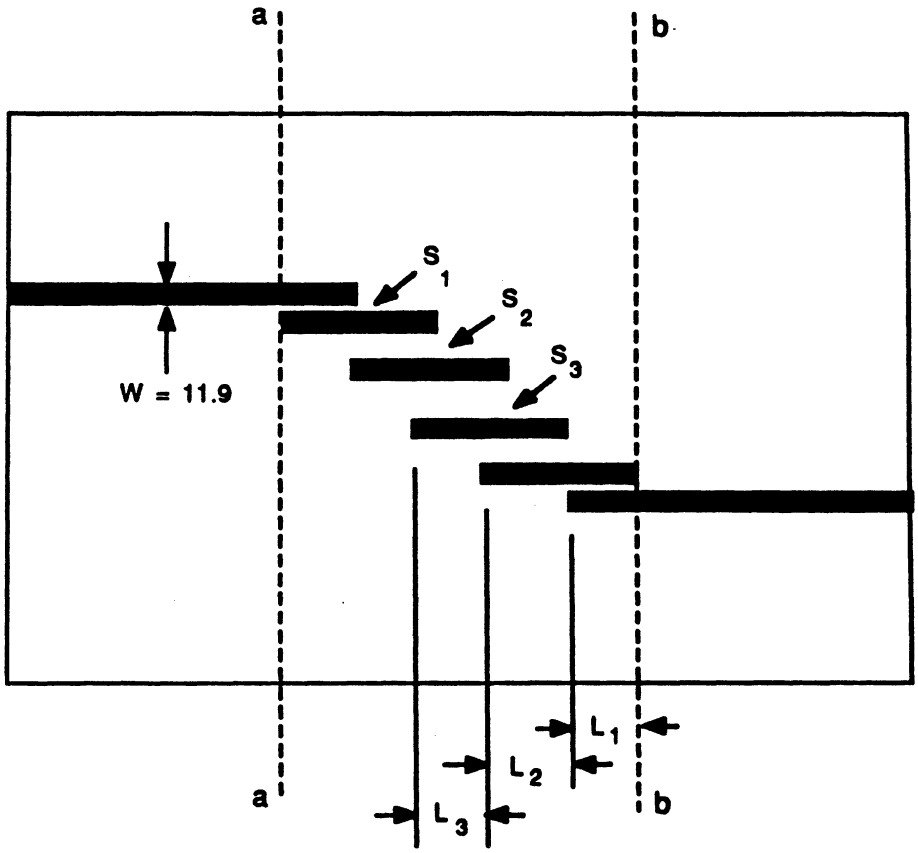

Figure 14: Sketch of four resonator coupled line filter studied here ($\epsilon_r = 9.7$, h = .025″, b = .4″, c = .25″).

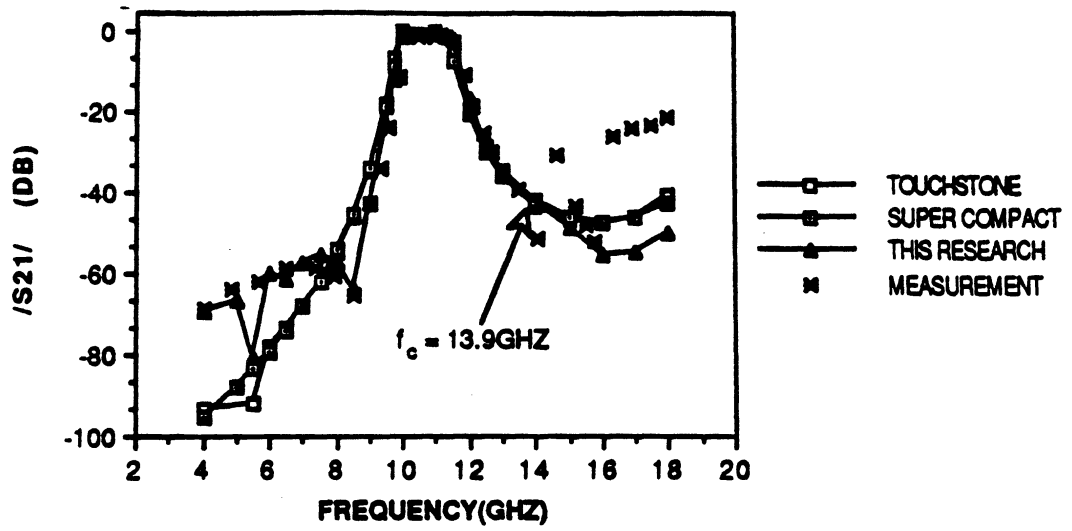

a. Amplitude of S_{21}

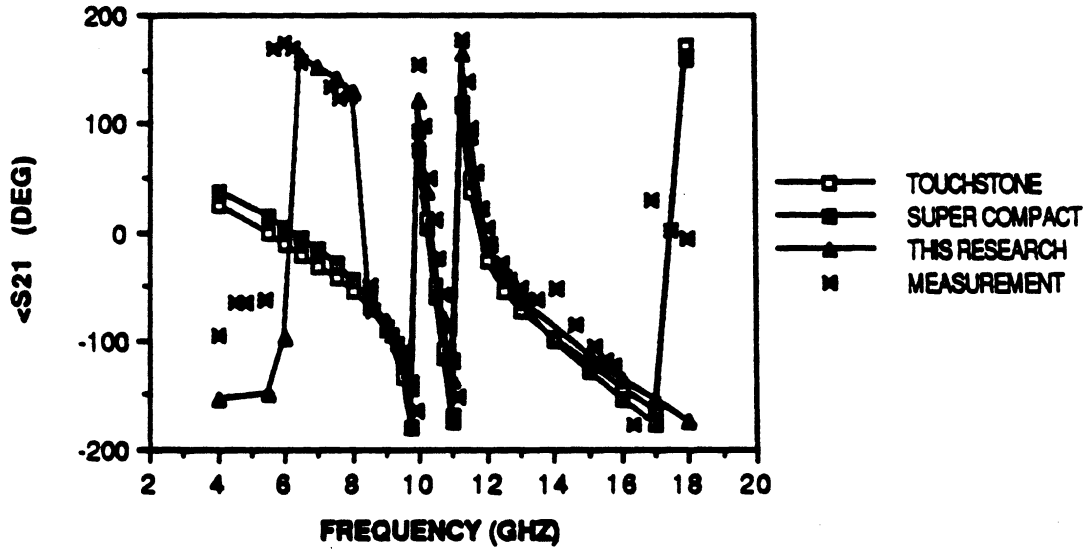

b. Phase of S_{21}

Figure 15: **Results for transmission coefficient** S_{21} of four resonator filter ($\epsilon_r = 9.7, W = .012'', h = .025''; b = .4'', c = .25''$).

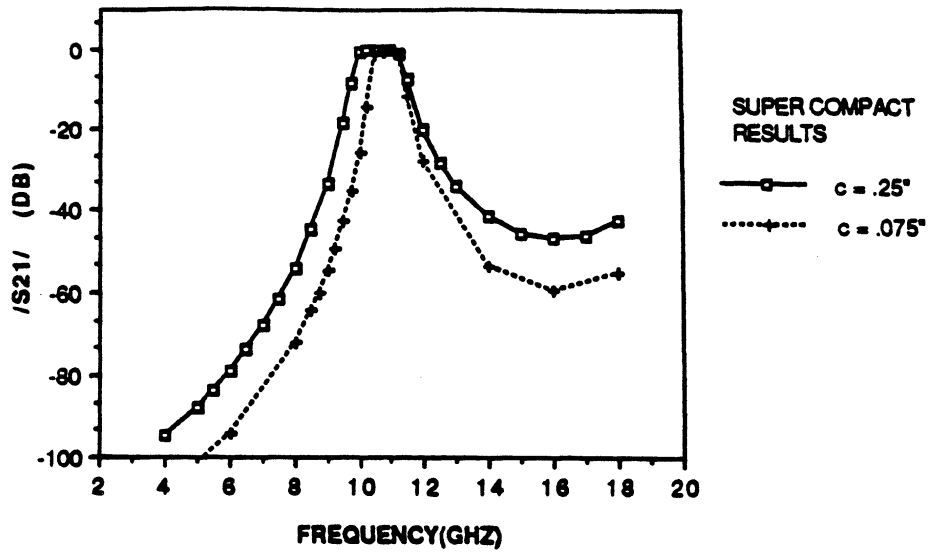

a. Super Compact predictions

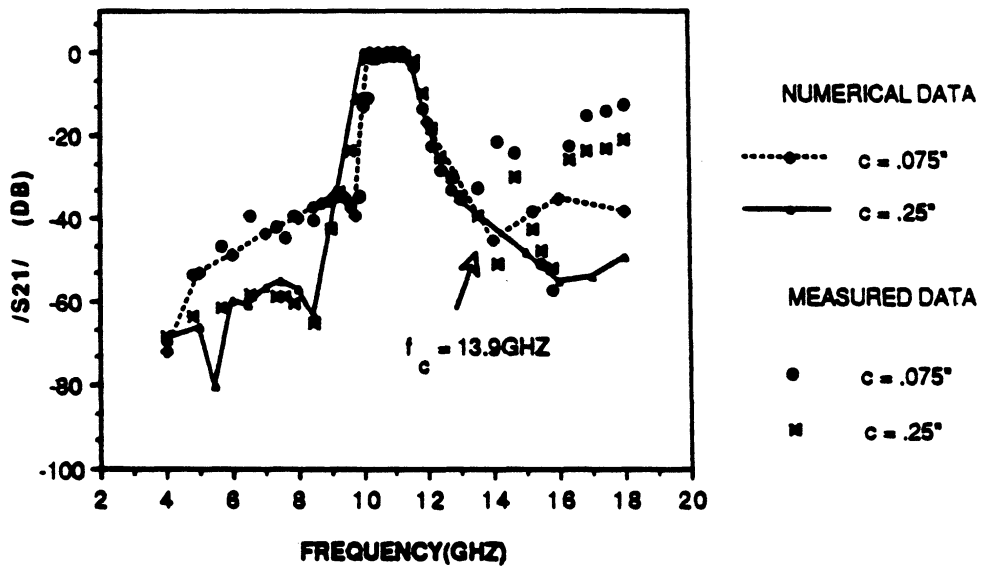

b. Numerical results of this research compared to measurements

Figure 16: Results for lowering the shielding cover on the amplitude response of four resonator filter ($\epsilon_r = 9.7, W = .012'', h = .025"; b = .4''$).

Appendix D

"High Frequency Conductor Losses in Shielded Microstrip"
T.E. van Deventer and P.B. Katehi

HIGH FREQUENCY CONDUCTOR LOSSES IN SHIELDED MICROSTRIP

T.E. van Deventer
P.B. Katehi
Radiation Laboratory
Department of Electrical Engineering
and Computer Science
The University of Michigan
Ann Arbor, MI 48109

June, 1988

1 Introduction

The effect of conductor losses in microstrip circuits and especially MMIC's is important to the circuit designer who has to account for dissipation and power loss. Several studies have been performed to calculate the dispersion in microstrip structures at microwave frequencies accounting for dielectric and conductor losses. Conductor losses have first been analyzed by Pucel [1] and Wheeler [2] where a technique based on the incremental inductance rule was used. Other approaches to the problem include quasi-TEM models [3], [4] and the conventional perturbation technique as in [5] using a spectral-domain approach.

In the present study, a shielded planar microstrip transmission line is considered where both dielectric losses in the substrate and conductor losses in the strip are accounted for. A spectral approach is adopted to solve an equivalent problem where the dielectric layer (or layers) is replaced by an impedance boundary condition. Using Fourier transformation, the Green's function of the problem is derived. Assuming a thin-strip approximation and a Maxwellian distribution for the current, a method is applied that represents conductor losses in microstrip lines in terms of a frequency-dependent impedance. The propagation constant of the lossy line is then computed for different frequencies and loss tangents.

2 Derivation of the Green's function

2.1 Geometry

Consider an infinitely long inhomogeneously-filled waveguide, with a microstrip centered on the substrate as shown in Figure 1. The dielectric substrate is considered lossy with relative permittivity ϵ_r and permeability μ_r. Conductor losses are accounted for in the microstrip whereas the walls are assumed perfect conductors.

Striplines which are within a shielding structure that is completely filled with dielectric material can propagate TEM waves. Shielded microstrip lines, however, cannot support these modes because the boundary conditions at the interface between air and dielectric cannot be rigourously fulfilled. These lines propagate hybrid modes which have non-zero cut-off frequencies with the exception of the dominant mode. Each microstrip mode propagates rectilinearly along the z-direction. Therefore the z-dependence in an infinite line will be of the form $e^{-\gamma_z z}$ where γ_z is the complex propagation constant for the given mode.

The solution for the microstrip modes can be obtained through an A_z, F_z or $\bar{A}$, $\bar{F}$ formulation which has to be applied to each of n dielectric regions separately [6]. This approach leads to a linear set of 4(n+1) equations which has to be solved analytically in order to find the unknown potentials. In the present formulation we eliminated this limitation by considering an equivalent boundary condition on the air-dielectric interface. In this manner, we are able to decrease the complexity of the solution and solve for the electromagnetic fields in the air region only. The impedance boundary condition is applied separately for LSE and LSM modes. The current source is raised above the substrate interface to study the slightly more

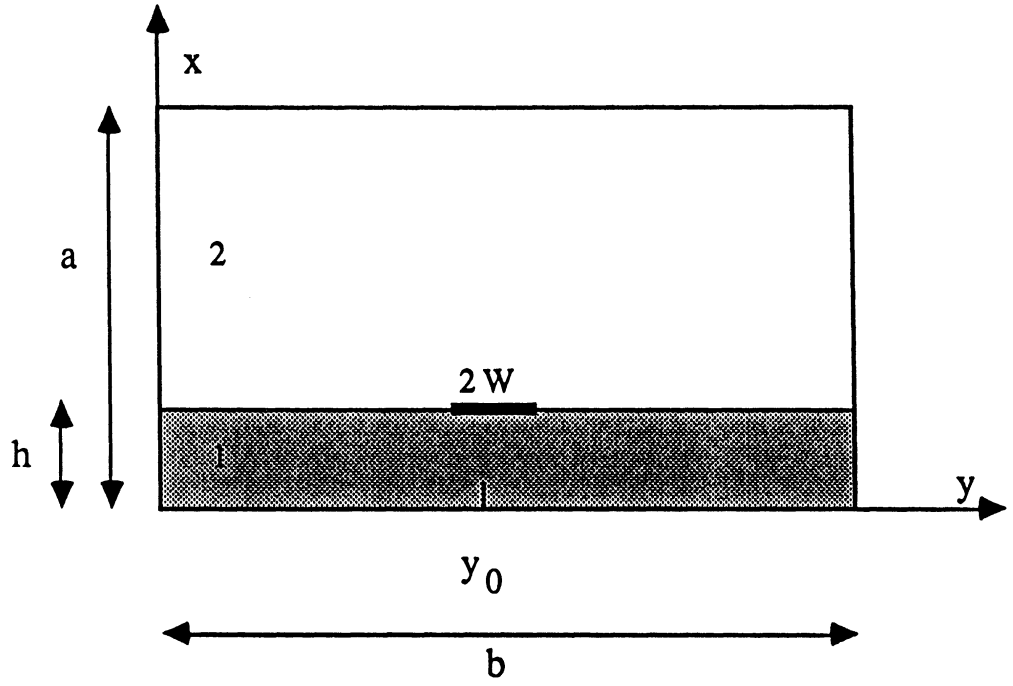

Figure 1: Cross-section of the shielded microstrip line

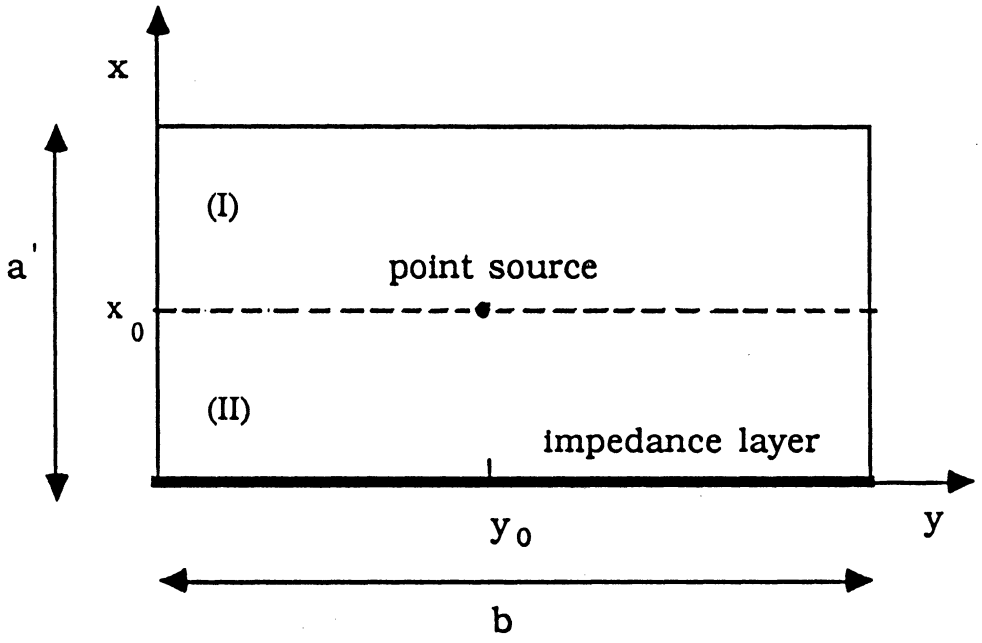

Figure 2: Cross-section of the equivalent boundary problem

general type of configuration as shown in Figure 2. Note that the height of the waveguide is now a', where $a' = a - h$.

2.2 Derivation

The Maxwell's equations are applied as

$$\bar{\nabla} \times \bar{E} = -j\omega\mu\bar{H} \tag{1}$$

$$\bar{\nabla} \times \bar{H} = \bar{J} + j\omega\epsilon\bar{E} \tag{2}$$

$$\bar{\nabla} \cdot (\epsilon\bar{E}) = \rho \tag{3}$$

$$\bar{\nabla} \cdot (\mu\bar{D}) = 0. \tag{4}$$

Defining the electric and magnetic potentials in the usual way using the Lorentz condition, we get for LSE modes

$$\bar{F} = F_x \hat{x} \tag{5}$$

$$\bar{E} = \frac{1}{\epsilon}\bar{\nabla} \times \bar{F} \tag{6}$$

$$\bar{H} = j\omega\bar{F} - \frac{1}{j\omega\epsilon\mu}\bar{\nabla}\bar{\nabla} \cdot \bar{F}, \tag{7}$$

and for LSM modes,

$$\bar{A} = A_x \hat{x} \tag{8}$$

$$\bar{H} = \frac{1}{\mu}\bar{\nabla} \times \bar{A} \tag{9}$$

$$\bar{E} = -j\omega\bar{A} + \frac{1}{j\omega\epsilon\mu}\bar{\nabla}\bar{\nabla} \cdot \bar{A}. \tag{10}$$

The problem is Fourier transformed using a spectral domain approach to reduce the problem to a two-dimensional one by eliminating the z-dependence.

The transformations used are given by

$$A_x = \frac{1}{2\pi}\int_{-\infty}^{\infty} \widetilde{A}_x\, e^{jk_z z}\, dk_z \tag{11}$$

$$\widetilde{A}_x = \int_{-\infty}^{\infty} A_x\, e^{-jk_z z}\, dz. \tag{12}$$

This gives for LSE modes

$$\widetilde{E}_x = 0 \tag{13}$$

$$\widetilde{E}_y = j\frac{k_z}{\epsilon}\widetilde{F}_x \tag{14}$$

$$\widetilde{E}_z = -\frac{1}{\epsilon}\frac{\partial}{\partial y}\widetilde{F}_x \tag{15}$$

$$\widetilde{H}_x = -\frac{1}{j\omega\epsilon\mu}(k^2 - k_z^2)\widetilde{F}_x \tag{16}$$

$$\widetilde{H}_y = -\frac{1}{j\omega\epsilon\mu}\frac{\partial^2}{\partial x \partial y}\widetilde{F}_x \tag{17}$$

$$\widetilde{H}_z = -\frac{k_z}{\omega\epsilon\mu}\frac{\partial}{\partial x}\widetilde{F}_x \tag{18}$$

and for LSM modes,

$$\widetilde{H}_x = 0 \tag{19}$$

$$\widetilde{H}_y = j\frac{k_z}{\mu}\widetilde{A}_x \tag{20}$$

$$\widetilde{H}_z = -\frac{1}{\mu}\frac{\partial}{\partial y}\widetilde{A}_x \tag{21}$$

$$\widetilde{E}_x = \frac{1}{j\omega\epsilon\mu}(k^2 - k_z^2)\widetilde{A}_x \tag{22}$$

$$\widetilde{E}_y = \frac{1}{j\omega\epsilon\mu}\frac{\partial^2}{\partial x \partial y}\widetilde{A}_x \tag{23}$$

$$\widetilde{E}_z = \frac{k_z}{\omega\epsilon\mu}\frac{\partial}{\partial x}\widetilde{A}_x \tag{24}$$

The general solution to the wave equation in each region can be obtained by the

method of separation of variables as

$$\tilde{A}_x^{(I)} = \sum_m^{\infty} a_{mn} \cos(k_{x2}(x-a)) \sin(\frac{m\pi y}{b}) \tag{25}$$

$$\tilde{A}_x^{(II)} = \sum_m^{\infty} [b_{mn} \cos(k_{x2}x) + c_{mn} \sin(k_{x2}x)] \sin(\frac{m\pi y}{b}) \tag{26}$$

$$\tilde{F}_x^{(I)} = \sum_m^{\infty} d_{mn} \sin(k_{x2}(x-a)) \cos(\frac{m\pi y}{b}) \tag{27}$$

$$\tilde{F}_x^{(II)} = \sum_m^{\infty} [f_{mn} \cos(k_{x2}x) + g_{mn} \sin(k_{x2}x)] \cos(\frac{m\pi y}{b}) \tag{28}$$

where k_{x1} and k_{x2} represent the wave numbers in the dielectric layer and in the air region respectively and (I), (II) correspond to the air region above and below the point source respectively. The boundary conditions on the perfectly conducting walls have been used to derive these expressions. The problem then consists of solving for the six unknown coefficients a_{mn}, b_{mn}, c_{mn}, d_{mn}, f_{mn} and g_{mn} using the following boundary conditions on the $x = x_0$ interface in the Fourier domain.

$$\widetilde{H}_y^{(I)} - \widetilde{H}_y^{(II)} = \delta(y-y')e^{-jk_z z'} \tag{29}$$

$$\tilde{E}_y^{(I)} = \tilde{E}_y^{(II)} \tag{30}$$

$$\tilde{E}_z^{(I)} = \tilde{E}_z^{(II)} \tag{31}$$

$$\widetilde{H}_z^{(I)} = \widetilde{H}_z^{(II)}. \tag{32}$$

Also impedance boundary conditions are used on the interface as

$$\left(\frac{\tilde{E}_y^{(II)}}{\widetilde{H}_z^{(II)}}\right)^{LSE} = \eta_e \tag{33}$$

$$\left(\frac{\tilde{E}_y^{(II)}}{\widetilde{H}_z^{(II)}}\right)^{LSM} = \eta_m \tag{34}$$

These impedances η_e and η_m can be found using the sending end impedance formulas for transmission lines. For a single layer these are, for LSE and LSM modes

respectively

$$\eta_e = -j\frac{\omega\mu_1}{k_{x1}}\tan(k_{x1}h) \tag{35}$$

$$\eta_m = -j\frac{k_{x1}}{\omega\epsilon_d}\tan(k_{x1}h) \tag{36}$$

After solving for the six coefficients, one obtains for the electric field due to a dipole above a substrate

$$\begin{aligned}\tilde{E}_z^{II} = \frac{1}{\epsilon}\sum_{m=1}^{\infty} j\frac{\epsilon_m\mu}{b}\sin(k_{x2}(x_0-a'))\frac{1}{k_z^2+(\frac{m\pi}{b})^2}\sin(\frac{m\pi}{b}y')\sin(\frac{m\pi}{b}y)e^{-jk_z z'} \\ ((\frac{m\pi}{b})^2\frac{\omega\epsilon}{k_{x2}}\frac{k_{x2}\sin(k_{x1}h)\cos(k_{x2}x)+k_{x1}\cos(k_{x1}h)\sin(k_{x2}x)}{\cos(k_{x2}(x_0-a'))(k_{x2}\sin(k_{x1}h)\cos(k_{x2}x_0)+k_{x1}\cos(k_{x1}h)\sin(k_{x2}x_0)} \\ \frac{1}{+\sin(k_{x2}(x_0-a'))(k_{x2}\sin(k_{x1}h)\sin(k_{x2}x_0)-k_{x1}\cos(k_{x1}h)\cos(k_{x2}x_0))} \\ -\frac{k_z^2k_{x2}}{\omega\mu}\frac{\epsilon_r k_{x2}\sin(k_{x2}x)\cos(k_{x1}h)+k_{x1}\cos(k_{x2}x)\sin(k_{x1}h)}{-\cos(k_{x2}(x_0-a'))(\epsilon_r k_{x2}\cos(k_{x1}h)\sin(k_{x2}x_0)+k_{x1}\sin(k_{x1}h)\cos(k_{x2}x_0} \\ \frac{1}{+\sin(k_{x2}(x_0-a'))(k_{x2}\epsilon_r\cos(k_{x1}h)\cos(k_{x2}x_0)-k_{x1}\sin(k_{x1}h)\sin(k_{x2}x_0))}).\end{aligned} \tag{3}$$

When restoring the point source on the interface $x = x_0$, the electric field in (37) therefore becomes

$$\begin{aligned}\tilde{E}_z^{II} = -j\omega\mu\frac{2}{b}\sum_{m=1}^{\infty}\sin(k_{x2}a')\sin(\frac{m\pi}{b}y')\sin(\frac{m\pi}{b}y)e^{-jk_z z'} \\ \frac{1}{k_z^2+(\frac{m\pi}{b})^2}(\frac{(\frac{m\pi}{b})^2\sin(k_{x1}h)}{k_{x2}\sin(k_{x1}h)\cos(k_{x2}a')+k_{x1}\cos(k_{x1}h)\sin(k_{x2}a')} \\ +\frac{k_z^2k_{x2}k_{x1}}{k_0^2}\frac{\sin(k_{x1}h)}{k_{x1}\sin(k_{x1}h)\cos(k_{x2}a')+k_{x2}\epsilon_r\cos(k_{x1}h)\sin(k_{x2}a')}).\end{aligned} \tag{38}$$

The denominator of each of the two terms inside the brackets is seen to correspond to the transcendental equations for LSE and LSM modes. Therefore we can write the $\tilde{E}$ fields as

$$\tilde{E}_z^{(II)}|_{x=x_0} = \tilde{E}_z|_{LSE} + \tilde{E}_z|_{LSM} \tag{39}$$

The equation (38) corresponds to the Fourier transform of the Green's function of the problem, namely $\tilde{\tilde{\bar{G}}}_{zz}$. Its inverse Fourier transform as defined in (11) is then given by

$$\bar{\bar{G}}_{zz} = \frac{1}{2\pi}\int_{-\infty}^{\infty} \tilde{\tilde{\bar{G}}}_{zz}\, e^{jk_z z}\, dk_z. \tag{40}$$

2.3 Electric field on the strip

Assuming that the strip is thin enough in the y-direction, we can propose a Maxwellian distribution [8] for the current density on the microstrip as

$$J_z(x', y', z') = \frac{2}{\pi w}\,\delta(x' - x_0)\,\frac{f(y)}{\sqrt{1 - \left[\frac{2}{w}(y' - y_0)\right]^2}}\, e^{jk_z^{MS} z'} \tag{41}$$

where w is the width of the line and k_z^{MS} is the unknown microstrip propagation constant. The function $f(y)$ allows for single or multiple strips on the air-dielectric interface. Chebyshev and Legendre polynomials have been used recently for the current distribution [7]. This study will first focus on a single microstrip centered in the y-direction. In that particular case $f(y)$ reduces to unity. The electric field due to this current distribution has a variation in x', y' and z' where the corresponding integrals are

$$\widetilde{I_x} = \int_0^{a'} \delta(x' - x_0)dx' \tag{42}$$

$$\widetilde{I_y} = \int_{y_0 - \frac{w}{2}}^{y_0 + \frac{w}{2}} \frac{2}{\pi w}\,\sin\left(\frac{m\pi}{b} y'\right)\frac{1}{\sqrt{1 - \left[\frac{2}{w}(y' - y_0)\right]^2}}\, dy' \tag{43}$$

$$\tilde{I}_z = \int_{-\infty}^{+\infty} e^{jk_z^{MS} z'}\, e^{jk_z|z - z'|}\, dz'. \tag{44}$$

The goal of this study is to find the dispersion characteristics of a centered, narrow microstrip line. To this end, the electric field on the interface $x = x_0$ is calculated

as follows

$$E_z(x=x_0) = \int\int \bar{\bar{G}}_{zz}(x=x_0)\, J_z(y',z')\, dy'\, dz'. \tag{45}$$

Substituting (38) into (45), we get

$$\begin{aligned} E_z(x=x_0) \;=\; & \frac{1}{2\pi}\int_{y_0-\frac{w}{2}}^{y_0+\frac{w}{2}}\int_{-\infty}^{+\infty}\int_{-\infty}^{+\infty} -j\omega\mu\frac{2}{b}\sum_{m=1}^{\infty}\sin(k_{x2}a')\sin(\frac{m\pi}{b}y')\sin(\frac{m\pi}{b}y) \\ & \frac{1}{k_z^2+(\frac{m\pi}{b})^2}\Big(\frac{(\frac{m\pi}{b})^2\sin(k_{x1}h)}{k_{x2}\sin(k_{x1}h)\cos(k_{x2}a')+k_{x1}\cos(k_{x1}h)\sin(k_{x2}a')} \\ & +\frac{k_z^2k_{x2}k_{x1}}{k_0^2}\frac{\sin(k_{x1}h)}{k_{x1}\sin(k_{x1}h)\cos(k_{x2}a')+k_{x2}\epsilon_r\cos(k_{x1}h)\sin(k_{x2}a')}\Big) \\ & \frac{2}{\pi w}\frac{1}{\sqrt{1-\left[\frac{2}{w}(y'-y_0)\right]^2}}\, e^{jk_z^{MS}z'}e^{-jk_zz'}\, dy'\, dz'\, dk_z. \end{aligned} \tag{46}$$

or more simply

$$\begin{aligned} E_z(x=x_0) \;=\; & \frac{1}{2\pi}\sum_{m=1}^{\infty}\int_{y_0-\frac{w}{2}}^{y_0+\frac{w}{2}}\int_{-\infty}^{+\infty}\int_{-\infty}^{+\infty}\phi(y,m,k_{x1},k_{x2},k_z)\sin(\frac{m\pi}{b}y') \\ & \frac{2}{\pi w}\frac{1}{\sqrt{1-\left[\frac{2}{w}(y'-y_0)\right]^2}}\, e^{-j(k_z-k_z^{MS})z'}\, dy'\, dz'\, dk_z. \end{aligned} \tag{47}$$

Evaluating the integration in y' (see Appendix F, [9]), one gets

$$\begin{aligned} E_z(x=x_0) \;=\; & \frac{1}{2\pi}\sum_{m=1}^{\infty}\int_{-\infty}^{+\infty}\int_{-\infty}^{+\infty}\phi(y,m,k_{x1},k_{x2},k_z)\sin(\frac{m\pi}{b}y_0) \\ & J_0(\frac{m\pi}{b}\frac{w}{2})\, e^{j(k_z-k_z^{MS})z'}\, dz'\, dk_z \qquad (48) \\ =\; & \frac{1}{2\pi}\sum_{m=1}^{\infty}\int_{-\infty}^{+\infty}\phi(y,m,k_{x1},k_{x2},k_z)\sin(\frac{m\pi}{b}y_0) \\ & J_0(\frac{m\pi}{b}\frac{w}{2})\delta(k_z-k_z^{MS})\, dk_z \qquad (49) \\ =\; & \frac{1}{2\pi}\sum_{m=1}^{\infty}\phi(y,m,k_{x1},k_{x2},k_z)\sin(\frac{m\pi}{b}y_0) \\ & J_0(\frac{m\pi}{b}\frac{w}{2})|_{k_z=k_z^{MS}} \qquad (50) \\ & \qquad (51) \end{aligned}$$

or

$$
\begin{aligned}
E_z(x=x_0) \;=\; & \frac{1}{2\pi}\sum_{m=1}^{\infty} -j\omega\mu\frac{2}{b}\sin(k_{x2}a')\sin(\frac{m\pi}{b}y) \\
& \frac{1}{k_z^2+(\frac{m\pi}{b})^2}\Big(\frac{(\frac{m\pi}{b})^2\sin(k_{x1}h)}{k_{x2}\sin(k_{x1}h)\cos(k_{x2}a')+k_{x1}\cos(k_{x1}h)\sin(k_{x2}a')} \\
& +\frac{k_z^2k_{x2}k_{x1}}{k_0^2}\frac{\sin(k_{x1}h)}{k_{x1}\sin(k_{x1}h)\cos(k_{x2}a')+k_{x2}\epsilon_r\cos(k_{x1}h)\sin(k_{x2}a')}\Big) \\
& \sin(\frac{m\pi}{b}y_0)\,J_0(\frac{m\pi}{b}\frac{w}{2})|_{k_x=k_x^{MS}}
\end{aligned}
\tag{52}
$$

It can be noted that only the odd modes in m will add up when the strip is centered in the y-direction. One more condition needs to be applied, i.e. the boundary condition on the microstrip. For perfect conductors, the tangential electric field vanishes on the strip. In this study, we assume the strip to have a finite non-zero surface impedance. This impedance varies both with frequency and space in the y-direction. The width is assumed large compared to the thickness of the strip but the latter need not be large compared to the skin depth. A definition was proposed in [10],[11] for the surface impedance as

$$Z(f,y) = (R + j\omega L_{in})w \tag{53}$$

where R and L_{in} are the per unit length resistance and internal inductance of the microstrip. By definition, the surface impedance is also given by

$$\frac{E_z}{H_y} = -Z(f,y) \tag{54}$$

which implies that

$$H_y = J_z \tag{55}$$

since

$$\hat{n} \times H_y \hat{y} = \bar{J} \tag{56}$$

Thus

$$E_z + Z(f,y)J_z = 0 \tag{57}$$

The integral equation for the electric field in the z-direction is given by

$$E_z = \frac{1}{j\omega\epsilon\mu} \int_{-\infty}^{+\infty} \int_{y_0-\frac{w}{2}}^{y_0+\frac{w}{2}} (k_0^2 \bar{\bar{I}} + \bar{\nabla}\bar{\nabla}) \cdot \bar{\bar{G}} \cdot \bar{J}\, dy'\, dz' \tag{58}$$

where $\bar{J}$ is a z-directed current with amplitude given by (41). To minimize the error function, we integrate over the strip after multiplying by a test function. A pulse function has been used in this study. The problem then amounts to solving the following equation for the microstrip propagation constant at the plane $z = 0$.

$$\int_{y_0-\frac{w}{2}}^{y_0+\frac{w}{2}} [E_z + Z(f,y)J_z]\, dy \;=\; 0 \tag{59}$$

or

$$\begin{aligned}
&-j\omega\mu \frac{1}{\pi^2} \sum_{m=1}^{\infty} \frac{1}{m} \sin(k_{x2}a') \sin(k_{x1}h) \sin(\frac{m\pi}{b}\frac{w}{2}) \sin(\frac{m\pi}{b}y_0)^2 \\
&J_0(\frac{m\pi}{b}\frac{w}{2}) \frac{1}{k_z^2 + (\frac{m\pi}{b})^2} \Big(\frac{(\frac{m\pi}{b})^2}{k_{x2}\sin(k_{x1}h)\cos(k_{x2}a') + k_{x1}\cos(k_{x1}h)\sin(k_{x2}a')} \\
&+ \frac{k_z^2 k_{x2} k_{x1}}{k_0^2} \frac{1}{k_{x1}\sin(k_{x1}h)\cos(k_{x2}a') + k_{x2}\epsilon_r \cos(k_{x1}h)\sin(k_{x2}a')} \Big) \Big|_{k_z = k_z^{MS}} \\
&+ \hat{Z}(f) = 0
\end{aligned} \tag{60}$$

where $\hat{Z}(f)$ represents now an average impedance integrated over the width of the strip. This expression can be easily programed in a personal computer to evaluate the propagation constant of various microstrip modes.

3 Discussion

Based on the theory derived in the previous section, a computer program has been developed to calculate the propagation constant of a lossy microstrip line. The equation (60) is solved for k_z^{MS} with as many as a hundred modes to insure convergence. The Muller's algorithm is used to calculate the complex roots of this function. Preliminary data were calculated for the case of a lossy substrate with a perfectly conducting microstrip structure. The results have been found to give good agreement with [12], within the readability of the quoted results. Also it is seen that as one decreases the size of the structure while keeping the different ratios the same, the effect of conductor losses on the propagation constant of the quasi-TEM microstrip mode becomes significant. This is due in part to the dominant effect of dielectric losses for thicker substrates. The effect of frequency with no dielectric loss is shown in Figs. 3,4,5,6 and also Figure 7. More research needs to be performed in this area, for example on the effect of conductor losses on higher order modes, and the validity of different current distributions on the strip.

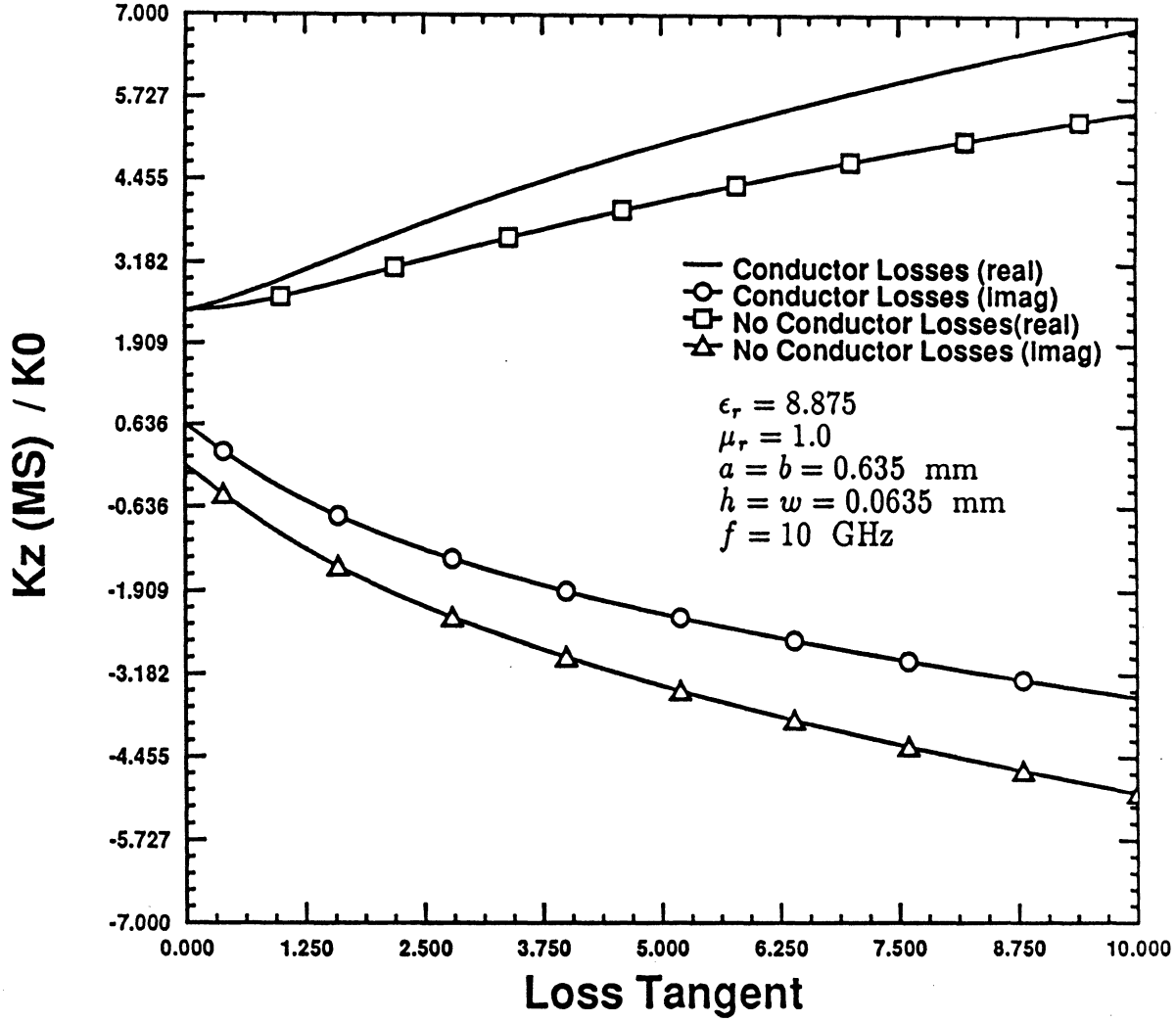

Figure 3: Propagation constant vs. loss tangent at $f = 10$ GIIz

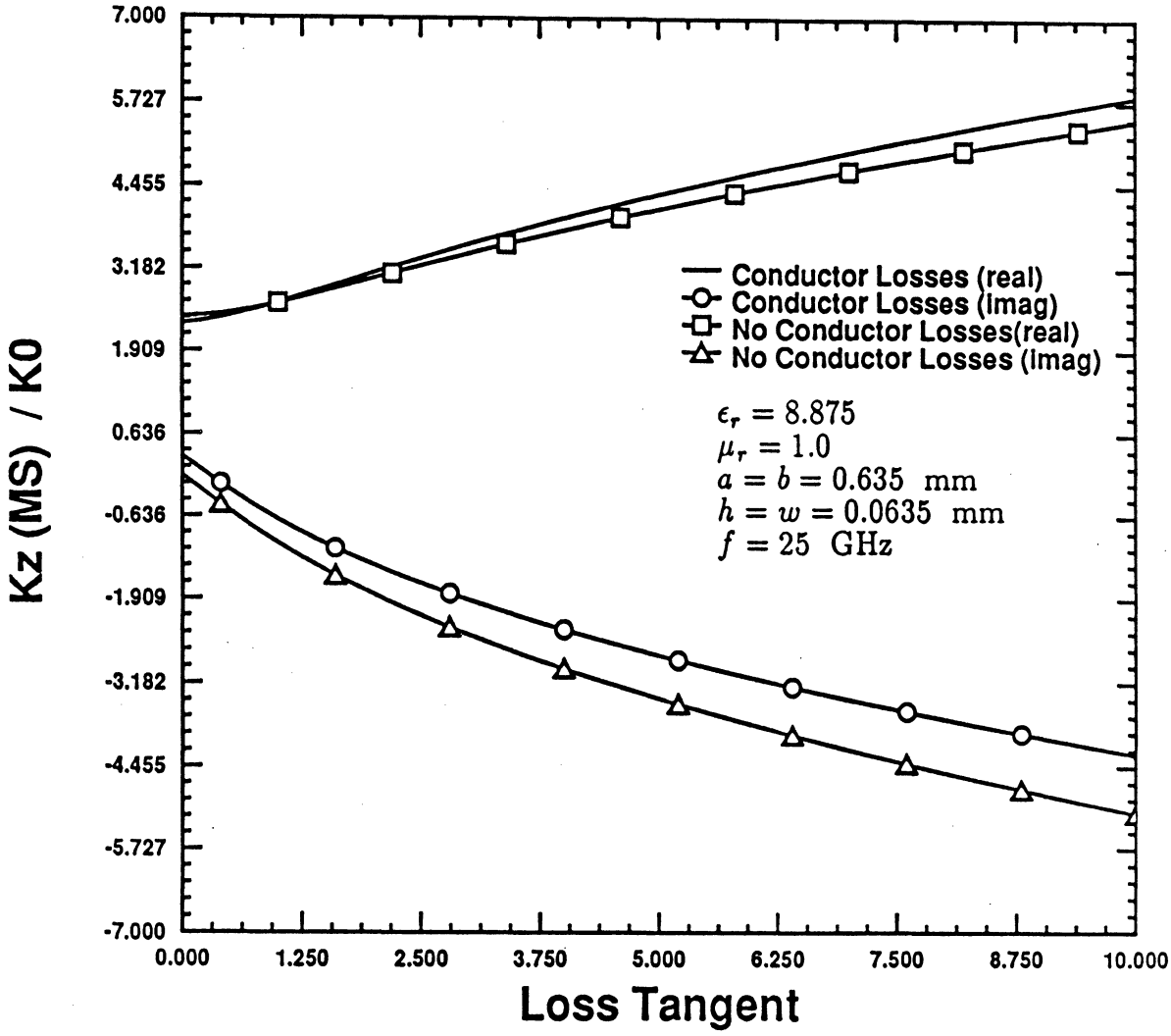

Figure 4: Propagation constant vs. loss tangent at $f = 25$ GHz

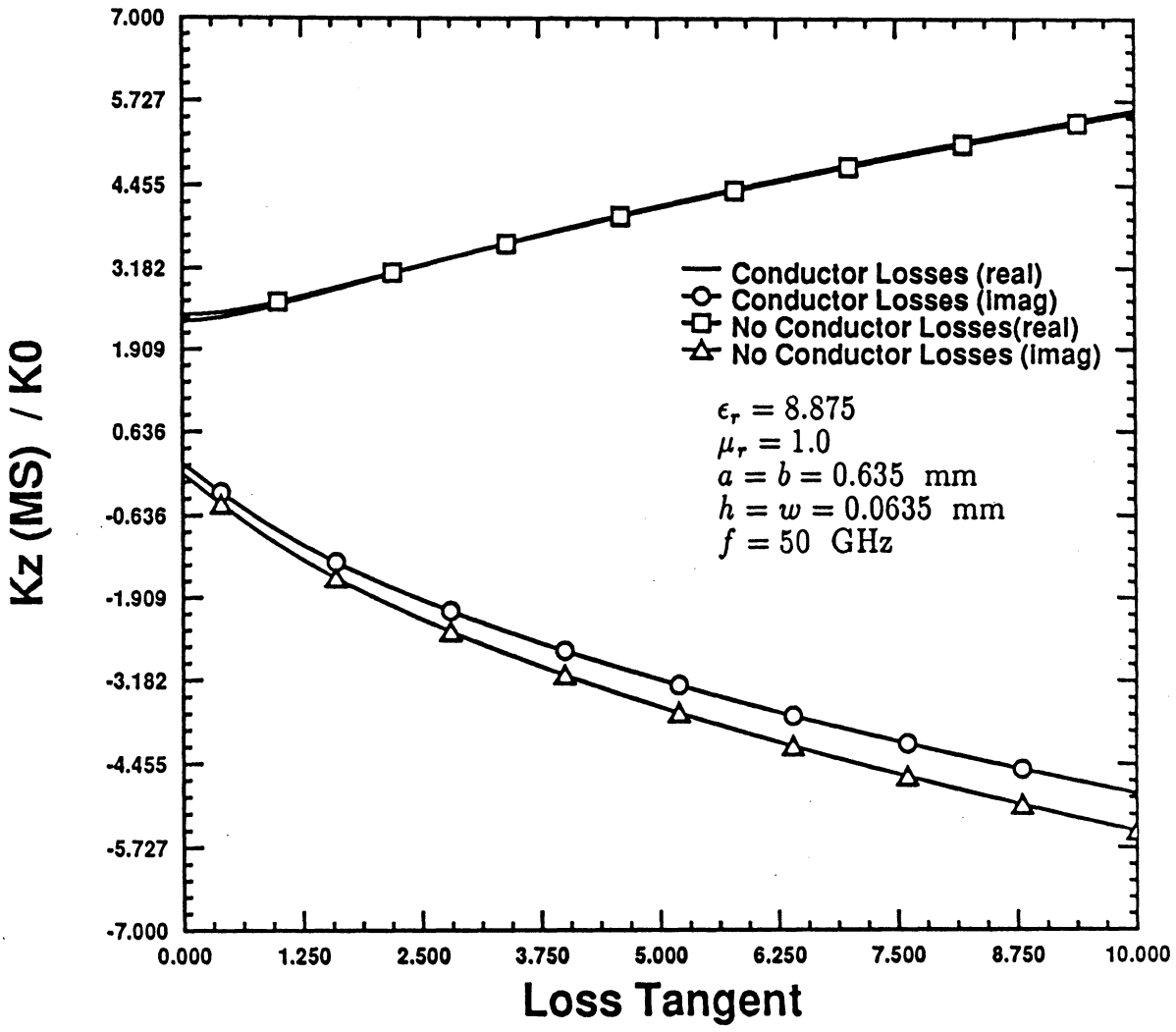

Figure 5: Propagation constant vs. loss tangent at $f = 50$ GHz

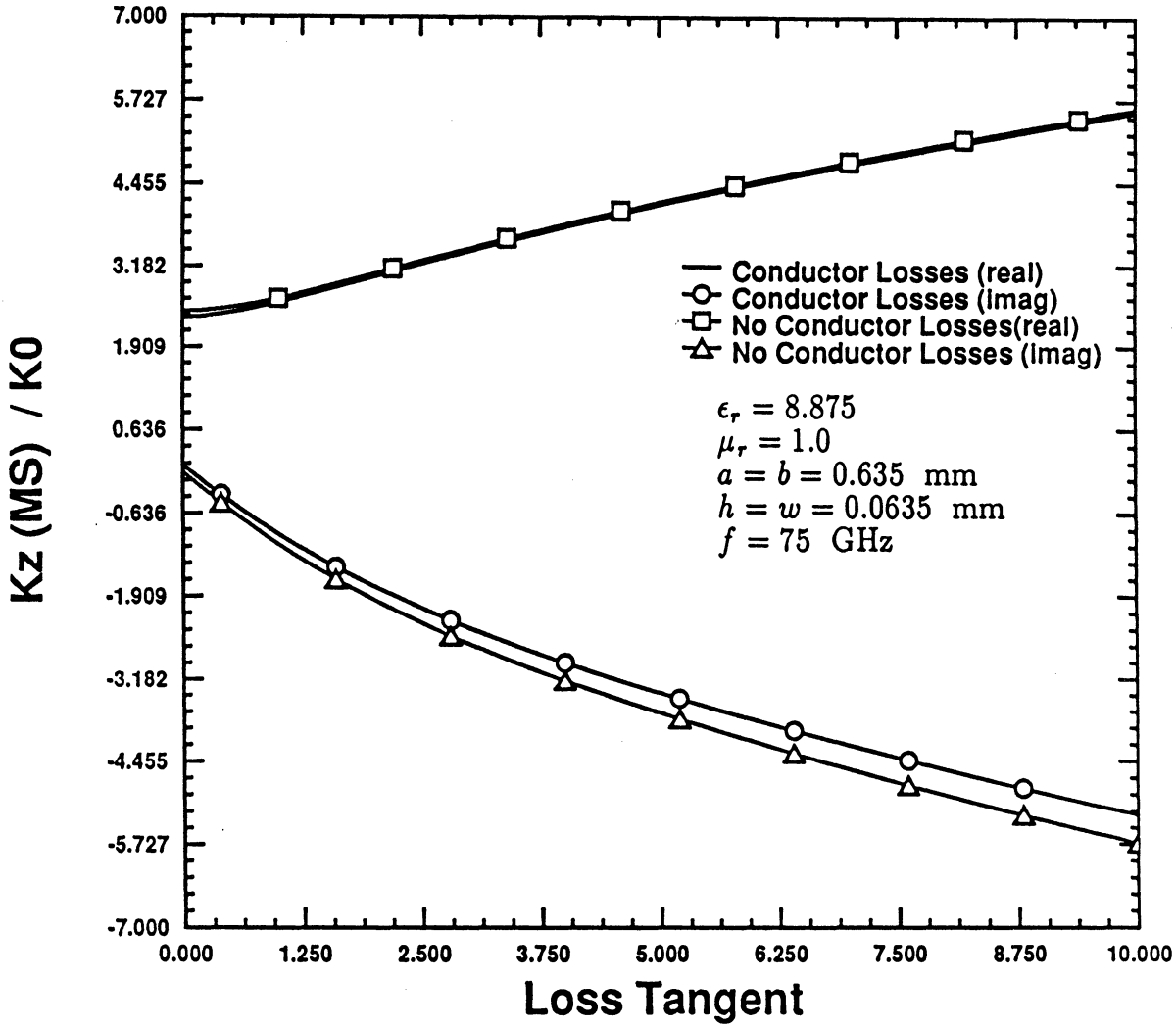

Figure 6: Propagation constant vs. loss tangent at $f = 75$ GHz

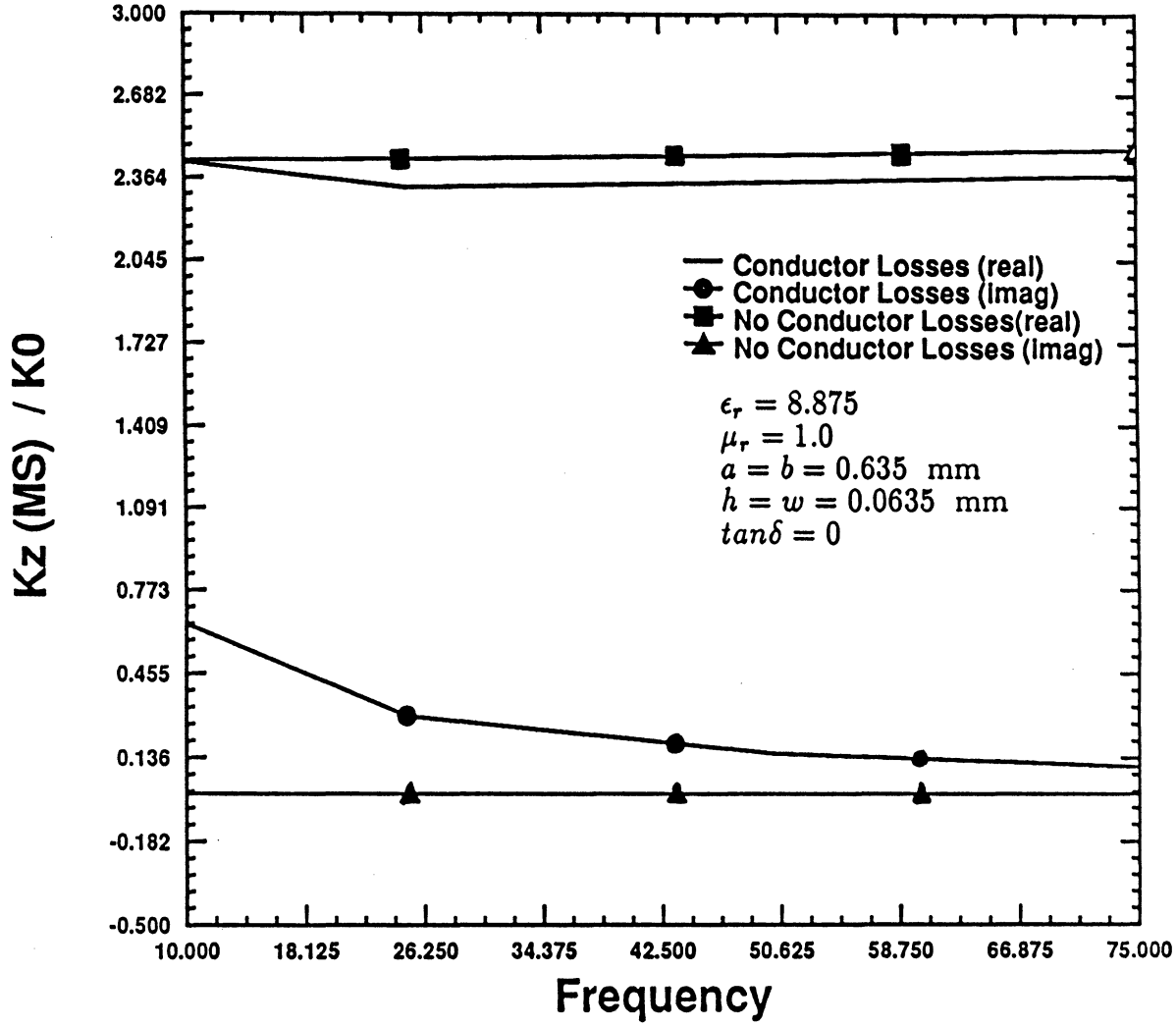

Figure 7: Propagation constant vs. frequency at $tan\delta = 0$

References

[1] R. A. Pucel, D. J. Masse, C. P. Hartwig, "Losses in Microstrip," *IEEE Trans. Microwave Theory Tech.*, vol. MTT-16, p 342, June 1968.

[2] H. A. Wheeler, "Transmission-line properties of a strip on a dielectric sheet on a plane," *IEEE Trans. Microwave Theory Tech.*, vol. MTT-25, p 631, August 1977.

[3] M.V. Schneider, " Microstrip Lines for Microwave Integrated Circuits," *The Bell System Technical Journal*, pp 1421-1444, May-June 1969.

[4] B.E. Spielman, "Dissipation Loss Effects in Isolated and Coupled Transmission Lines," *IEEE Trans. Microwave Theory Tech.*, vol. MTT-25, pp 648-655, August 1977.

[5] D. Mirshekar-Syahkal, J. B. Davies, "Accurate Solution of Microstrip and Coplanar Structures for Dispersion and for Dielectric and Conductor Losses", *IEEE Trans. Microwave Theory Tech.*, vol. MTT-27, p 694, July 1979.

[6] R.F. Harrington, "Time-Harmonic Electromagnetic Fields," 3rd. ed., McGraw-Hill Book Co., 1961.

[7] C.J. Railton, T.Rozzi, "Complex Modes in Boxed Microstrip," *IEEE Trans. Microwave Theory Tech.*, vol. MTT-36, p 865, May 1988.

[8] J. C. Maxwell, " A Treatise on Electricity and Magnetism," 3rd. ed., vol.1, New York: Dover 1954, pp 296-297.

[9] L. P. Dunleavy, "Discontinuity Characterization in Shielded Microstrip: a Theoretical and Experimental Study", *Ph.D. Dissertation*, the University of Michigan, April 1988.

[10] A.C. Cangellaris, University of Arizona, Personal Communication, April 1988.

[11] A.C. Cangellaris, "The importance of skin-effect in microstrip lines at high frequencies", *IEEE MTT-International Symposium Digest*, p 197, May 1988.

[12] D. Mirshekar-Syahkal, "An Accurate Determination of Dielectric Loss Effect in Monolithic Microwave Integrated Circuits Including Microstrip and Coupled Microstrip Lines," *IEEE Trans. Microwave Theory Tech.*, vol. MTT-31, pp 950-954, November 1983.

Appendix E

"Theoretical Characterization of an Air-Bridge"
M.E. Coluzzi and P.B. Katehi

THEORETICAL CHARACTERIZATION OF AIR-BRIDGES

Michael E. Coluzzi
Pisti B. Katehi
Radiation Laboratory
Department of Electrical Engineering
and Computer Science
The University of Michigan
Ann Arbor, MI 48109

June 1988

Abstract-The theoretical analysis of an enclosed air-bridge is presented. This includes a derivation of the Green's function in the x and z directions which is used to find the current distribution on the conducting strips of the air-bridge. Boundary conditions at the interfaces are applied and the numerical technique Method of Moments is used to solve the integral equation for the unknown current. Upon derivation of the current distribution on the conductors, an ideal transmission line model is applied to obtain the scattering parameters of the structure.

Contents

1 Introduction 1

2 Evaluation of the unknown current 2

2.1 Formulation of the Integral Equation 3

2.2 Derivation of Green's function 5

2.2.1 Derivation of the Green's function for a x-directed current . 6

2.2.2 Derivation of the Green's function for a z-directed current. . 12

2.2.3 Summary of Green's function determination 20

2.3 Application of Method of Moments 20

2.4 Matrix Equation 34

3 Scattering Parameters 34

4 Summary 34

1 Introduction

Millimeter wave technology concerns itself with that portion of the electromagnetic spectrum between 0.3 Ghz and 300 Ghz, corresponding to wavelengths of 1000 mm to 1mm. Effective quasi-static techniques have been developed for the lower frequencies (0.3 Ghz to 3 Ghz) but for the higher frequency part of the spectrum, a full-wave analysis must be employed.

Millimeter and microwave systems may be overshadowed by infarred and optical systems but limitations to the latter, in particular their disadvantages in fog, dust, rain, and nighttime viewing support further development of the former. As with many technologies, the number of applications will increase with the passage of time.

The typical millimeter microwave integrated circuit contains associated active and passive elements interconnected by transmission lines. In integrating these components together, various discontinuities arise where evanescent fields and surface waves play an important role in their operation. Work has been done to model these discontinuities with lumped elements but the numerical techniques used to derive equivalent circuits are either frequency bound or dependent.

Here we present a full-wave analysis, which in not frequency bound or dependent, to analyze an air-bridge structure. The resultant expressions and methods used are general enough to be applied to an array of three dimensional problems.

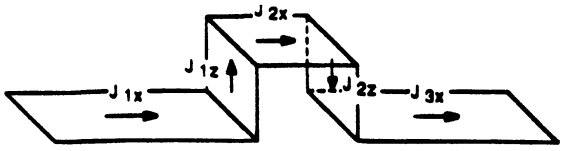

a. One dimensional view highlighting current directions

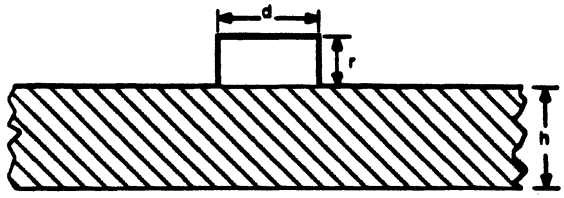

b. Two dimensional view highlighting dimensions

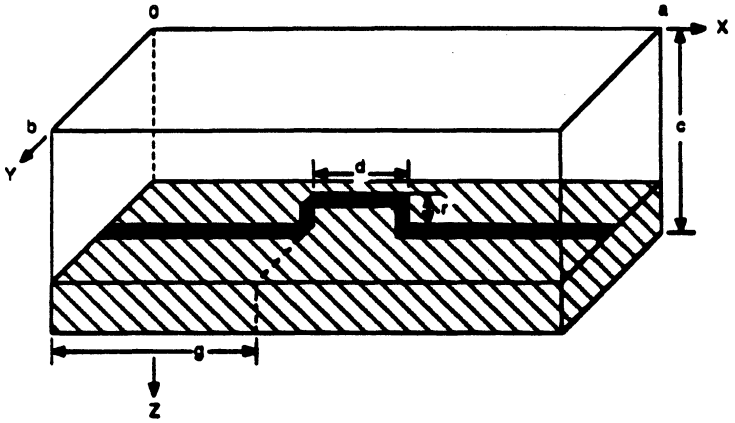

c. Three dimensional view highlighting relative geometry

Figure 1: Air-bridge in enclosed microstrip.

2 Evaluation of the unknown current

In our problem the current distribution on the structure of interest must be determined accurately. Then by the use of an ideal transmission line model, the scattering parameters can be evaluated. In obtaining the current distribution, Pocktnigton's integral equation is solved numerically.

The formulation of the Pocktnigton's integral equation and the solution for the given structure are presented in the following work. Our structure under study is shown in Fig.1.

2.1 Formulation of the Integral Equation

Through the manipulation of Maxwell's equations [1]

$$\overline{\nabla} \times \overline{E} = -j\omega\mu\overline{H} \tag{1}$$

$$\overline{\nabla} \times \overline{H} = j\omega\mu\overline{E} + \overline{J} \tag{2}$$

$$\overline{\nabla} \cdot \epsilon\overline{E} = \rho \tag{3}$$

$$\overline{\nabla} \cdot \mu\overline{H} = 0 \tag{4}$$

along with the representation of the magnetic vector potential $\overline{A}$

$$\overline{H} = \frac{\overline{\nabla} \times \overline{A}}{\mu} \tag{5}$$

one arrives at an expression relating current and the magnetic vector potential

$$\nabla^2\overline{A} + k^2\overline{A} = -\mu\overline{J}. \tag{6}$$

When the current $\overline{J}$ is represented by a dirac delta function in equation (6), the Green's function becomes a solution as shown by the equation

$$\nabla^2\overline{\overline{G}} + k^2\overline{\overline{G}} = -\mu\overline{\overline{I}}\delta(\overline{r} - \overline{r}'). \tag{7}$$

To obtain a unique solution that applies to the specific geometry as shown in Fig.1, one must apply the characteristic boundary conditions of the structure. Note that we have introduced the dyadic form as we need to be able to describe fields which are produced by a current of arbitrary orientation.

[1] throughout this report an $e^{j\omega t}$ time convention is assumed and suppressed

For the case of a single x-directed current, the unit dyadic $\overline{\overline{I}}$ takes on the form;

$$\overline{\overline{I}} = \hat{x}\hat{x}. \tag{8}$$

The vector representation of this current is

$$J = \delta(\overline{r} - \overline{r}')\hat{x}. \tag{9}$$

Equation (9) represents a dipole directed in the x-direction and parallel to the interface between regions II and III. It has been shown by Sommerfeld that the magnetic vector potential of this structure needs to have two components so that the appropriate boundary conditions are satisfied. This dictates that $\overline{A}$ must have one component parallel to the current source and another parallel to the interface;

$$\overline{A}^{i\,2} = A^i_x\hat{x} + A^i_z\hat{z}. \tag{10}$$

The integral equation which relates the magnetic vector potential to the current of interest is written as

$$\overline{A}^i = \mu \int\int\int_V \overline{\overline{G}}^i \cdot \overline{J} dV \tag{11}$$

where the dyadic Green's function $\overline{\overline{G}}^i$ is uniquely defined by the structure under investigation and takes on the general form

$$\overline{\overline{G}}^i = \begin{bmatrix} G^i_{xx}\hat{x}\hat{x} & G^i_{xy}\hat{x}\hat{y} & G^i_{xz}\hat{x}\hat{z} \\ G^i_{yx}\hat{y}\hat{x} & G^i_{yy}\hat{y}\hat{y} & G^i_{yz}\hat{y}\hat{z} \\ G^i_{zx}\hat{z}\hat{x} & G^i_{zy}\hat{z}\hat{y} & G^i_{zz}\hat{z}\hat{z} \end{bmatrix}.$$

[2] i denotes for which region (I, II, or III) the equation applies as defined in Fig.2

In the case of a single directional current in the x-direction, the dyadic equation has only two components,

$$\overline{\overline{G}}^{i} = G^{i}_{xx}\hat{x}\hat{x} + G^{i}_{zx}\hat{z}\hat{x}. \tag{12}$$

From equations (1)-(5) our electric field is related to the magnetic vector potential by

$$\overline{E} = \frac{\nabla \times \overline{H}}{j\omega\epsilon} = \frac{1}{j\omega\epsilon\mu}\nabla \times (\nabla \times \overline{A}) = \frac{1}{j\omega\epsilon\mu}(k^2\overline{A} + \nabla\nabla \cdot \overline{A}) \tag{13}$$

therefore

$$E_x = -j\omega\left[A_x + \frac{1}{(k^i)^2}\frac{\delta}{\delta x}\left(\frac{\delta A_x}{\delta x} + \frac{\delta A_z}{\delta z}\right)\right] \tag{14}$$

$$E_y = -j\omega\left[\frac{1}{(k^i)^2}\frac{\delta}{\delta y}\left(\frac{A_x}{\delta x} + \frac{\delta A_z}{\delta z}\right)\right] \tag{15}$$

$$E_z = -j\omega\left[A_z + \frac{1}{(k_i)^2}\frac{\delta}{\delta z}\left(\frac{\delta A_x}{\delta x} + \frac{\delta A_z}{\delta z}\right)\right] \tag{16}$$

and through Maxwell's equations,

$$H_x = \frac{1}{\mu}\frac{\delta A_z}{\delta y} \tag{17}$$

$$H_y = \frac{1}{\mu}\left(\frac{\delta A_x}{\delta z} - \frac{\delta A_z}{\delta x}\right) \tag{18}$$

$$H_z = -\frac{1}{\mu}\left(\frac{\delta A_x}{\delta y}\right). \tag{19}$$

2.2 Derivation of Green's function

For our structure pictured in Fig.1 (an air bridge on an enclosed thin microstrip), we require only the derivation of the Green's function for an x- and z-directed current. For the variation of current in the y-direction, we have assumed a Maxwellian distribution. Our first step will be to derive the Green's function considering the x and z components of the current separately.

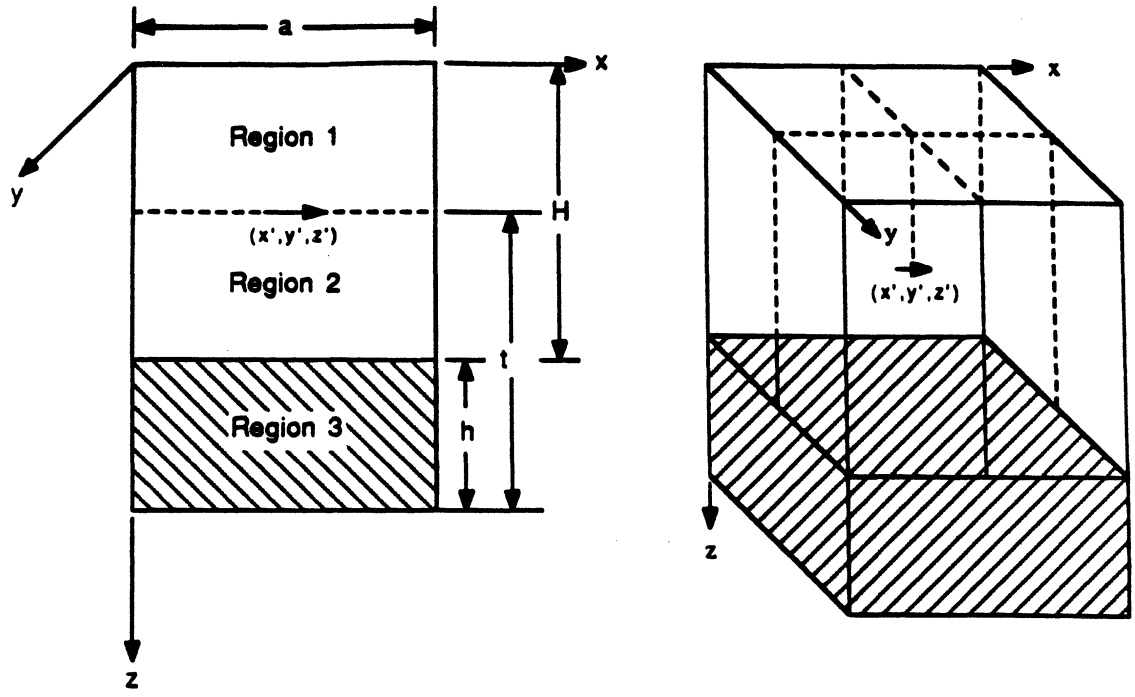

Figure 2: x-directed current above dielectric in enclosed microstrip structure.

2.2.1 Derivation of the Green's function for a x-directed current

With equations (14)-(19) the Green's function can be related to the electric and magnetic fields which have conceivably defined values dictated by the structures electrical characteristics. We begin by stating that the tangential electric fields are zero everywhere on the surface of the walls of the structure;

$$E^i_{y,z} = 0 \; at \; x = 0, a \tag{20}$$

$$E^i_{x,z} = 0 \; at \; y = 0, b \tag{21}$$

$$E^I_{x,y} = 0 \; at \; z = 0 \tag{22}$$

$$E^{III}_{x,y} = 0 \; at \; z = c. \tag{23}$$

Employing separation of variables to the expressions and the established boundary conditions (20)-(23), the following general forms of the green's functions can be derived for each region of interest

$$G^I_{xx} = \sum_{n=0}^{\infty}\sum_{m=1}^{\infty} A^I cos\left(\frac{n\pi x}{a}\right) sin\left(\frac{m\pi y}{b}\right) sin(k^I_z z) \quad (24)$$

$$G^I_{xx} = \sum_{n=1}^{\infty}\sum_{m=1}^{\infty} B^I sin\left(\frac{n\pi x}{a}\right) sin\left(\frac{m\pi y}{b}\right) cos(k^I_z z) \quad (25)$$

$$G^{II}_{xx} = \sum_{n=0}^{\infty}\sum_{m=1}^{\infty} cos\left(\frac{n\pi x}{a}\right) sin\left(\frac{m\pi y}{b}\right) (A^{II} sin(k^{II}_z z) + C^{II} cos(k^{II}_z z)) \quad (26)$$

$$G^{II}_{xx} = \sum_{n=0}^{\infty}\sum_{m=1}^{\infty} cos\left(\frac{n\pi x}{a}\right) sin\left(\frac{m\pi y}{b}\right) (B^{II} sin(k^{II}_z z) + D^{II} cos(k^{II}_z z)) \quad (27)$$

$$G^{III}_{xx} = \sum_{n=0}^{\infty}\sum_{m=1}^{\infty} A^{III} cos\left(\frac{n\pi x}{a}\right) sin\left(\frac{m\pi y}{b}\right) sin(k^{III}_z (z-c)) \quad (28)$$

$$G^{III}_{xx} = \sum_{n=1}^{\infty}\sum_{m=1}^{\infty} B^{III} sin\left(\frac{n\pi x}{a}\right) sin\left(\frac{m\pi y}{b}\right) sin(k^{III}_z (z-c)). \quad (29)$$

In equations (24)-(29) the eigenvalues k_x, k_y, and k_z satisfy the following relations:

$$(k^i)^2 = (k^i_x)^2 + (k^i_y)^2 + (k^i_z)^2$$

$$\text{where } k_x = \left(\frac{m\pi}{a}\right)$$

$$\text{and } k_y = \left(\frac{m\pi}{b}\right)$$

$$k^2 = \omega^2 \mu\epsilon. \quad (30)$$

To determine the unknown coefficients $A^{I,II,III}$ and $B^{I,II,III}$, one should apply boundary conditions at the two interfaces between Regions I, II, and III. Since at

the boundary between Regions I and II there exists no magnetic charge, the normal magnetic field must be continuous across the boundary. Therefore $H_z^I = H_z^{II}$, so

$$A^I sin(k_z^I z') = A^{II} sin(k_z^{II} z') + C^{II} sin(k_z^{II} z') \tag{31}$$

Since there is no electric current in the y direction, the tangential magnetic field is continuous. By substituting this relation into (18), one obtains $H_x^I = H_x^{II}$, therefore

$$B^I cos(k_z^I z') = B^{II} sin(k_z^{II} z') + D^{II} cos(k_z^{II} z') \tag{32}$$

Also, since there is no magnetic current in the x direction, the tangential electric field is continuous. Therefore $E_y^I = E_y^{II}$;

$$A^I sin(k_z^I z') - B^I sin(k_z^I z') =$$
$$B^{II} cos(k_z^{II} z') - D^{II} sin(k_z^{II} z') + A^{II} sin(k_z^{II} z') + C^{II} sin(k_z^{II} z') \tag{33}$$

By applying similar boundary conditions on the interface between Region II and III, the following equations result;

$$A^{II} sin(k_z^{II} H) + C^{II} cos(k_z^{II} H) = A^{III} sin(k_z^{III}(H - c)) \tag{34}$$

$$B^{II} sin(k_z^{II} H) + D^{II} cos(k_z^{II} H) = B^{III} cos(k_z^{III}(H - c)) \tag{35}$$

$$k_z^{II}(A^{II} cos(k_z^{II} H) - C^{II} sin(k_z^{II} H)) = A^{III} k_z^{III} cos(k_z^{III}(H - c)) \tag{36}$$

$$\begin{aligned} &A^{II} sin(k_z^{II} H) + C^{II} cos(k_z^{II} H) \\ &+ \frac{k_z^{II}}{-(\frac{n\pi}{a})} \left(B^{II} cos(k_z^{II} H) - D^{II} sin(k_z^{II} H) \right) \\ &= \frac{1}{\epsilon_{III}} \left(A^{III} sin(k_z^{III}(H - c)) + \frac{B^{III} k_z^{III}}{(\frac{n\pi}{a})} sin(k_z^{III}(H - c)) \right). \end{aligned} \tag{37}$$

Since there does exist an electric current between Regions I and II, the magnetic field between these two boundaries is discontinuous. This discontinunity can be considered by integrating the inhomogenous helmholtz expression over the boundary and using orthogonality. This results in

$$\frac{ab}{\rho}\left(k_z^I A^I cos(k_z^I z') - k_z^{II} A^{II} cos(k_z^{II} z') + k_z^{II} C^{II} sin(k_z^{II} z')\right) = -cos\left(\frac{n\pi x'}{a}\right) sin\left(\frac{m\pi y'}{b}\right) \tag{38}$$

$$\text{where } \rho = \begin{cases} 4 & \text{when } n \neq 0 \\ 2 & \text{when } n = 0 \end{cases}$$

Using these eight relations derived from the boundary conditions, the eight unknown constants, A^I, B^I, A^{II}, B^{II}, C^{III}, D^{II}, A^{III}, B^{III} are found. The resulting Green's functions for a x-directed current above the dielectric upon simplification are

$$G_{xx}^I = \sum_{n=0}^{\infty}\sum_{m=1}^{\infty} \frac{\rho\left[\frac{k_z^{III} - k_z tan(k_z^{III}(H-c))tan(k_z H)}{k_z^{III} tan(k_z H) - k_z tan(k_z^{III}(H-c))} - cot(k_z H)\right]}{abk_z[cot(k_z z')cos(k_z z') - sin(k_z z')]} cos\left(\frac{n\pi x'}{a}\right) sin\left(\frac{m\pi y'}{b}\right) cos\left(\frac{n\pi x}{a}\right) sin\left(\frac{m\pi y}{b}\right) sin(k_z^I z) \tag{39}$$

$$G_{xx}^I = \sum_{n=0}^{\infty}\sum_{m=1}^{\infty} \frac{\rho(1 - tan^2(k_z H))\left(\frac{n\pi}{a}\right)(\epsilon_r^{III} - 1)tan(k_z^{III}(H-c))}{ab[k_z^{III} tan(k_z H) - k_z tan(k_z^{III}(H-c))][cot(k_z z')cos(k_z z') - sin(k_z z')]} cos\left(\frac{n\pi x'}{a}\right) sin\left(\frac{m\pi y'}{b}\right) \frac{1}{k_z^{III} tan(k_z^{III}(H-c)) - \epsilon_r^{III} k_z tan(k_z H)}$$

$$sin\left(\frac{n\pi x}{a}\right) sin\left(\frac{m\pi y}{b}\right) cos(k_z^I z) \tag{40}$$

$$G_{xx}^{II} = \sum_{n=0}^{\infty}\sum_{m=1}^{\infty} \frac{\rho\left[k_z^{III} - k_z tan(k_z^{III}(H-c))tan(k_z H)\right]}{abk_z[cot(k_z z')cos(k_z z') - sin(k_z z')][k_z^{III}tan(k_z H) - k_z tan(k_z^{III}(H-c))]}$$
$$cos\left(\frac{n\pi x}{a}\right) sin\left(\frac{m\pi y}{b}\right) sin(k_z^{II} z) cos\left(\frac{n\pi x'}{a}\right) sin\left(\frac{m\pi y'}{b}\right) +$$
$$\frac{-\rho}{abk_z[cot(k_z z')cos(k_z z') - sin(k_z z')]} cos\left(\frac{n\pi x}{a}\right) sin\left(\frac{m\pi y}{b}\right) cos(k_z^{II} z)$$
$$cos\left(\frac{n\pi x'}{a}\right) sin\left(\frac{m\pi y'}{b}\right) \tag{41}$$

$$G_{xx}^{II} = \sum_{n=0}^{\infty}\sum_{m=1}^{\infty} \frac{\rho\,(1 - tan^2(k_z H))\left(\frac{n\pi}{a}\right)(\epsilon_r^{III} - 1)tan(k_z^{III}(H-c))}{ab[k_z^{III}tan(k_z H) - k_z tan(k_z^{III}(H-c))][cot(k_z z')cos(k_z z') - sin(k_z z')]}$$
$$\frac{1}{[k_z^{III}tan(k_z^{III}(H-c)) - \epsilon_r^{III}tan(k_z H)]} sin\left(\frac{n\pi x}{a}\right) sin\left(\frac{m\pi y}{b}\right) cos(k_z^{II} z)$$
$$cos\left(\frac{n\pi x'}{a}\right) sin\left(\frac{m\pi y'}{b}\right) \tag{42}$$

$$G_{xx}^{III} = \sum_{n=0}^{\infty}\sum_{m=1}^{\infty} \frac{\rho\,(1 - tan^2(k_z H))cos(k_z H)}{ab[cot(k_z z')cos(k_z z') - sin(k_z z')]cos(k_z^{III}(H-c))}$$
$$\frac{1}{[k_z^{III}tan(k_z H) - k_z tan(k_z^{III}(H-c))]}$$
$$cos\left(\frac{n\pi x}{a}\right) sin\left(\frac{m\pi y}{b}\right) sin(k_z^{III}(z-c)) cos\left(\frac{n\pi x'}{a}\right) sin\left(\frac{m\pi y'}{b}\right) \tag{43}$$

$$G_{zx}^{III} = \sum_{n=0}^{\infty}\sum_{m=1}^{\infty} \frac{\rho(1 - tan^2(k_z H))\left(\frac{n\pi}{a}\right)(\epsilon_r^{III} - 1)tan(k_z^{III}(H-c))}{ab[k_z^{III}tan(k_z H) - k_z tan(k_z^{III}(H-c))][cot(k_z z')cos(k_z z') - sin(k_z z')]}$$
$$\frac{sec(k_z^{III}(H-c))}{[k_z^{III}tan(k_z(H-c)) - \epsilon_r^{III}tan(k_z^{III}H)]}$$
$$sin\left(\frac{n\pi x}{a}\right) sin\left(\frac{m\pi y}{b}\right) cos(k_z^{III}(z-c)) cos\left(\frac{n\pi x'}{a}\right) sin\left(\frac{m\pi y'}{b}\right) \tag{44}$$

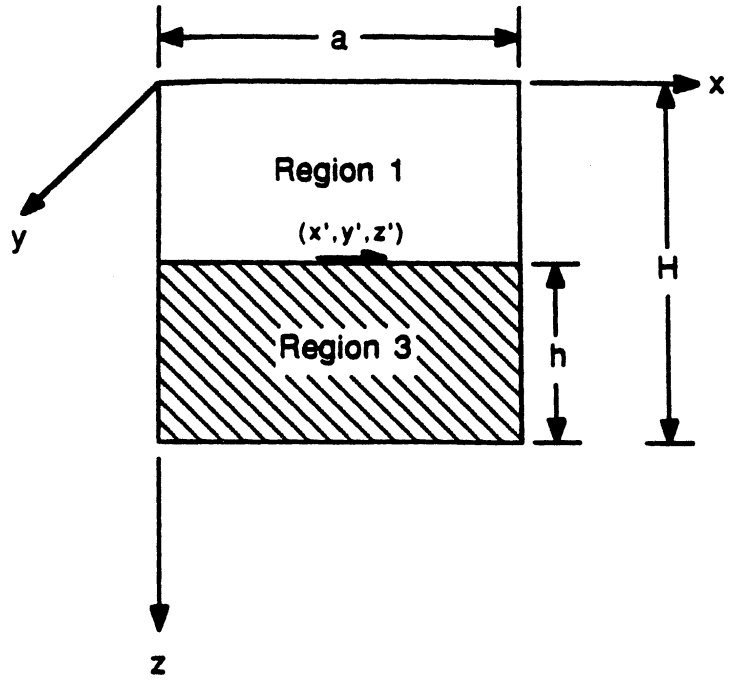

Figure 3: Structure when conducting strip is lowered on to the dielectric.

If the conducting strip is lowered on to the dielectric, we will have only two regions; air representing Region I and dielectric representing Region III.

To formulate the following Green's fuctions for the strip on the dielectric , one simply lets $z' = H$ in the previous expressions.

$$G_{xx}^{I} = \sum_{n=0}^{\infty}\sum_{m=1}^{\infty} \frac{\rho\, tan(k_z^{III}(H-c))}{ab(cos(k_z H))[k_z^{III} tan(k_z H) - k_z tan(k_z^{III}(H-c))]} cos\left(\frac{n\pi x'}{a}\right) sin\left(\frac{m\pi y'}{b}\right) cos\left(\frac{n\pi x}{a}\right) sin\left(\frac{m\pi y}{b}\right) sin(k_z^{I} z) \quad (45)$$

$$G_{zx}^{I} = \sum_{n=0}^{\infty}\sum_{m=1}^{\infty} \frac{\rho\, tan(k_z H)\left(\frac{n\pi}{a}\right)(\epsilon_r^{III}-1) tan(k_z^{III}(H-c))}{ab(cos(k_z H))[k_z^{III} tan(k_z H) - k_z tan(k_z^{III}(H-c))]}$$

$$\frac{1}{[k_z^{III}tan(k_z^{III}(H-c)) - \epsilon_r^{III}k_z tan(k_z H)]} cos\left(\frac{n\pi x'}{a}\right) sin\left(\frac{m\pi y'}{b}\right)$$
$$sin\left(\frac{n\pi x}{a}\right) sin\left(\frac{m\pi y}{b}\right) cos(k_z^I z) \quad (46)$$

$$G_{xx}^{III} = \sum_{n=0}^{\infty}\sum_{m=1}^{\infty} \frac{\rho\, tan(k_z H)}{abcos(k_z^{III}(H-c))[k_z^{III}tan(k_z H) - k_z tan(k_z^{III}(H-c))]}$$
$$cos\left(\frac{n\pi x}{a}\right) sin\left(\frac{m\pi y}{b}\right) sin(k_z^{III}(z-c)) cos\left(\frac{n\pi x'}{a}\right) sin\left(\frac{m\pi y'}{b}\right) \quad (47)$$

$$G_{xx}^{III} = \sum_{n=0}^{\infty}\sum_{m=1}^{\infty} \frac{\rho(\epsilon_r^{III}-1)tan(k_z^{III}(H-c)tan(k_z H)\left(\frac{n\pi}{a}\right)}{abcos(k_z(H-c))[k_z^{III}tan(k_z H) - k_z tan(k_z^{III}(H-c))]}$$
$$\frac{1}{[k_z^{III}tan(k_z^{III}(H-c)) - \epsilon_r^{III}k_z tan(k_z H)]} sin\left(\frac{n\pi x}{a}\right) sin\left(\frac{m\pi y}{b}\right) cos(k_z^{III}(z-c))$$
$$cos\left(\frac{n\pi x'}{a}\right) sin\left(\frac{m\pi y'}{b}\right) \quad (48)$$

2.2.2 Derivation of the Green's function for a z-directed current.

The structure used to consider the z-directed current is pictured in Fig.4. We will simplify our problem separating it into two parts; a primary field problem and a secondary field problem as shown in Fig.5. For a z-directed current only one component of the magnetic vector potential is needed to satisfy the boundary conditions;

$$\overline{A} = \hat{z}Az \quad (49)$$

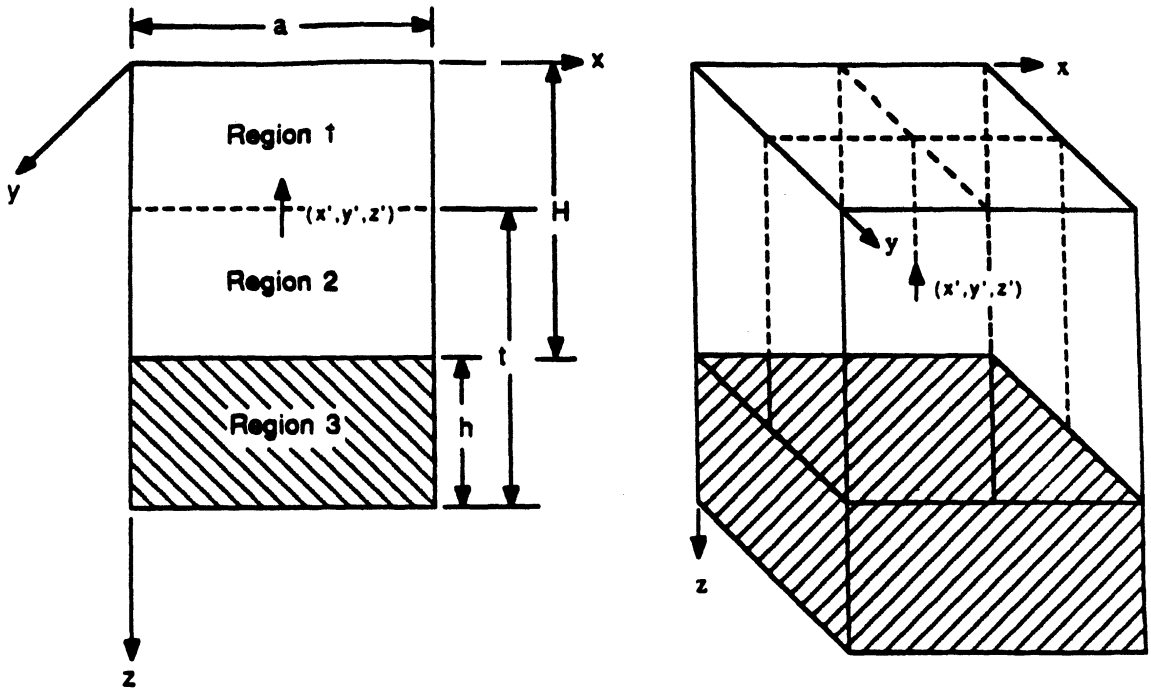

Figure 4: A z-directed current above a dielectric substrate.

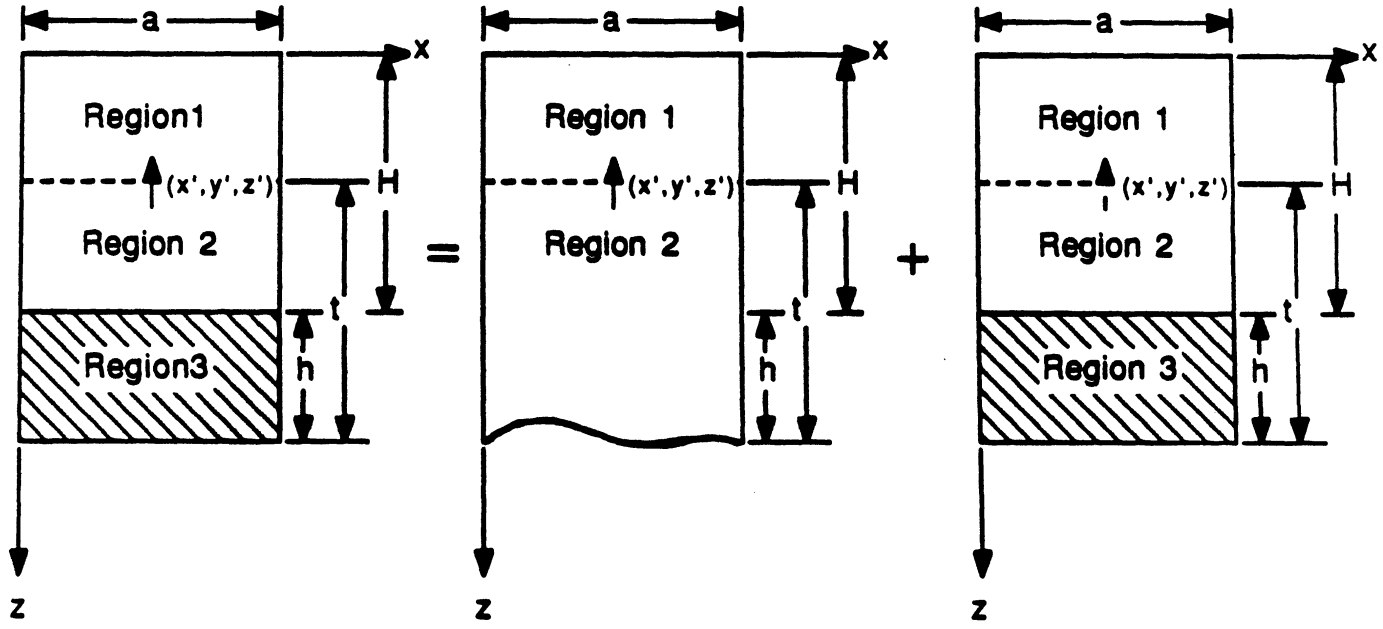

Figure 5: The problem is divided into two parts, a primary and secondary problem.

where

$$A_z^I = A_{zp}^I + A_{zs}^I \tag{50}$$

$$A_z^{II} = A_{zp}^{II} + A_{zs}^{II} \tag{51}$$

$$A_z^{III} = A_{zs}^{III}. \tag{52}$$

From our definition of Magnetic vector potentials,

$$\overline{H} = \frac{\overline{\nabla} \times \overline{A}}{\mu} \tag{53}$$

and from Maxwell's equations,

$$\overline{E} = \frac{\nabla \times \overline{H}}{j\omega\epsilon} = \frac{1}{j\omega\epsilon\mu}\nabla \times (\nabla \times \overline{A}) = \frac{1}{j\omega\epsilon\mu}(k^2\overline{A} + \overline{\nabla\nabla} \cdot \overline{A}) \tag{54}$$

therefore, for the z-directed current,

$$E_z = \frac{1}{j\omega\mu\epsilon}\left(k^2 + \frac{\delta^2}{\delta z^2}\right)A_z \tag{55}$$

$$E_y = \frac{1}{j\omega\mu\epsilon}\left(\frac{\delta^2 A_z}{\delta y \delta z}\right) \tag{56}$$

$$E_x = \frac{1}{j\omega\mu\epsilon}\left(\frac{\delta^2 A_z}{\delta x \delta z}\right) \tag{57}$$

$$H_z = 0 \tag{58}$$

$$H_y = \frac{1}{\mu}\left(\frac{-\delta A_z}{\delta x}\right) \tag{59}$$

$$H_x = \frac{1}{\mu}\left(\frac{\delta A_z}{\delta y}\right). \tag{60}$$

Now we must apply the boundary conditions of the structure to obtain the general (primary) solution. The first readily known boundary conditions are those on the walls where the tangential electric fields become zero. Therefore

$$E_x^I = 0 \; at \; z = 0 \; y = 0, b \tag{61}$$

$$E_x^{II} = 0 \; at \; y = 0, b \tag{62}$$

$$E_y^I = 0 \; at \; z = 0; \; x = 0, a \tag{63}$$

$$E_y^{II} = 0 \; at \; x = 0, a \tag{64}$$

$$E_z^I = 0 \; at \; x = 0, a \; y = 0, b \tag{65}$$

$$E_z^{II} = 0 \; at \; x = 0, a \; y = 0, b \tag{66}$$

In the primary field problem, the inhomogenous differential equation takes on the form

$$\nabla^2 A_z + k_o^2 A_z = -\mu \overline{J}. \tag{67}$$

The solution to the above equation when the listed boundary conditions are satisfied is of the form

$$A_{zp}^I = \sum_{n=1}^{\infty} \sum_{m=1}^{\infty} A^I sin\left(\frac{n\pi x}{a}\right) sin\left(\frac{m\pi y}{b}\right) cos(k_z^I z) \tag{68}$$

$$A_{zp}^{II} = \sum_{n=1}^{\infty} \sum_{m=0}^{\infty} A^{II} sin\left(\frac{n\pi x}{a}\right) sin\left(\frac{m\pi y}{b}\right) e^{-jk_z^{II}(z-z')} \tag{69}$$

In the secondary field problem, we will derive a solution that satisfies the homogenous differential equation. This is due to the fact that we do not have a current source in the secondary field problem. In both field problems, the electric fields must satisfy the same boundary conditions on the conducting walls. As a result, the secondary fields are of the same dependence with respect to the x and y coordinates, therefore

$$A^I_{zs} = \sum_{n=1}^{\infty}\sum_{m=1}^{\infty} f^I \left(j\frac{4\mu}{abk_z}\right) sin\left(\frac{n\pi x'}{a}\right) sin\left(\frac{m\pi y'}{b}\right) sin\left(\frac{n\pi x}{a}\right) sin\left(\frac{m\pi y}{b}\right) cos(k_z z) \quad (70)$$

$$A^{II}_{zs} = \sum_{n=1}^{\infty}\sum_{m=1}^{\infty}(f^{II}_s sin(k_z z) + f^{II}_c cos(k_z z))\left(j\frac{4\mu}{abk_z}e^{jk_z z'}\right) sin\left(\frac{n\pi x'}{a}\right) sin\left(\frac{m\pi y'}{b}\right) cos(k_z z') sin\left(\frac{n\pi x}{a}\right) sin\left(\frac{m\pi y}{b}\right) \quad (71)$$

For Region III we have the same standing wave solution as in Region 1 except for the fact that the conducting wall has been moved by (H+h) along the z-axis as reflected in our z dependence below

$$A^{III}_{zs} = \sum_{n=1}^{\infty}\sum_{m=1}^{\infty} j\frac{4\mu}{abk^{III}_z}e^{jk_z z'} f^{III} sin\left(\frac{n\pi x'}{a}\right) sin\left(\frac{m\pi y'}{b}\right) sin\left(\frac{n\pi x}{a}\right) sin\left(\frac{m\pi y}{b}\right) cos(k^{III}_z(z-(H+h)). \quad (72)$$

In the case of a delta function source, A_{zp} will give a G_{zzp} component in the dyadic Green's function and similarly, a A_{zs} will give a G_{zzs}. These two components are related to G_{zz} by the relation

$$G_{zz} = G_{zzp} + G_{zzs} \quad (73)$$

Since we have a current source between Regions I and II, our magnetic field is discontinuous so we must integrate the inhomogenous helmholtz equation over the

interface which results in

$$\lim_{\alpha\to 0}\int_{z'-\alpha}^{z'+\alpha}(\nabla^2+k_o^2)A_z dz = -\mu\lim_{\alpha\to 0}\int_{z'-\alpha}^{z'+\alpha}\delta(x-x')\delta(y-y')\delta(z-z')dz, \quad (74)$$

and upon simplification, one obtains

$$\lim_{\alpha\to 0}\left(\frac{\delta}{\delta z}A_z\,|_{z'-\alpha}^{z'+\alpha}\right) = -\mu\delta(x-x')\delta(y-y') \quad (75)$$

$$\frac{\delta A_z^{II}}{\delta z}\,|_{z'} - \frac{\delta A_z^{I}}{\delta z}\,|_{z'} = \mu\delta(x-x')\delta(y-y') \quad (76)$$

from (25), one obtains

$$\frac{ab}{4}\left(k_z^I sin(k_z^I z')A_z^I - jk_z^{II}A_z^{II}\right) = sin\left(\frac{n\pi x'}{a}\right)sin\left(\frac{m\pi y'}{b}\right). \quad (77)$$

One more equation is needed to solve for the two unknowns A_p^I, and A_p^{II}. Utilizing the fact that the E field in the z- direction must be continuous at the boundary between regions I and II; one obtains

$$A^I cos(k_z z') = A^{II}. \quad (78)$$

These equations are solved for the unknown coefficients resulting in

$$A_p^I = j\frac{4\mu}{abk_z}e^{jk_z z'}sin\left(\frac{n\pi x'}{a}\right)sin\left(\frac{m\pi y'}{b}\right) \quad (79)$$

$$A_p^{II} = j\frac{4\mu}{abk_z}e^{jk_z z'}sin\left(\frac{n\pi x'}{a}\right)sin\left(\frac{m\pi y'}{b}\right)cos(k_z z'). \quad (80)$$

By substituting these expressions into our general forms (68) and (69), the zz-component of the Green's function takes the form;

$$G_{zzp}^I = \sum_{n=1}^{\infty}\sum_{m=1}^{\infty} j\frac{4\mu}{abk_z}e^{jk_z z'}sin\left(\frac{n\pi x'}{a}\right)sin\left(\frac{m\pi y'}{b}\right) sin\left(\frac{n\pi x}{a}\right)sin\left(\frac{m\pi y}{b}\right)cos(k_z z) \quad (81)$$

$$G_{zzp}^{II} = \sum_{n=1}^{\infty}\sum_{m=1}^{\infty} j\frac{4\mu}{abk_z} e^{jk_z z'} sin\left(\frac{n\pi x'}{a}\right) sin\left(\frac{m\pi y'}{b}\right) cos(k_z z') \\ sin\left(\frac{n\pi x}{a}\right) sin\left(\frac{m\pi y}{b}\right) e^{-jk_z^{II}(z-z')} \quad (82)$$

In order to determine the four unknowns of the secondary field problem, boundary conditions on the air-dielectric must be applied to the structure of Fig.5c.

First, the z-component of the electric field is continuous across the boundary between regions I and II; $E_z^I = E_z^{II}$. Therefore

$$f^I cos(k_z z') - f_s^{II} sin(k_z z') - f_c^{II} cos(k_z z') = 0 \quad (83)$$

Integrating the homogenous helmholtz equation (there is no electric source in the secondary problem) across the boundary and using orthogonality, one obtains

$$f_s^{II} cos(k_z z') - f_c^{II} sin(k_z z') + f^I sin(k_z z') = 0. \quad (84)$$

From (83) and (84), we conclude that

$$f_s^{II} = 0 \quad (85)$$

and

$$f_I = f_c^{II}. \quad (86)$$

From the boundary conditions at the dielectric interface, $E_x^{II} = E_x^{III}$ one obtains

$$je^{-jk_z H} cos(k_z z') + f_c^{II} sin(k_z H) = \frac{-f^{III} sin(k_z^{III} h)}{\epsilon_r^{III} \mu_r^{III}} \quad (87)$$

and from $H_x^{II} = H_x^{III}$,

$$\frac{e^{-jk_z H} cos(k_z z') + f_c^{II} cos(k_z H)}{k_z} = \frac{1}{u_r^{III}} f^{III} \frac{cos(k_z^{III} h)}{k_z^{III}}. \quad (88)$$

The resultant Green's function for this problem will have a zz component only, which is given by

$$G_{zz}^{I} = \sum_{n=1}^{\infty}\sum_{m=1}^{\infty}(e^{jk_z z'} + f^{I})j\frac{4\mu}{abk_z}sin\left(\frac{n\pi x'}{a}\right)sin\left(\frac{m\pi y'}{b}\right) sin\left(\frac{n\pi x}{a}\right)sin\left(\frac{m\pi y}{b}\right)cos(k_z z) \quad (89)$$

$$G_{zz}^{II} = \sum_{n=1}^{\infty}\sum_{m=1}^{\infty} j\frac{4\mu}{abk_z}e^{jk_z z'}(e^{-jk_z z}cos(k_z z) + f_s^{II}sin(k_z z) + f_c^{II}cos(k_z z)) sin\left(\frac{n\pi x'}{a}\right)sin\left(\frac{m\pi y'}{b}\right) sin\left(\frac{n\pi x}{a}\right)sin\left(\frac{m\pi y}{b}\right) \quad (90)$$

$$G_{zz}^{III} = \sum_{n=1}^{\infty}\sum_{m=1}^{\infty} j\frac{4\mu}{abk_z^{III}}f^{III}sin\left(\frac{n\pi x'}{a}\right)sin\left(\frac{m\pi y'}{b}\right) sin\left(\frac{n\pi x}{a}\right)sin\left(\frac{m\pi y}{b}\right)cos(k_z^{III}(z-(H+h))). \quad (91)$$

After applying all the necessary boundary conditions, the Green's function takes on the following form

$$G_{zz}^{I} = \sum_{n=1}^{\infty}\sum_{m=1}^{\infty}\frac{\epsilon_r^{III}k_z cos(k_z(z'-H))cos(k_z^{III}h) + k_z^{III}sin(k_z(z'-H))sin(k_z^{III}h)}{k_z^2\epsilon_r^{III}sin(k_z H)cos(k_z^{III}h) + k_z^{III}k_z sin(k_z^{III}h)cos(k_z H)} \frac{4\mu}{ab}sin\left(\frac{n\pi x'}{a}\right)sin\left(\frac{m\pi y'}{b}\right) sin\left(\frac{n\pi x}{a}\right)sin\left(\frac{m\pi y}{b}\right)cos(k_z z) \quad (92)$$

$$G_{zz}^{II} = \sum_{n=1}^{\infty}\sum_{m=1}^{\infty} \frac{\epsilon_r^{III} k_z cos(k_z(z-H))cos(k_z^{III}h) + k_z^{III} sin(k_z(z-H))sin(k_z^{III}h)}{k_z^2 \epsilon_r^{III} sin(k_z H)cos(k_z^{III}h) + k_z^{III} k_z sin(k_z^{III}h)cos(k_z H)}$$
$$\frac{4\mu}{ab} sin\left(\frac{n\pi x'}{a}\right) sin\left(\frac{m\pi y'}{b}\right) cos(k_z z')$$
$$sin\left(\frac{n\pi x}{a}\right) sin\left(\frac{m\pi y}{b}\right) \tag{93}$$

$$G_{zz}^{III} = \sum_{n=1}^{\infty}\sum_{m=1}^{\infty} \frac{\epsilon_r^{III} k_z \mu_r^{III} cos(k_z z')}{k_z^2 \epsilon_r^{III} sin(k_z H)cos(k_z^{III}h) + k_z^{III} sin(k_z^{III}h)cos(k_z H)}$$
$$\frac{4\mu}{ab} sin\left(\frac{n\pi x'}{a}\right) sin\left(\frac{m\pi y'}{b}\right) cos(k_z z')$$
$$sin\left(\frac{n\pi x}{a}\right) sin\left(\frac{m\pi y}{b}\right) cos(k_z^{III}(z-(h+H))) \tag{94}$$

2.2.3 Summary of Green's function determination

In this chapter we have determined the unique Green's function for the air-bridge structure (Fig. 1). This was accomplished by working with Maxwell's equations to establish a tractable equation and by representation of our source as dirac delta functions. We then applied boundary conditions to solve for the unknown coefficients and formulated a solution. We now have expressions that will give the resulting field produced by a point source directed in the x or z direction as required to analyze the air-bridge structure.

2.3 Application of Method of Moments

The method of moments is a numerical technique used for solving functional equations which cannot be solved in closed form. By reducing the functional relation to a matrix equation, known techniques can be used to solve the resulting

matrix equation. This method is computationally intensive but with the advent of faster computers, the method has become feasible.

To apply the method of moments in the specific case of an air-bridge, one should follow the steps outlined below:

1. Use the integral equation (11) derived in section 1 along with the relations (13) and (5) so one obtains an integral equation that relates the current to the electric and magnetic fields respectively. A general form of this is

$$L_{op}(\overline{J}_s) = \overline{g} \begin{pmatrix} \overline{E} \\ \overline{H} \end{pmatrix} \tag{95}$$

where L_{op} is an integral operator operating along with the derived Green's function and $\overline{g}$ is a vector function of either the electric field $\overline{E}$ or magnetic field $\overline{H}$.

2. Represent the current on the conducting strip as a sum of coefficients multiplied by a pre-determined basis function,

$$\overline{J}_s = \sum_{q=1}^{Nia} I_q \overline{J}_q \tag{96}$$

In equation (96) where I_q represents the complex coefficients, Nia represents the number of sections the strip is to be divided into and $\overline{J}_q$ represents the chosen basis functions which represent the current distribution.

3. Discretize the integral equation by minimizing the resuting error function δE on the surface of the conducting strips.

In applying the above steps to the problem of an air-bridge we have set up the integral equation for the electric field of the form

$$\overline{E}^i = -jw\mu \int\int\int_V \left(\overline{\overline{I}} + \frac{1}{k^2}\nabla\nabla\right) \cdot \overline{\overline{G}}^i \cdot \overline{J} dV. \tag{97}$$

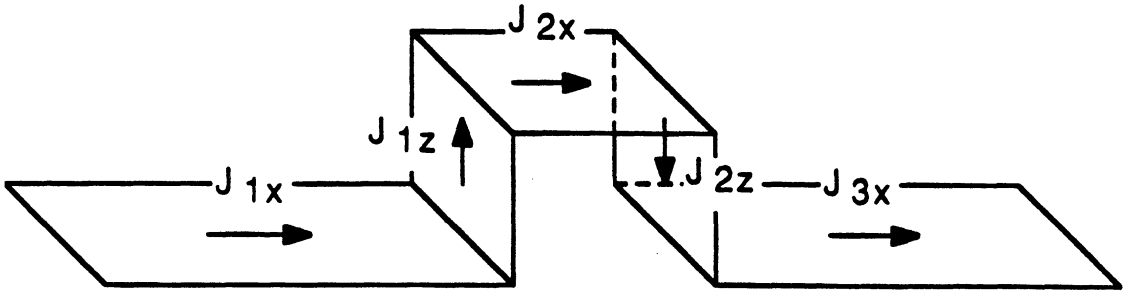

a. One dimensional view highlighting current directions

Figure 6: Currents are assigned variables by direction.

In proceeding to the second step, we seperate the problem into five different sections as pictured below (this figure is taken in part from fig.1).

For J_{1x} and J_{3x} we will model the current as a sum of an incident current A, a reflected current B, and the sum of incremental currents I_q. For J_{2x}, J_{1z}, and J_{2z} only a sum of incremental currents is required. Implementing this convention results in

$$J_{1x} = A_{1x}e^{jkx} + B_{1x}e^{-jkx} + \sum_{q=1}^{N1x} I_{q1x}\overline{J}_{1xq} \tag{98}$$

$$J_{2x} = \sum_{q=1}^{N2x} I_{q2x}\overline{J}_{2xq} \tag{99}$$

$$J_{3x} = A_{3x}e^{jkx} + B_{3x}e^{-jkx} + \sum_{q=1}^{N3x} I_{q3x}\overline{J}_{3xq} \tag{100}$$

$$J_{1z} = \sum_{q=1}^{N1z} I_{q1z}\overline{J}_{1zq} \tag{101}$$

$$J_{2z} = \sum_{q=1}^{N2z} I_{q2z}\overline{J}_{2zq}. \tag{102}$$

The basis functions the x-directed currents in this case are the same and are defined as being

$$J_{ixq}(x',y') = \begin{cases} \frac{\sin(k(x'-x_{q-1}))}{\sin(kl_z)} & x_{q-1} \le x' \le x_q \\ \frac{\sin(k(x_{q+1}-x'))}{\sin(kl_z)} & x_q \le x' \le x_{q+1} \\ \left(\frac{2}{\pi w}\right)\frac{1}{\left(1-\left(\frac{2y'}{w}\right)^2\right)^{\frac{1}{2}}} & -\frac{w}{2} \le y' \le \frac{w}{2} \end{cases} \tag{103}$$

where for the y-direction we have used a maxwellian distribution function.

The first step in discretizing the integral equation (97) is to evaluate the error that our mathematical representation of the electric field will produce. This is done by evaluating the electric field produced by one section of current on the conductor on another section of the conductor. Since the electric field on any part of the strip must be zero, the value of our integral evaluates the error. Then, by the concept of least square estimation, when one takes the inner product of the basis function along with the error and sets the result to zero, the error is minimized.

Proceeding to do this for our problem here we first account for the different components of the fields produced by a current of given orientation.

$$E_z = E_{1zz} + E_{2zz} + E_{3zz} + E_{1zs} + E_{2zs} \tag{104}$$

and

$$E_z = E_{1zz} + E_{2zz} + E_{3zz} + E_{1zz} + E_{2zz}. \tag{105}$$

First, we shall consider the x-directed field produced by a x-directed current on the dielectric

$$E_{1zz} = A_{1zz} \int_{-\frac{a}{2}}^{\frac{a}{2}} cos\left(\frac{n\pi}{a}x'\right) e^{-jkz'} dx' \int_{-\frac{w}{2}}^{\frac{w}{2}} \left(\frac{2}{\pi w}\right) \frac{1}{\left[1-\left(\frac{2y'}{w}\right)^2\right]^{\frac{1}{2}}} sin\left(\frac{m\pi}{b}y'\right) dy'$$

$$\left[\frac{\rho\, tan(k_z^{III}(H-c))}{ab(cos(k_zH))[k_z^{III}tan(k_zH) - k_z tan(k_z^{III}(H-c))]}\right.$$

$$\left(k^2 - \left(\frac{n\pi}{a}\right)^2\right) cos\left(\frac{n\pi x}{a}\right) sin\left(\frac{m\pi x}{b}\right) sin(k_z z) +$$

$$\frac{\rho\, tan(k_zH)\left(\frac{n\pi}{a}\right)(\epsilon_r^{III}-1)tan(k_z^{III}(H-c))}{abcos(k_zH)[k_z^{III}tan(k_zH) - k_z tan(k_z^{III}(H-c))]}$$

$$\left.\frac{1}{[k_z^{III}tan(k_z^{III}(H-c)) - \epsilon_r^{III}k_z tan(k_zH)]} cos\left(\frac{n\pi x}{a}\right) sin\left(\frac{m\pi x}{b}\right) cos(k_z z)\right] +$$

$$R_{1zz} \int_{-\frac{a}{2}}^{\frac{a}{2}} cos\left(\frac{n\pi}{a}x'\right) e^{jkz'} dx' \int_{-\frac{w}{2}}^{\frac{w}{2}} \left(\frac{2}{\pi w}\right) \frac{1}{\left[1-\left(\frac{2y'}{w}\right)^2\right]^{\frac{1}{2}}} sin\left(\frac{m\pi}{b}y'\right) dy'$$

$$\left[\frac{\rho\, tan(k_z^{III}(H-c))}{ab(cos(k_zH))[k_z^{III}tan(k_zH) - k_z tan(k_z^{III}(H-c))]}\right.$$

$$\left(k^2 - \left(\frac{n\pi}{a}\right)^2\right) cos\left(\frac{n\pi x}{a}\right) sin\left(\frac{m\pi x}{b}\right) sin(k_z z) +$$

$$\frac{\rho\, tan(k_z H)\left(\frac{n\pi}{a}\right)(\epsilon_r^{III}-1)tan(k_z^{III}(H-c))}{abcos(k_z H)[k_z^{III}tan(k_z H)-k_z tan(k_z^{III}(H-c))]}$$

$$\frac{1}{[k_z^{III}tan(k_z^{III}(H-c))-\epsilon_r^{III}k_z tan(k_z H)]}cos\left(\frac{n\pi x}{a}\right)sin\left(\frac{m\pi x}{b}\right)cos(k_z z)\Bigg] +$$

$$\sum_{q=1}^{N_{1x}} I_{q1x}\left(\int_{-\frac{x}{2}}^{0}\frac{sin(k(x'-x_{q-1}))}{sin(kl_x)}cos\left(\frac{n\pi}{a}x'\right)dx' +\right.$$

$$\left.\int_{0}^{\frac{x}{2}}\frac{sin(k(x_{q+1}-x'))}{sin(kl_x)}cos\left(\frac{n\pi}{a}x'\right)dx'\right)$$

$$\int_{-\frac{w}{2}}^{\frac{w}{2}}\left(\frac{2}{\pi w}\right)\frac{1}{\left[1-\left(\frac{2y'}{w}\right)^2\right]^{\frac{1}{2}}}sin\left(\frac{m\pi}{b}y'\right)dy'$$

$$\Bigg[\left(k^2-\left(\frac{n\pi}{a}\right)^2\right)\frac{\rho\, tan(k_z^{III}(H-c))}{ab(cos(k_z H))[k_z^{III}tan(k_z H)-k_z tan(k_z^{III}(H-c))]}$$

$$cos\left(\frac{n\pi x}{a}\right)sin\left(\frac{m\pi x}{b}\right)sin(k_z z) +$$

$$\frac{\rho\, tan(k_z H)\left(\frac{n\pi}{a}\right)(\epsilon_r^{III}-1)tan(k_z^{III}(H-c))}{abcos(k_z H)[k_z^{III}tan(k_z H)-k_z tan(k_z^{III}(H-c))]}$$

$$\frac{1}{[k_z^{III}tan(k_z^{III}(H-c))-\epsilon_r^{III}k_z tan(k_z H)]}$$

$$\left(\frac{n\pi}{a}\right)k_z cos\left(\frac{n\pi x}{a}\right)sin\left(\frac{m\pi y}{b}\right)cos(k_z z)\Bigg] \qquad (106)$$

~~Integrating this expression over the surface of the conducting microstrip where~~

~~the x-component of the electric field can exist, one obtains~~

For a x-directed current, a z-directed field is also produced. Proceeding with the same procedure as above one obtains

$$E_{1zx} = A_{1zx}\int_{-\frac{a}{2}}^{\frac{a}{2}} cos\left(\frac{n\pi}{a}x'\right)e^{-jkx'}dx'\int_{-\frac{w}{2}}^{\frac{w}{2}}\left(\frac{2}{\pi w}\right)\frac{1}{\left[1-\left(\frac{2y'}{w}\right)^2\right]^{\frac{1}{2}}}sin\left(\frac{m\pi}{b}y'\right)dy'$$

$$\left[\frac{\rho\, tan(k_z^{III}(H-c))}{ab(cos(k_zH))[k_z^{III}tan(k_zH)-k_ztan(k_z^{III}(H-c))]}\right.$$

$$\left(\frac{-n\pi}{a}\right)sin\left(\frac{n\pi x}{a}\right)sin\left(\frac{m\pi y}{b}\right)k_zcos(k_zz)+$$

$$\frac{\rho\, tan(k_zH)\left(\frac{n\pi}{a}\right)(\epsilon_r^{III}-1)tan(k_z^{III}(H-c))}{abcos(k_zH)[k_z^{III}tan(k_zH)-k_ztan(k_z^{III}(H-c))]}$$

$$\frac{1}{[k_z^{III}tan(k_z^{III}(H-c))-\epsilon_r^{III}k_ztan(k_zH)]}$$

$$\left.(k^2-k_z^2)sin\left(\frac{n\pi x}{a}\right)sin\left(\frac{m\pi y}{b}\right)sin(k_zz)\right]+$$

$$R_{1zx}\int_{-\frac{a}{2}}^{\frac{a}{2}} cos\left(\frac{n\pi}{a}x'\right)e^{jkx'}dx'\int_{-\frac{w}{2}}^{\frac{w}{2}}\left(\frac{2}{\pi w}\right)\frac{1}{\left[1-\left(\frac{2y'}{w}\right)^2\right]^{\frac{1}{2}}}sin\left(\frac{m\pi}{b}y'\right)dy'$$

$$\left[\frac{\rho\, tan(k_z^{III}(H-c))}{ab(cos(k_zH))[k_z^{III}tan(k_zH)-k_ztan(k_z^{III}(H-c))]}\right.$$

$$\left(\frac{-n\pi}{a}\right)sin\left(\frac{n\pi x}{a}\right)sin\left(\frac{m\pi y}{b}\right)k_zcos(k_zz)+$$

$$\frac{\rho\, tan(k_z H)\left(\frac{n\pi}{a}\right)(\epsilon_r^{III}-1)tan(k_z^{III}(H-c))}{abcos(k_z H)[k_z^{III}tan(k_z H)-k_z tan(k_z^{III}(H-c))]}$$

$$\frac{1}{[k_z^{III}tan(k_z^{III}(H-c))-\epsilon_r^{III}k_z tan(k_z H)]}$$

$$(k^2-k_z^2)sin\left(\frac{n\pi x}{a}\right)sin\left(\frac{m\pi y}{b}\right)sin(k_z z)\Big] +$$

$$\sum_{q=1}^{N_{1x}} I_{q1x}\left(\int_{-\frac{a}{2}}^{0}\frac{sin(k(x'-x_{q-1}))}{sin(kl_x)}cos\left(\frac{n\pi}{a}x'\right)dx' +\right.$$

$$\left.\int_{0}^{\frac{a}{2}}\frac{sin(k(x_{q+1}-x'))}{sin(kl_x)}cos\left(\frac{n\pi}{a}x'\right)dx'\right)$$

$$\int_{-\frac{w}{2}}^{\frac{w}{2}}\left(\frac{2}{\pi w}\right)\frac{1}{\left[1-\left(\frac{2y'}{w}\right)^2\right]^{\frac{1}{2}}}sin\left(\frac{m\pi}{b}y'\right)dy'$$

$$\left[\frac{\rho\, tan(k_z^{III}(H-c))}{ab(cos(k_z H))[k_z^{III}tan(k_z H)-k_z tan(k_z^{III}(H-c))]}\right.$$

$$\left(\frac{-n\pi}{a}\right)sin\left(\frac{n\pi x}{a}\right)sin\left(\frac{m\pi y}{b}\right)k_z cos(k_z z) +$$

$$\frac{\rho\, tan(k_z H)\left(\frac{n\pi}{a}\right)(\epsilon_r^{III}-1)tan(k_z^{III}(H-c))}{abcos(k_z H)[k_z^{III}tan(k_z H)-k_z tan(k_z^{III}(H-c))]}$$

$$\frac{1}{[k_z^{III}tan(k_z^{III}(H-c))-\epsilon_r^{III}k_z tan(k_z H)]}$$

$$(k^2 - k_z^2) sin\left(\frac{n\pi x}{a}\right) sin\left(\frac{m\pi y}{b}\right) sin(k_z z)\Big] \tag{107}$$

For a z-directed current, one must consider the fields above and below the source seprately as they have different forms in those two respective regions. Also, as before, both x- and z-components of the electric field are produced.

First we consider the x-directed field produced by a z-directed current above the source where

$$E_{1axz} = \sum_{q=1}^{N_{1z}} I_{q1z} \left(\int_{-\frac{s}{2}}^{0} \frac{sin(k(z' - z_{q-1}))}{sin(kl_z)} (\epsilon_r^{III} k_z cos(k_z(z' - H)) cos(k_z^{III} h) + \right.$$

$$k_z^{III} sin(k_z(z' - H)) sin(k_z^{III} h) dz') +$$

$$\int_{0}^{-\frac{s}{2}} \frac{sin(k(z_{q+1} - z'))}{sin(kl_z)} (\epsilon_r^{III} k_z cos(k_z(z' - H)) cos(k_z^{III} h) +$$

$$\left. k_z^{III} sin(k_z(z' - H)) sin(k_z^{III} h) dz') \right)$$

$$\int_{-\frac{w}{2}}^{\frac{w}{2}} \left(\frac{2}{\pi w}\right) \frac{1}{\left[1 - \left(\frac{2y'}{w}\right)^2\right]^{\frac{1}{2}}} sin\left(\frac{m\pi}{b} y'\right) dy'$$

$$\frac{4\mu}{ab} \frac{1}{\epsilon_r^{III} k_z^2 sin(k_z H) cos(k_z^{III} h) + k_z^{III} k_z cos(k_z H) sin(k_z^{III} h)} sin\left(\frac{n\pi}{a} x'\right)$$

$$\left(\frac{n\pi}{a}\right) cos\left(\frac{n\pi x}{a}\right) sin\left(\frac{m\pi y}{b}\right) (-k_z) sin(k_z z) \tag{108}$$

For the x-directed field below the source produced by a z-directed current, one

obtains

$$E_{1bzz} = \sum_{q=1}^{N_{1z}} I_{q1z} \left(\int_{\frac{b}{2}}^{0} \frac{sin(k(z' - z_{q-1}))}{sin(kl_z)} cos(k_z z') dz' + \int_{0}^{-\frac{b}{2}} \frac{sin(k(z_{q+1} - z'))}{sin(kl_z)} cos(k_z z') dz' \right)$$

$$\int_{-\frac{w}{2}}^{\frac{w}{2}} \left(\frac{2}{\pi w}\right) \frac{1}{\left[1 - \left(\frac{2y'}{w}\right)^2\right]^{\frac{1}{2}}} sin\left(\frac{m\pi}{b} y'\right) dy'$$

$$\frac{4\mu}{ab} \frac{\epsilon_r^{III} k_z sin(k_z(z - H)) cos(k_z^{III} h) + k_z^{III} cos(k_z(z - H)) sin(k_z^{III} h)}{k_z \epsilon_r^{III} sin(k_z H) cos(k_z^{III} h) + k_z^{III} sin(k_z^{III} h) cos(k_z H)} sin\left(\frac{n\pi}{a} x'\right)$$

$$\left(\frac{n\pi}{a}\right) cos\left(\frac{n\pi x}{a}\right) sin\left(\frac{m\pi y}{b}\right) \tag{109}$$

For the z-directed field above the source produced by a z-directed current, one obtains

$$E_{1azz} = \sum_{q=1}^{N_{1z}} I_{q1z} \left(\int_{\frac{b}{2}}^{0} \frac{sin(k(z' - z_{q-1}))}{sin(kl_z)} (\epsilon_r^{III} k_z cos(k_z(z' - H)) cos(k_z^{III} h) +$$

$$k_z^{III} sin(k_z(z' - H)) sin(k_z^{III} h) dz') +$$

$$\int_{0}^{-\frac{b}{2}} \frac{sin(k(z_{q+1} - z'))}{sin(kl_z)} (\epsilon_r^{III} k_z cos(k_z(z' - H)) cos(k_z^{III} h) +$$

$$k_z^{III} sin(k_z(z' - H)) sin(k_z^{III} h) dz') \Big)$$

$$\int_{-\frac{w}{2}}^{\frac{w}{2}} \left(\frac{2}{\pi w}\right) \frac{1}{\left[1 - \left(\frac{2y'}{w}\right)^2\right]^{\frac{1}{2}}} sin\left(\frac{m\pi}{b} y'\right) dy'$$

$$\frac{4\mu}{ab}\frac{1}{\epsilon_r^{III}k_z^2 sin(k_z H)cos(k_z^{III}h)+k_z^{III}k_z cos(k_z H)sin(k_z^{III}h)}sin\left(\frac{n\pi}{a}x'\right)$$

$$(k^2-k_z^2)sin\left(\frac{n\pi x}{a}\right)sin\left(\frac{m\pi y}{b}\right)cos(k_z z) \tag{110}$$

For the z-directed field below the source produced by a z-directed current, one obtains

$$E_{1bzz} = \sum_{q=1}^{N_{1z}} I_{q1z}\left(\int_{\frac{s}{2}}^{0}\frac{sin(k(z'-z_{q-1}))}{sin(kl_z)}cos(k_z z')dz'+\int_{0}^{-\frac{s}{2}}\frac{sin(k(z_{q+1}-z'))}{sin(kl_z)}cos(k_z z')dz'\right)$$

$$\int_{-\frac{w}{2}}^{\frac{w}{2}}\left(\frac{2}{\pi w}\right)\frac{1}{\left[1-\left(\frac{2y'}{w}\right)^2\right]^{\frac{1}{2}}}sin\left(\frac{m\pi}{b}y'\right)dy'$$

$$\frac{4\mu}{ab}sin\left(\frac{n\pi}{a}x'\right)$$

$$\frac{\epsilon_r^{III}k_z sin(k_z(z-H))cos(k_z^{III}h)+k_z^{III}cos(k_z(z-H))sin(k_z^{III}h)}{k_z\epsilon_r^{III}sin(k_z H)cos(k_z^{III}h)+k_z^{III}sin(k_z^{III}h)cos(k_z H)}$$

$$(k^2-k_z^2)sin\left(\frac{n\pi x}{a}\right)sin\left(\frac{m\pi y}{b}\right) \tag{111}$$

For a x-directed field in the region above a x-directed current which is above the dielectric, one obtains

$$E_{1axxa} = \sum_{q=1}^{N_{2x}} I_{q2x}\left(\int_{-\frac{s}{2}}^{0}\frac{sin(k(x'-x_{q-1}))}{sin(kl_x)}cos\left(\frac{n\pi}{a}x'\right)dx'+\right.$$

$$\left.\int_{0}^{\frac{s}{2}}\frac{sin(k(x_{q+1}-x'))}{sin(kl_x)}cos\left(\frac{n\pi}{a}x'\right)dx'\right)$$

$$\int_{-\frac{w}{2}}^{\frac{w}{2}} \left(\frac{2}{\pi w}\right) \frac{1}{\left[1-\left(\frac{2y'}{w}\right)^2\right]^{\frac{1}{2}}} sin\left(\frac{m\pi}{b}y'\right) dy'$$

$$\left[\left(k^2-\left(\frac{n\pi}{a}\right)^2\right) \frac{\rho\left[\frac{k_z^{III}-k_z tan(k_z^{III}(H-c))tan(k_z H)}{k_z^{III}tan(k_z H)-k_z tan(k_z^{III}(H-c))} - cot(k_z H)\right]}{abk_z[cot(k_z z')cos(k_z z') - sin(k_z z')]}\right.$$

$$cos\left(\frac{n\pi x}{a}\right) sin\left(\frac{m\pi x}{b}\right) sin(k_z z) +$$

$$\frac{\rho(1-tan^2(k_z H))\left(\frac{n\pi}{a}\right)(\epsilon_r^{III}-1)tan(k_z^{III}(H-c))}{ab[k_z^{III}tan(k_z H) - k_z tan(k_z^{III}(H-c))][cot(k_z z')cos(k_z z') - sin(k_z z')]}$$

$$\frac{1}{k_z^{III}tan(k_z^{III}(H-c)) - \epsilon_r^{III}k_z tan(k_z H)}$$

$$\left.\left(\frac{n\pi}{a}\right) k_z cos\left(\frac{n\pi x}{a}\right) sin\left(\frac{m\pi y}{b}\right)(-k_z sin(k_z z))\right] \qquad (112)$$

For the x-directed field located below the x-directed current source which is above the dielectric, we obtain

$$E_{1bxxs} = \sum_{q=1}^{N_{2x}} I_{q2x}\left(\int_{-\frac{a}{2}}^{0} \frac{sin(k(x'-x_{q-1}))}{sin(kl_x)} cos\left(\frac{n\pi}{a}x'\right) dx' +\right.$$

$$\left.\int_{0}^{\frac{a}{2}} \frac{sin(k(x_{q+1}-x'))}{sin(kl_x)} cos\left(\frac{n\pi}{a}x'\right) dx'\right)$$

$$\int_{-\frac{w}{2}}^{\frac{w}{2}} \left(\frac{2}{\pi w}\right) \frac{1}{\left[1-\left(\frac{2y'}{w}\right)^2\right]^{\frac{1}{2}}} sin\left(\frac{m\pi}{b}y'\right) dy'$$

$$\left[\left(k^2-\left(\frac{n\pi}{a}\right)^2\right) \frac{\rho\left[k_z^{III} - k_z tan(k_z^{III}(H-c))tan(k_z H)\right]}{abk_z[cot(k_z z')cos(k_z z') - sin(k_z z')][k_z^{III}tan(k_z H) - k_z tan(k_z^{III}(H\right.$$

$$cos\left(\frac{n\pi x}{a}\right) sin\left(\frac{m\pi y}{b}\right) sin(k_z^{II} z) +$$

$$\frac{-\rho}{abk_z[cot(k_z z')cos(k_z z') - sin(k_z z')]} cos\left(\frac{n\pi x}{a}\right) sin\left(\frac{m\pi y}{b}\right) cos(k_z^{II} z) +$$

$$\frac{\rho(1 - tan^2(k_z H))\left(\frac{n\pi}{a}\right)(\epsilon_r^{III} - 1)tan(k_z^{III}(H - c))}{ab[k_z^{III} tan(k_z H) - k_z tan(k_z^{III}(H - c))][cot(k_z z')cos(k_z z') - sin(k_z z')]}$$

$$\frac{1}{k_z^{III} tan(k_z^{III}(H - c)) - \epsilon_r^{III} k_z tan(k_z H)}$$

$$\left(\frac{n\pi}{a}\right) k_z cos\left(\frac{n\pi x}{a}\right) sin\left(\frac{m\pi y}{b}\right)(-k_z) sin(k_z z)\Big]$$

For a z-directed field above the current produced from a x-directed current above the dielectric, one obtains the expression

$$E_{1azza} = \sum_{q=1}^{N_{2z}} I_{q2x} \left(\int_{-\frac{a}{2}}^{0} \frac{sin(k(x' - x_{q-1}))}{sin(kl_x)} cos\left(\frac{n\pi}{a} x'\right) dx' + \right.$$

$$\left. \int_{0}^{\frac{a}{2}} \frac{sin(k(x_{q+1} - x'))}{sin(kl_x)} cos\left(\frac{n\pi}{a} x'\right) dx' \right)$$

$$\int_{-\frac{w}{2}}^{\frac{w}{2}} \left(\frac{2}{\pi w}\right) \frac{1}{\left[1 - \left(\frac{2y'}{w}\right)^2\right]^{\frac{1}{2}}} sin\left(\frac{m\pi}{b} y'\right) dy'$$

$$\left(-\frac{n\pi}{a}\right) sin\left(\frac{n\pi}{a} x\right) \frac{\rho \left[\frac{k_z^{III} - k_z tan(k_z^{III}(H-c)) tan(k_z H)}{k_z^{III} tan(k_z H) - k_z tan(k_z^{III}(H-c))} - cot(k_z H)\right]}{abk_z[cot(k_z z')cos(k_z z') - sin(k_z z')]}$$

$$sin\left(\frac{m\pi y}{b}\right)(k_z)cos(k_z z) +$$

$$\frac{\rho(1-tan^2(k_z H))\left(\frac{n\pi}{a}\right)(\epsilon_r^{III}-1)tan(k_z^{III}(H-c))}{ab[k_z^{III}tan(k_z H)-k_z tan(k_z^{III}(H-c))][cot(k_z z')cos(k_z z')-sin(k_z z')]}$$

$$\frac{1}{k_z^{III}tan(k_z^{III}(H-c))-\epsilon_r^{III}k_z tan(k_z H)}$$

$$(k^2-k_z^2)sin\left(\frac{n\pi x}{a}\right)sin\left(\frac{m\pi y}{b}\right)cos(k_z z)\Big] \qquad (114)$$

For a z-directed field below the current produced from a x-directed current above the dielectric, one obtains the expression

$$E_{1bzxs} = \sum_{q=1}^{N_{2x}} I_{q2x}\left(\int_{-\frac{x}{2}}^{0}\frac{sin(k(x'-x_{q-1}))}{sin(kl_x)}cos\left(\frac{n\pi}{a}x'\right)dx' +$$

$$\int_{0}^{\frac{x}{2}}\frac{sin(k(x_{q+1}-x'))}{sin(kl_x)}cos\left(\frac{n\pi}{a}x'\right)dx'\right)$$

$$\int_{-\frac{w}{2}}^{\frac{w}{2}}\left(\frac{2}{\pi w}\right)\frac{1}{\left[1-\left(\frac{2y'}{w}\right)^2\right]^{\frac{1}{2}}}sin\left(\frac{m\pi}{b}y'\right)dy'$$

$$\left[\frac{\rho\left[k_z^{III}-k_z tan(k_z^{III}(H-c))tan(k_z H)\right]}{abk_z[cot(k_z z')cos(k_z z')-sin(k_z z')][k_z^{III}tan(k_z H)-k_z tan(k_z^{III}(H-c))]}\right.$$

$$\left(-\frac{n\pi}{a}\right)sin\left(\frac{n\pi x}{a}\right)sin\left(\frac{m\pi y}{b}\right)k_z cos(k_z^{II}z) +$$

$$\frac{-\rho}{abk_z[cot(k_z z')cos(k_z z')-sin(k_z z')]}\left(-\frac{n\pi}{a}\right)sin\left(\frac{n\pi x}{a}\right)sin\left(\frac{m\pi y}{b}\right)(-k_z)sin(k_z^{II}z)$$

$$\frac{\rho(1-tan^2(k_zH))\left(\frac{n\pi}{a}\right)(\epsilon_r^{III}-1)tan(k_z^{III}(H-c))}{ab[k_z^{III}tan(k_zH)-k_ztan(k_z^{III}(H-c))][cot(k_zz')cos(k_zz')-sin(k_zz')]}$$

$$\frac{1}{k_z^{III}tan(k_z^{III}(H-c))-\epsilon_r^{III}k_ztan(k_zH)}$$

$$(k^2-k_z^2)sin\left(\frac{n\pi x}{a}\right)sin\left(\frac{m\pi y}{b}\right)cos(k_zz)\Big]$$

2.4 Matrix Equation

The resulting matrix equation is formed and upon inversion the unknowns can be obtained for a given exciation.

3 Scattering Parameters

Using the derived current distribution on the conductors, one can apply an ideal transmission line model to determine the scattering parameters.

4 Summary

From this general analysis of the Green's function and the ultimate determination of the scattering parameters of an air-bridge, the formulation used here could be applied to a variety of structures whose geometry requires a three-dimentional analysis.

Other planned work includes the application of this work to other structures and the use of air-bridges as a curcuit element in the construction of other passive microwave circuits.

References

[1] A. Sommerfeld, *Partial Differential Equations*, New York:Academic Press Inc., 1949.

[2] R. Harrington, *Field Computation by Moment Methods*, New York:The Macmillan Company, 1968.

[3] L. P. Dunleavy and P. B. Katehi, *Preliminary results for study of theoritical and experimental characherization of discontinuities in shielded microstirip*, radiation lab report RL 846, August 1987.

[4] R. Harrington, *Time-Harmonic Electromagnetic Fields*, New York:McGraw-Hill, 1961.

[5] T. Hirota, Y. Tarusawa, H. Ogawa, "Uniplanar MMIC Hybrids-A Proposed New MMIC Structure" *IEEE Transactions on Microwave Theory and Tecniques, Vol. MTT-35, No.6, June 1987 pp. 576-581.*

[6] R. E. Collin, *Field Theory of Guided Waves*, McGraw-Hill, New York, 1960